Gaseous Tracking Detectors

4

This chapter describes various gaseous tracking detectors that are used to measure particle trajectories with high precision. First, we discuss planar multi-wire proportional chambers (Sect. 4.1) followed by planar drift chambers (Sect. 4.2). These chambers are still used in fixed-target experiments and in endcaps of colliding-beam detectors. For usage in the central region of colliding-beam experiments, cylindrical chambers are necessary. Thus, we continue our discussion with cylindrical drift chambers (Sect. 4.3), jet drift chambers (Sect. 4.4) and time projection chambers (Sect. 4.5). We then focus on some other developments such as the microstrip gas chambers (Sect. 4.6), the electron gas multiplication (Sect. 4.7), micromesh gaseous structures (Sect. 4.8), resistive plate chambers (Sect. 4.9), limited streamer tubes (Sect. 4.10), monitored drift tubes (Sect. 4.11) and thin gap chambers (Sect. 4.14). At the end we mention briefly the bubble chamber for historic reasons (Sect. 4.15), list some older technologies (Sect. 4.16) and present a comparison of position resolutions of tracking detectors (Sect. 4.17). We will not present here cloud, flash, spark and streamer chambers since they cannot be read out electronically and are no longer used. Cloud chambers, also called Wilson chambers [1], played an important role from the 1910s to 1950s. Note that the positron [2], muon [3] and kaon [4] were discovered using cloud chambers. Spark [5] and streamer [6] chambers were used from the 1930s to 1960s. While spark chambers consisted of a stack of metal plates housed in a gas volume streamer chambers just had two plates. Flash chamber were used in neutrino experiments [7,8].

G. Eigen, *Detectors in High-Energy Physics Experiments*, Graduate Texts in Physics,
https://doi.org/10.1007/978-3-031-67336-8_4

4.1 Multi-Wire Proportional Chambers

In the previous chapter we saw that the ionization in proportional counters is localized rather precisely due to the slowly moving positive ions. Thus, by combining many proportional counters we can build large-area multi-wire proportional chambers (MWPC) to measure the position of traversing particles. This idea was proposed first by Charpak [9] for which he was awarded the Nobel prize in physics in 1992.

4.1.1 Principles

Figure 4.1 shows a schematic view (left) and a cross section (right) of a multi-wire proportional chamber. Many anode wires are arranged parallel to each other in a plane at fixed spacing called pitch. The anode wire plane is sandwiched between two cathode planes. A high electric field is applied between anode and cathode. While cathode planes typically are kept at ground potential, anode wires are connected to high voltage. Each anode wire acts as a separate proportional counter. Figure 4.2 (left) shows the electric-field lines and equipotential surfaces of an MWPC. The electric-field lines of two adjacent wires repel each other leading to a field-free region at the midpoint between the two wires. Away from the wire plane the electric field is constant in most parts of the chamber. If a wire is displaced, the electric field becomes distorted as depicted in Fig. 4.2 (right). We discuss the effects of displaced wires below.

We define a coordinate system in which the x-axis is perpendicular to the anode wires in the chamber plane, the y-axis is along the direction of the anode wires and the z-axis is perpendicular to the cathode plane as shown in Fig. 4.1 (left). In this coordinate system the beam direction is along the z axis. The analytic form of the electric field and electric potential is obtained by solving the Laplace equation in two

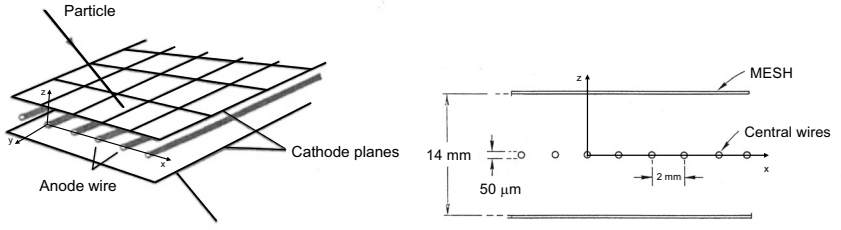

Fig. 4.1 Left: Schematic view of a multi-wire proportional chamber. Reprinted with kind permission from [10], © 1992, CERN. All rights reserved. Right: Cross section through a typical MWPC. Here, the anode wire pitch is 2 mm, the diameter of the gold-plated tungsten wire is 50 μm and the anode-cathode gap is 7 mm. Reprinted with kind permission from [11], © 1969, SLAC. All rights reserved

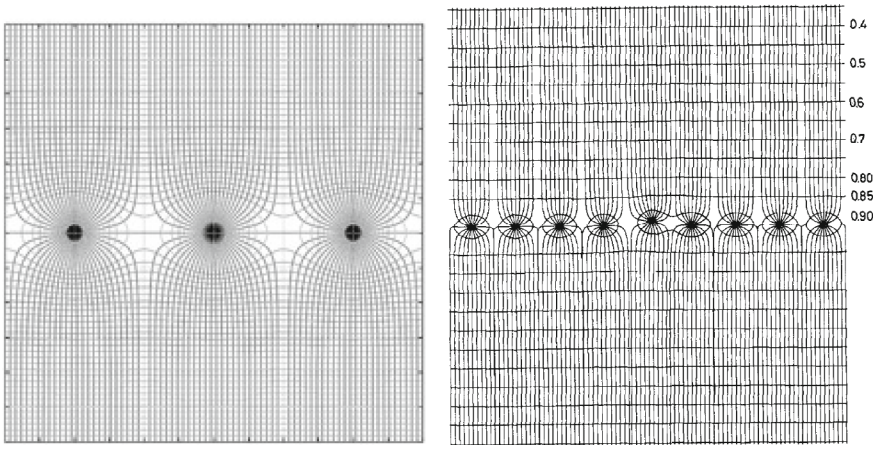

Fig. 4.2 Left: Schematic view of the electric-field lines (vertical lines) and equipotential surfaces (horizontal lines) in an MWPC in the vicinity of anode wires. Reprinted under CC-BY-NC-ND-4.0 Licence with kind permission from [12], © 2023, F. Sauli. Right: Schematic view of the electric-field lines and equipotential surfaces in an MWPC in which one wire is displaced. Reprinted with kind permission from [13], © 1970, Elsevier. All rights reserved

dimensions. The analytic solution is given in textbooks, e.g. Morse and Feshbach [14] or Buchholz [15]. A useful approximation is given by Erskine [16],

$$V(x,z) = \frac{C_w \cdot V_0}{4\pi\epsilon_0}\left\{\frac{2\pi a_w}{s_w} - \ln\left[4\left(\sin^2\left(\frac{\pi x}{s_w}\right) + \sinh^2\left(\frac{\pi z}{s_w}\right)\right)\right]\right\}, \quad (4.1)$$

$$|\vec{E}(x,z)| = \frac{C_w \cdot V_0}{2\epsilon_0 s_w}\frac{\sqrt{1+\tan^2\left(\frac{\pi x}{s_w}\right)\tanh^2\left(\frac{\pi z}{s_w}\right)}}{\sqrt{\tan^2\left(\frac{\pi x}{s_w}\right)+\tanh^2\left(\frac{\pi z}{s_w}\right)}}, \quad (4.2)$$

where s_w is the anode wire pitch, a_w is the gap between anode and cathode, d_w is the anode wire diameter, V_0 is the high voltage on the anode wire and C_w is the capacitance per unit length to ground determined by

$$C_w = \frac{2\pi\epsilon_0}{\frac{\pi a_w}{s_w} - \ln\left(\frac{\pi d_w}{s_w}\right)}. \quad (4.3)$$

Since $d_w/2 \ll s_w$ the capacitance per unit length in (4.3) is always smaller than that of a plane capacitor with the same surface ($2\epsilon_0 s_w/a_w$). Typical values for the anode-cathode gap are 4–8 mm and for the wire diameter are 20–100 μm. The anode wire pitch is around 2 mm. Figure 4.3 depicts the capacitance as a function of the wire spacing s_w. The capacitance increases with larger spacing up to $\sim$ 1 cm before leveling off. For small wire spacings the dependence on the wire diameter is rather weak. Reducing the anode-cathode gap increases the capacitance. For example, for

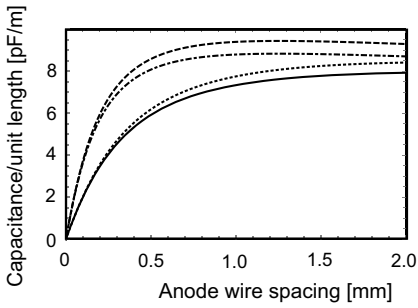

Fig. 4.3 The capacitance per unit length as a function of the wire spacing s_w for $a_w = 8$ mm and $d_w = 0.02$ mm (solid curve), $a_w = 8$ mm and $d_w = 0.03$ mm (dotted curve), $a_w = 4$ mm and $d_w = 0.02$ mm (dash-dotted curve) and $a_w = 4$ mm and $d_w = 0.03$ mm (dashed curve)

$a_w = 8$ mm, $d_w = 20\,\mu$m and $s_w = 2$ mm we get a capacitance of $C_w = 3.47$ pF/m. Reducing the gap to 4 mm increases the capacitance to 5.71 pF/m. More values are given in reference [17]. For $z = 0$ and $x = 0$ the electric field takes the forms

$$E_x = |\vec{E}(x,0)| = \frac{C_w \cdot V_0}{2\epsilon_0 s_w} \cot \frac{\pi x}{s_w} \tag{4.4}$$

$$E_z = |\vec{E}(0,z)| = \frac{C_w \cdot V_0}{2\epsilon_0 s_w} \coth \frac{\pi z}{s_w}, \tag{4.5}$$

respectively. For a single anode wire, the electric field is $E(r) \propto 1/r$, where $r = \sqrt{x^2 + z^2}$. In fact, we recover the $1/r$ dependence for $z \ll s_w$

$$|\vec{E}(x,z)| = \frac{C_w V_0}{2\pi\epsilon_0} \frac{1}{r}. \tag{4.6}$$

For large $z \geq s_w$, the electric field approaches a constant

$$|\vec{E}_0(x,z)| = \frac{C_w V_0}{2\epsilon_0 s_w}, \tag{4.7}$$

because for large z values we get $\tanh(\pi z/s_w) = 1$.

Let us consider a chamber with dimensions $s_w = 2$ mm, $d_w = 0.02$ mm and $a_w = 8$ mm that is filled with an Ar-CO_2 (75:25) gas mixture. If we apply a voltage of $V_0 = 4000$ V, the electric field at the anode wire is $|\vec{E}| = 2.5 \times 10^5$ V/cm. Figure 4.4 shows the electric-field strength for this chamber in the x- and z-directions in a double logarithmic scale. Near the anode wire, the electric field decreases as $1/r$ like in a cylindrical proportional counter shown by the straight lines at small distances. In the x-direction, the electric field continues to drop becoming rather weak in the middle region between two anode wires. At the midpoint it is zero. In the z-direction, the electric field approaches a constant value of $|\vec{E}_0(x,z)|$ given in (4.7). This already occurs at a distance of $z \geq 0.5 s_w$.

A charged particle traversing the MWPC liberates electron-ion pairs along its path as sketched in Fig. 3.3. The electrons are accelerated along the electric-field lines towards the nearest anode wires while the positive ions move very slowly towards the cathode plane. As discussed in the previous chapter, each primary electron produces

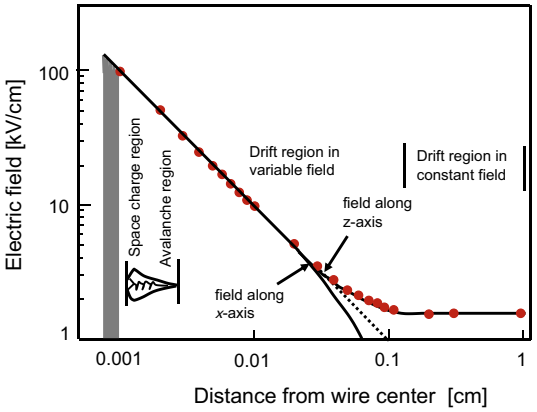

Fig. 4.4 Electric-field strengths E_x and E_z as a function of the anode wire distance perpendicular to the anode wire plane (z-direction) and that perpendicular to the anode wires in the anode wire plane (x-direction) for a chamber with $V_0 = 4000$ V, $s_w = 2$ mm, $d_w = 0.02$ mm and $a_w = 8$ mm. Solid points show measurements. The grey bar at 10 μm indicates the anode wire position. The space charge region, avalanche region, drift region in a variable electric field and the drift region in a constant field are marked. In the x-direction the electric-field strengths drops more rapidly than $1/r$ shown by the dashed line. At large z distances the electric field approaches the constant value of $|\vec{E}_0| = (C_w V_0)/(2 s_w \epsilon_0)$. Reprinted under CC-BY-3.0 Licence from [17], ©1977–2024, CERN

an avalanche near the closest anode wire if the gas amplification is sufficiently high. Since primary electrons are produced successively along the path of the traversing charged particle, the arrival time of each primary electron at each anode wire is slightly different. One primary electron after another reaches the high electric-field region and produces an individual avalanche and in turn a signal pulse. The observed signal on the anode wire consists of several individual pulses each produced by a separate avalanche. With good time resolution, these individual pulses can be resolved whose rise time is about 0.1 ns and whose decay time depends on the time constant $\tau_{\text{ch}} = R_{\text{ch}} C_{\text{ch}}$, where R_{ch} is the resistor and C_{ch} is the capacitance of the readout chain. Figure 4.5 (left) shows a picture of individual pulses taken from an oscilloscope and Fig. 4.5 (right) shows a simulation of individual pulses. If we sum over all individual pulses, a pulse with a long tail is observed as depicted in the inset of Fig. 4.5 (right). While the electron cloud formed in an avalanche develops into a tube around anode wire, the shape of the slowly moving ions still retains the memory of the origin of the avalanche by forming a drop-like shape. Each anode wire of an MWPC acts as an independent detector [9]. As Charpak noticed, positive signals induced in all electrodes by the positive ions are largely compensated by the negative signals produced by capacitive coupling.

The timing properties of proportional chambers are determined by the collection time of the electrons produced by ionizing tracks. Figure 4.6 (left) shows a typical signal recorded with an MWPC, which results from electrons collected in three regions (A, B, C) as shown in Fig. 4.6 (center) [19]. Electrons produced in region A are quickly collected because typical drift velocities in this high-field region are above 5 cm/μs. Electrons produced in the low field region B will produce a tail

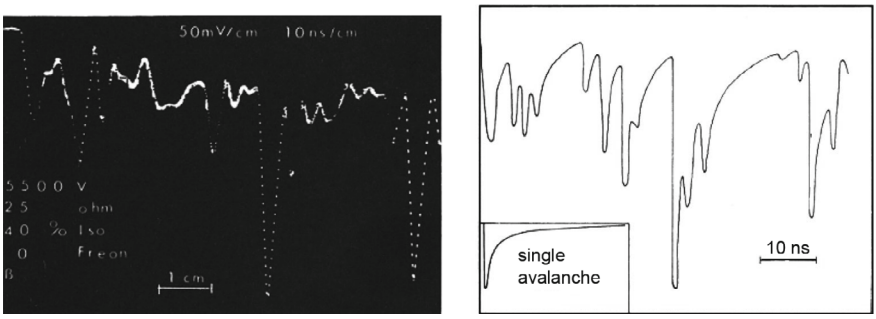

Fig. 4.5 Left: Voltage pulses from a proportional chamber recorded with an oscilloscope. Right: Simulation of avalanching secondary electrons expected in a multi-wire proportional chamber. Both reprinted with kind permission from [18], © 1975, CERN. All rights reserved

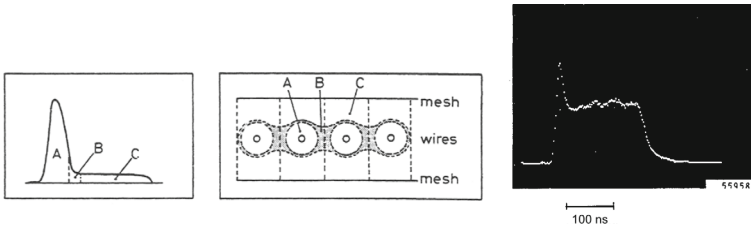

Fig. 4.6 Left: Typical signal pulse of an MWPC wire. Center: Three regions contribute to the signal pulse, the fast drift region (A), the intermediate region (B) and a smooth drift region (C). Both reprinted under CC-BY-3.0 Licence from [17], ©1977–2024, CERN. Right: Measured time distribution of a signal pulse for an inclined beam of minimum ionizing electrons. The observed signal on the anode is induced by the ions slowly moving away from the wire. Reprinted with kind permission from [20], © 1973, Elsevier. All rights reserved

while electrons produced in region C, on the other hand, smoothly drift to the anode where they are amplified and collected. The time resolution of a chamber is defined as the minimum gate width needed on the readout electronics for full efficiency. It is typically around 30 ns for 2 mm wire spacing. Figure 4.6 (right) shows the typical time distribution measured on a single wire for an inclined beam of minimum-ionizing electrons. The long uniform tail in this case corresponds to tracks crossing region C of the considered wire. Here, the gate was set to 160 ns. Optimizing the gate width reduced a large fraction of electrons from region C.

4.1.2 Design Considerations

The rule of thumb for the construction of MWPCs is to choose an anode wire diameter, which is about 1% of the anode wire pitch. Thus, for 2 mm pitch we choose a wire diameter of $d_w \simeq 20\ \mu$m. Above, we listed the capacitance per unit length for these dimensions and an 8 mm anode-cathode gap. Since the spatial resolution in an MWPC improves with smaller pitch (see Fig. 4.3), we would like to place anode wires as close

as possible next to each other. However, large MWPCs with an anode wire pitch of less than 2 mm become difficult to operate. For example, an MWPC with 1 mm anode wire pitch and anode wires 20 μm in diameter has $C_w = 1.99$ pF/m. To achieve a similar gain as for an MWPC with an anode wire pitch of 2 mm, we have to keep the charge per unit length $V_0 C_w$ constant. This would require doubling V_0, which would double the electric field in the drift region, bringing us closer to the Raether condition (3.31). Decreasing the anode wire diameter would help, but we would run quickly into mechanical instabilities and electrostatic limitations. Note that chambers with 30 cm^2 sensitive area, 1 mm anode wire spacing, 6–8 mm anode-cathode gaps and gold-plated W wires 20 μm in diameter were operated successfully using a gas mixture of argon-isobutane-freon (79.5:20.0:0.5) at $\sim$ 7 kV [21]. For large ($>$ 1 m^2) MWPCs, typical parameters are [22]: anode wire spacing $s_w = 2$ mm, anode-cathode gap $a_w = 6$–8 mm and anode wire diameter $d_w = 20$ μm.

Standard anode wires are made of gold-plated tungsten or aluminum. The former material is less fragile but adds more inactive material into the chamber reducing the effective radiation length. This increases the probability for both photon conversions that produce new avalanches and elastic and inelastic scattering of the heavy charged particle. In most multipurpose detectors one tries to minimize the inactive material in order to optimize the momentum resolution. Cathode planes are made of stretched metal foil, metal strips or wires such as Cu-Be wires 50–100 μm in diameter. Many wires up to 100 may be ganged together to save readout channels. The chambers are held by rigid light frames typically made of honeycomb plates, G10 or fiber glass containing printed circuit boards. Aluminum frames serve as rigid support structures.

The counting gas in MWPCs typically consists of noble gases (Ar, Kr, Xe) with admixtures of CO_2, methane (CH_4), isobutane (iC_4H_{10}), ethylene (C_2H_4) or ethane (C_2H_6). In addition, often small portions of methylal ($C_3H_8O_2$) are added for quenching and freon (CF_3Br) or ethylbromide (C_2H_5Br) for reaching high amplifications $>10^7$ without breakdown. The so-called magic gas is an argon-isobutane-freon mixture where the argon fraction is 70–80%, the isobutane fraction is 30–20% and the freon concentration is 0.15–0.4% [23].

The chamber is kept at a certain pressure. So, the volume has to be sealed and kept at constant temperature. The wires and pads are soldered to feedthroughs at the inner wall, which take out the signals and transfer them to preamplifiers. A high electric field is used to reach typical gas amplifications of $10^5 - 10^6$ in the proportional region. The detection efficiency depends on the high voltage and the gate width as shown in Fig. 4.7 (left). Above a certain field strength the detection efficiency reaches a constant value called plateau, which is typically several 100 V wide. Here, chambers are operated with efficiencies near 100%. The gas amplification also depends on the anode wire diameter as shown in Fig. 4.7 (right).

The starting value of the plateau depends on the readout such as the selected gate, a time window during which the signal is collected. Shorter gates yield a better signal-to-noise ratio at reduced efficiency. For wider gates, the plateau is reached at lower electric-field strengths than for shorter gates. The characteristics of the plateau also depends on the gas amplification and the threshold of the amplifier attached to each wire. Typical thresholds are 200–500 μV. Note that at very high electric-field

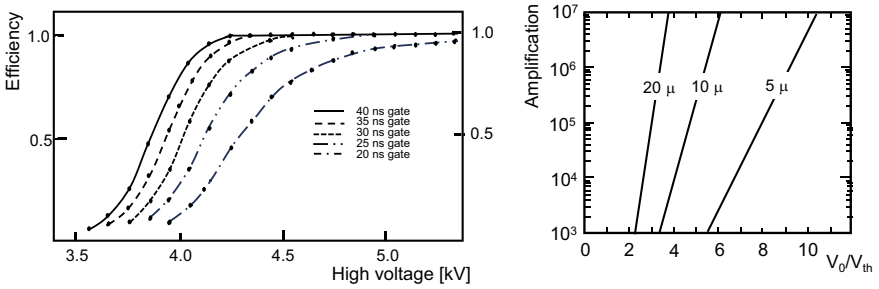

Fig. 4.7 Left: Detection efficiency as a function of applied high voltage for different gate widths of the signal readout electronics. Reprinted with kind permission from [24], © 1971, Elsevier. All rights reserved. Right: The amplification of a proportional chamber as a function of the ratio of operational voltage V_0 to threshold voltage V_{th} for different anode wire radii. Reprinted under CC-BY-3.0 License with kind permission from [17], © 1977–2024, CERN

strengths a chamber breakdown may occur via sparking. Sparking may burn carbon paths on the fiber glass chamber frame. If this occurs, the chamber is shorted and will not operate any longer. Discharges can also lead to anode wire breakage.

4.1.3 Electric-Field Distortions

Distortions of the electric-field due to displaced wires or varying wire diameter affect the performance. Figure 4.2 (right) shows the electric-field configuration and equipotential lines for a set of anode wires where the fifth wire is displaced upward modifying the anode-cathode gap. Displacements in the x direction change the pitch. Other effects include changes of the cathode position and variations of the strip/wire size. To estimate the gain changes caused by variations of the wire radius and wire positions, we differentiate (3.29), obtaining

$$\frac{\Delta A}{A} = \ln A \frac{\Delta Q}{Q}. \tag{4.8}$$

We can compute $\Delta Q/Q$ in terms of tolerances in the wire radius and variations in the anode-cathode gap. Recalling that $Q = C_w \cdot V_0$ with C_w given in (4.3), we obtain

$$\frac{\Delta Q}{Q}|_{d_w} = \frac{C_w}{2\pi\epsilon_0}\frac{\Delta d_w}{d_w}, \tag{4.9}$$

$$\frac{\Delta Q}{Q}|_{a_w} = \frac{C_w}{2\epsilon_0}\frac{a_w}{s_w}\frac{\Delta a_w}{a_w}, \tag{4.10}$$

$$\frac{\Delta Q}{Q}|_{s_w} = \frac{C_w}{2\pi\epsilon_0}\left(1 - \frac{\pi a_w}{s_w}\right)\frac{\Delta s_w}{s_w}. \tag{4.11}$$

Consider for example a typical chamber with parameters $a_w = 8$ mm, $d_w = 20\ \mu$m, $s_w = 2$ mm and a gain of 10^6. The gain changes become

$$\frac{\Delta A}{A}|_{d_w} \approx 0.9\frac{\Delta d_w}{d_w}, \tag{4.12}$$

$$\frac{\Delta A}{A}|_{a_w} \approx 11\frac{\Delta a_w}{a_w}, \tag{4.13}$$

$$\frac{\Delta A}{A}|_{s_w} \approx 10\frac{\Delta s_w}{s_w}. \tag{4.14}$$

Thus, a 1% change in the wire diameter leads to a 0.9% change in the gain while a 1% wire shift in the x and y directions yields a 11% and 10% gain change, respectively. Figure 4.8 (left) shows the effect of a displacement of wire 0 in the x-direction on $\Delta Q/Q$ for wire 0 and neighboring wires. The effects on wires ± 1 are largest. The relative charge change on wire 0 is smaller than that on wires ± 2. For a gain of 10^6 and a displacement of 0.1 mm, this introduces charge changes of about 0.8% on wires ± 1 and about 0.2% on wires ± 2, leading to gain changes of 9% and 2%, respectively. Figure 4.8 (right) shows the effect of the displacement of wire 0 in the y-direction on $\Delta Q/Q$ for wires 0 and 1. Here, the effect on wire 0 is largest. For a 0.25 mm displacement the change in $\Delta Q/Q$ is 1% leading to a gain change of 10%.

A problem specific to large chambers is the mechanical instability of anode wires due to electrostatic repulsion. If an anode wire is slightly displaced from the middle plane by $\delta_z > 0$ due to an inaccurately drilled hole, it will be pulled more into the positive than the negative z direction. The wire tension counteracts the electrostatic force. In large chambers at high potential, however, the wires will buckle even if the wires are positioned perfectly. If wire 0 is pulled up, wires ± 1 will be pulled down as illustrated in Fig. 4.9. The wires are no longer straight but take a parabolic shape, so that the displacement is largest at half the wire length. The charges induced on neighboring wires are opposite. The critical length of a chamber for wire stability was calculated in reference [25]. The magnitude of the force between two equal

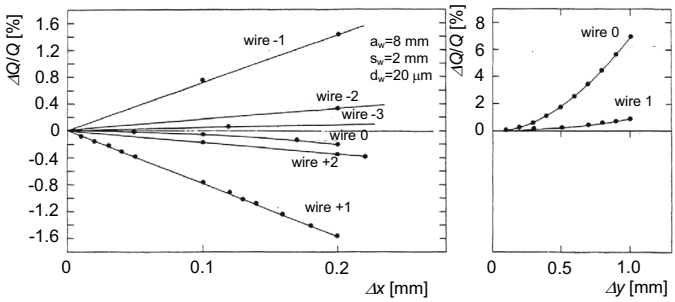

Fig. 4.8 Left: The $\Delta Q/Q$ variation in different wires caused by a displacement of wire 0 in the x-direction. Right: The $\Delta Q/Q$ variation in wires 0 and 1 caused by a displacement of wire 0 in the z-direction. Both reprinted under CC-BY-3.0 License with kind permission from [17], © 1977–2024, CERN

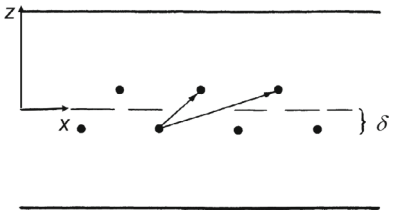

Fig. 4.9 Wire displacements due to electrostatic instabilities in a large MWPC (> 1 m) in the x-z plane. Reprinted under CC-BY-3.0 License with kind permission from [17], © 1977–2024, CERN

linear charges $C_w V_0$ at a distance r per unit length in which the electric field is given by (4.6) and is not modified due to the small displacement δ_z is

$$F(r) = \frac{(C_w V_0)^2}{2\pi\epsilon_0}\frac{1}{r}. \tag{4.15}$$

The total force on a given wire per unit length perpendicular to the wire plane is given by [25],

$$\sum F_\perp = 2\frac{(C_w V_0)^2}{2\pi\epsilon_0}\left\{\frac{1}{s_w}\frac{2\delta_z}{s_w} + \frac{1}{3s_w}\frac{2\delta_z}{3s_w} + ...\right\} = \frac{\pi(C_w V_0)^2}{4\epsilon_0}\frac{\delta_z}{s_w^2}. \tag{4.16}$$

If T_w is the mechanical tension of the wire, the restoring force perpendicular to the wire plane is

$$F_\mathrm{R} = T_w \frac{\mathrm{d}^2\delta_z}{\mathrm{d}y^2}, \tag{4.17}$$

where $\delta_z = \delta_z(y)$ is the displacement of the wire along its length with boundary conditions of $\delta_z(0) = \delta_z(\ell_w) = 0$ if ℓ_w is the total wire length. In equilibrium, the restoring force compensates $\sum F_\perp$, yielding

$$T_w \frac{\mathrm{d}^2\delta_z}{\mathrm{d}y^2} = -\frac{\pi(C_w V_0)^2}{4\epsilon_0}\frac{\delta_z}{s_w^2}. \tag{4.18}$$

The solution of the second-order differential equation is

$$\delta_z(y) = \delta_0 \sin\left(\frac{C_w V_0}{2s_w}\sqrt{\frac{\pi}{\epsilon_0 T_w}}y\right). \tag{4.19}$$

The boundary condition $\delta_z(\ell_w) = 0$ allows us to determine the required tension

$$\frac{C_w V_0}{2s_w}\sqrt{\frac{\pi}{\epsilon_0 T_0}}\ell_w = \pi, \tag{4.20}$$

yielding

$$T_0 = \frac{1}{4\pi\epsilon_0}\left(\frac{C_w V_0 \ell_w}{s_w}\right)^2. \tag{4.21}$$

We achieve a stable condition if

$$T_m > T_w > T_0 = \frac{1}{4\pi\epsilon_0}\left(\frac{C_w V_0 \ell_w}{s_w}\right)^2, \tag{4.22}$$

where T_0 is the tension defined by the parameters of the chamber and T_m is the elastic limit. The other parameters are the same as those in (4.1). So, the critical stability length is given by

$$\ell_c = \frac{s_w}{C_w V_0}\sqrt{4\pi\epsilon_0 T_m}. \tag{4.23}$$

For example, for a typical MWPC with $d_w = 20\ \mu$m, $s_w = 2$ mm and $a_w = 8$ mm the elastic limit of the wire is $T_m = 0.65$ N for $V_0 = 5$ kV yielding a critical length of about $\ell_c = 90$ cm. Since the elastic limit decreases with the diameter of the anode wire as d_w^2, the critical wire length is proportional to d_w. For larger chambers we need a mechanical support. One solution is to weave a thin nylon wire across the anode wires perpendicular to their direction. However, the electric field $\vec{E}$ of the anode wires is disturbed in the region near nylon wire causing an inefficient zone of 5 mm width around the nylon wire. In some very large chambers, solid support bars have been used.

Another effect of the electrostatic forces in an MWPC is the overall attraction of the cathode planes towards the anode planes reducing the gap in the center of the chamber. The calculation is tedious and thus omitted here. An approximation is given in [12]. For our typical chamber with parameters listed above, the maximum deflection is 220 μm for $V_0 = 4.5$ kV.

4.1.4 Performance

Multi-wire proportional chambers are robust, reliable, easy-to-build and rather inexpensive large-area detectors, which yield reasonable position resolutions. Thus, they have been used in many experiments. Figure 4.10 (left) shows a schematic view of a large self-supporting MWPC [26]. The frame consisted of fiber glass. This chamber used three layers with wires running horizontally in the first plane, vertically in the second plane and at an angle of 15° in the third plane. The counting gas was an argon-isobutane gas mixture (80:20) plus methylal as quencher. Using an amplifier threshold of 5 mV on a 3.3 kΩ resistor and a gate width of 60 ns, the plateau at 100% efficiency was larger than 700 V. The operating voltage was 4.7 kV. A spatial resolution of $\sigma_x = 0.6/\cos\lambda_d$ mm was measured where $\lambda_d = 90° - |\theta|$ is the dip angle. The gas gain depends on the ratio of operational voltage to threshold voltage and on the anode wire diameter. For thicker wires the same gain is achieved with a lower V_0/V_{th} ratio. An another large MWPC (200 cm × 50 cm) was built and tested at CERN by a different group [24]. Figure 4.10 (right) shows a photograph of an LHCb MWPC.

Table 4.1 summarizes parameters and properties of MWPCs used as tracking detectors in some high-energy physics experiments. In some experiments the

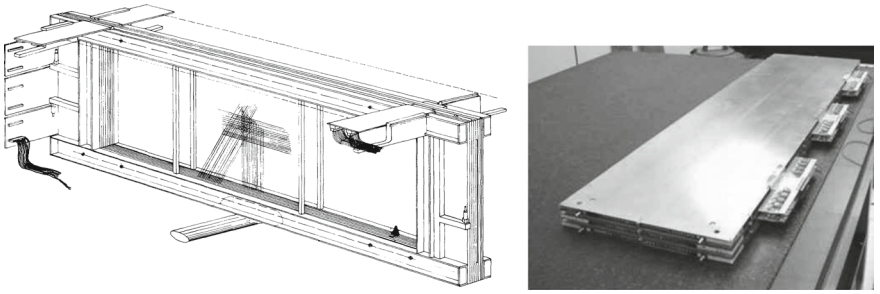

Fig. 4.10 Left: View of a large MWPC (39 cm × 154 cm). The chamber has three independent gaps with sense wires running horizontally, vertically and at 15° with respect to the vertical axis. Reprinted with kind permission from [22], © 1971, Elsevier. All rights reserved. Right: Photograph of an LHCb MWPC used for the muon system. This chamber is in the first muon layer (M1) in the outermost region (R4), which has dimensions of 20 cm × 96 cm. A total of 192 chambers covers the R4 region in layer M1. Reprinted with kind permission from [28], © 2008, IOP Publishing. All rights reserved

MWPCs are used for the trigger in the tracking or muon systems. So, here the spatial resolution is compromised for a reduced number of readout channels as seen in the SELEX experiments and the LHCb muon system. The best performance is achieved with Charpak's MWPC, which measured a spatial resolution of 45 μm in the direction along the anode wires. Next, we consider the Large-Area Solenoid Spectrometer (LASS) experiment [27] at SLAC.[1] The upgraded experiment used three planar and six cylindrical MWPCs. For planar chambers the wires were parallel to the upper frame edge while the cathode strips had a 45° stereo angle with respect to the anode wires. For the cylindrical chambers a small stereo angle was provided by helical cathode strips at ±10° for chambers 1–4 and ±15° for chambers 5 and 6. The LASS MWPCs achieved a reasonable spatial resolution. The second MWPC system was installed into the NA24 experiment [29] at CERN.[2] For tracking they used five layers of 1 m × 1 m and three layers of 2 m × 2 m MWPCs.

The SELEX experiment [30] at Fermilab[3] used three sets of MWPCs for tracking. Each set consisted of multiple chambers with multiple layers, having both axial (X,Y) and stereo (U,V) layers. The stereo angle was ±28.07°. The gold-plated tungsten sense wires were spaced at a 2 mm pitch, which was increased to 3 mm in some chambers. The HERMES experiment [31] at DESY[4] used three planes of MWPCs in the magnet region. The Cello experiment used cylindrical proportional chambers that were positioned in the tracking system [32]. The LHCb experiment used 1380

[1] LASS operated 1976–82 using 11 GeV/c charged kaon beams to study strange and non-strange lower-mass resonances.
[2] NA24 was a prompt photon production experiment operating with 300 GeV/c pion and proton beams 1980–84.
[3] SELEX studied properties of charmed baryons operating 1996–97.
[4] HERMES studied the proton spin at HERA running from 1995–2007.

Table 4.1 Properties of some MWPCs used in sub-detectors of different experiments listing the sensitive area in $x \times y$ for planar chambers and radius/length for cylindrical chambers, maximum unsupported sense wire length (ℓ_w), anode-cathode gap (a_w), sense wire diameter (d_w), sense wire spacing (s_w), cathode wire/strip spacing (c_w), high voltage, gas mixture and position resolution ($\sigma_{x(r\phi)}/\sigma_{y(rz)}$). The area denotes the sensitive area. The magic gas is a mixture of Ar-isobutane-methylal-freon in a ratio (∼75:21:4:0.25). The upper part of the table shows planar chambers and the lower part cylindrical chambers. For planar chambers, the position resolution denotes σ_x and σ_y if the y position is measured. For cylindrical chambers, the position resolution refers to $\sigma_{r\phi}$ and σ_z. X and Y are vertical and horizontal planes while U and V are stereo layers with angles of $\pm 28.07°$. [†]The resolution is measured with X-rays; replacing argon with xenon improves the spatial resolution to 35 μm. [&]All chambers have two planes of cathode readout with strips arranged under $\pm 45°$ stereo angles. [#]In the central region three planes have anode wire spacing of 1 mm. [‡]The first pair is for the innermost region of station M3, the second pair is for the outermost region of M2; for all other regions σ_x and σ_y lie between these boundaries. [##]In muon stations M2 (M3) in the inner regions wires are combined to strips with sizes 6.3 mm (6.7 mm) and 12.5 mm (13.5 mm). [*]SELEX also has smaller MWPCs in magnets M2 and M3. [⋆]Listed are the smallest and largest pad sizes of the cathode planes; in the the different regions of the muon stations anode wires, cathode pads or both are read out. [§]This is for layers 1–4; for layers 5 and 6 the length is 87 cm

Experiment system	sens. area [cm × cm]	ℓ_w/a_w [cm]/[mm]	d_w [μm]	s_w/c_w [mm/mm]	HV [kV]	gas (fractions)	$\sigma_{x,r\phi}/\sigma_{y,z}$ [mm/mm]
Charpak [38,41] X, Y	small	–/8	10	1–2/0.5	3.9	Xe-$HC(CH_3)_3$–$C_3H_8O_2$ (55:38:7)	0.15–0.3/ 0.045[†]
LASS [27,44][&] gap PWC	155 × 155 3 chambers	31.5/5.1	20	2[#]/8.1	6.0	magic gas	≤ 0.3/ ≤ 0.3
NA24 [29] 3 × (X, Y, U, V)	200 × 200	66/6	25 75	3/–	2.97	Ar-CO_2-freon (80:20:0.15)	0.87 (wire)/
SELEX M1 [30] 3 × (X, Y, V, U)	200 × 200[*]	70/6	25	3/–	3.0	Ar-C_4H_{10}-freon (75:24.5:0.5)	0.6/–
LHCb [45] Muon M1–M5	30 × 25 to 129.6 × 27	30/2.5	30	1.5[##]/ 37.5 × 31.3[⋆] 54 × 270[⋆]	3.15	Ar-CO_2-CF_4 (40:55:5)	10/12[‡] to 60/100[‡]
HERMES MC1 –MC3 [31,46]	99.6 × 26.3 142.4 × 34.7	–/4	25	2/0.5	2.85	Ar-CO_2-CF_4 (65:30:5)	0.7/0.7
LASS [27,44] Cylindrical	6–49 × 100[§] 6 layers	50 & 43.5/ 4.8–5.8	20	2/5–10	6.0	magic gas	≤ 0.3/0.7–1.5 wire: 0.6
Cello [32] tracking	17-70 × 220 5 layers	220/4	20	2.09–2.86 /4.5	2.1	magic gas	0.179/ 0.44

MWPCs in five stations[5] of the muon system [28] with 276 chambers in each station, which is subdivided further into four regions. The cathode planes use pad or wire-pad readouts. Multi-wire proportional chambers have been used also as readout systems in other sub-detectors, for example, in Ring-Imaging Cherenkov detectors [33,34] and in time projection chambers [35–37].

4.1.5 Position Measurement

One plane of an MWPC in which the cathodes are not read out provides a position measurement only in the direction perpendicular to the wires (x). To measure x and y positions simultaneously, we need two chambers with anode wires planes placed perpendicular to each other. Another option is to make the cathode out of wires or metal strips that run orthogonal to the anode wires and that are also read out. Figure 4.11 (left) shows the layout of an MWPC with cathode readout [38,39]. The upper (lower) cathode has wires running parallel (perpendicular) to the anode wires. To reduce the number of readout channels, six cathode wires are ganged together while all anode wires are connected. Typically, anode wires are read out individually, in groups or not at all. In this chamber the x and y position measurements come from the cathode wires. Pulses are induced on the cathode wires by the positive ions. The magnitude varies with the distance between the avalanche position and the wire. On each readout line the size of the signal is sketched. Cathode wires produce positive pulses with signal heights decreasing with distance from the ionization point while the anode wires produce a negative pulse. Figure 4.11 (right) shows another layout of an MWPC with cathode readout. Here, the anode wires run under a stereo angle while the top and bottom cathode strips run in the x and y directions, respectively. In this chamber all wires and strips are read out. While only one anode wire records the signal, several x and y cathode strips see the signal allowing for a precise position measurement.

The x position is determined by the center-of-gravity (COG) method either using the charge recorded on individual anode wires or cathode strips running parallel to the wires [39],

$$x = \frac{\sum_i (Q_i - b) x_i}{\sum_i (Q_i - b)}, \tag{4.24}$$

where Q_i is the charge measured on wire or strip i at position x_i and b is a small bias level offset to correct for noise. Typically, the offset is determined from a fit to the data. Similarly, the y position is obtained by using the cathode strips running perpendicular to the anode wires,

$$y = \frac{\sum_j (\tilde{Q}_j - \tilde{b}) y_j}{\sum_j (\tilde{Q}_j - \tilde{b})}, \tag{4.25}$$

[5] For run 2 layer M1 was removed.

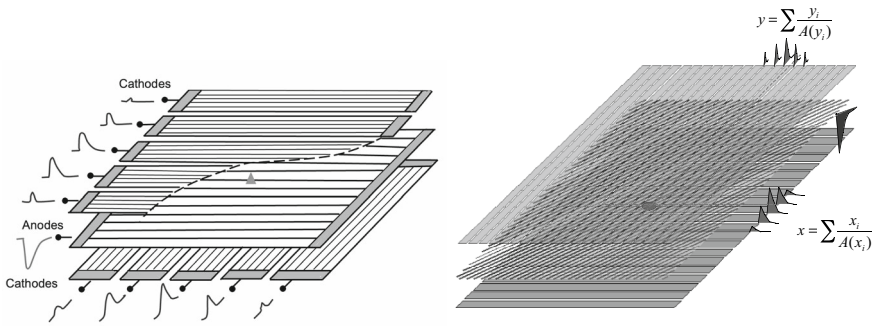

Fig. 4.11 Left: Schematic view of an MWPC with cathode readout [40,41]. The upper (lower) cathode strips run parallel (perpendicular) to the anode wires. To reduce the number of readout channels, all anode wires and rows of six cathode strips are combined. The triangle shows the position of the primary ionization. Reprinted with kind permission from [41], © 1978, Elsevier. All rights reserved. Right: Schematic view of an MWPC in which all anode wires running under a stereo angle and cathode strips running in x and y directions are read out. Note that the cathode strips see charge distributions on both strips in the x and y directions while only one anode wire records a signal. Reprinted with kind permission from [42], © 2014, F. Sauli. All rights reserved

where $\tilde{b}$ is another offset and y_i is the strip position in the y direction.

Another algorithm for determining the position is the head-tail algorithm, which is used for solid state detectors [43].

$$x = \frac{x_R + x_L}{2} + \frac{Q_R - Q_L}{2\bar{Q}} s_w, \tag{4.26}$$

where $x_{R,L}$ are the positions of the right- and left-most pixel, $Q_{R,L}$ are their measured charges, $\bar{Q}$ is the average charge and s_w is the wire or strip pitch.

Charpak measured the position resolution using three chambers. The chambers were equipped with gold-plated tungsten wires 15 μm in diameter that were spaced at a 2.54 mm pitch [39,41]. The cathode planes used wires 100 μm in diameter separately spaced every 1.27 mm. The chambers were operated with a magic gas mixture at 3.9 kV. The two outer chambers defined the expected position. From the measured position in the central chamber residuals were extracted. The anode-cathode gap was 5 mm and the chamber had an active area of 100 mm $\times$ 100 mm. Charpak used 1.5 GeV/c test beam particles to study the chamber performance. Figure 4.12 (left) shows the residual distribution as a function of the y position. The distribution is uniform and has residuals of 100 μm at FWHM. This leads to a spatial resolution in y direction of 45 μm. Replacing argon with xenon leads to a further improvement in position resolution of 35 μm. Figure 4.12 (right) shows the charge distribution versus y position for the same MWPC operated with a xenon gas mixture. The MWPC recorded collimated soft X-rays that were moved twice by 200 μm.

Figure 4.13 (left) shows the correlation of the measured versus true center-of-gravity x position. There is clearly a clustering effect visible although charge sharing between adjacent wires introduces a certain amount of interpolation and a moderate

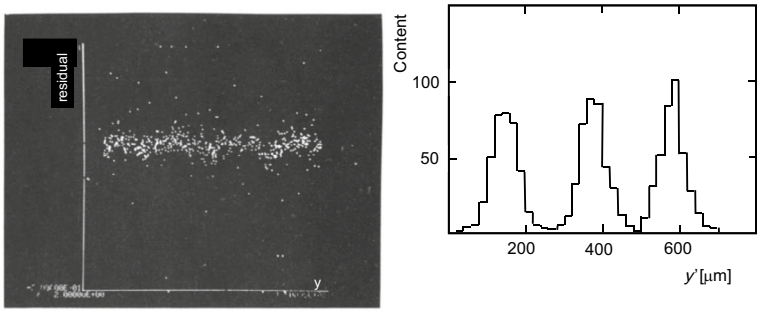

Fig. 4.12 Left: Measured residuals in the y direction along the anode wire for uniform irradiation of the chamber. The vertical dispersion has a FWHM of 100 μm. Reprinted with kind permission from [39], © 1979, Elsevier. All rights reserved. Right: Charge distribution of a proportional chamber with cathode readout irradiated with a 1.4 keV X-ray source at three positions separated by 200 μm. Reprinted with kind permission from [41], © 1978, Elsevier. All rights reserved

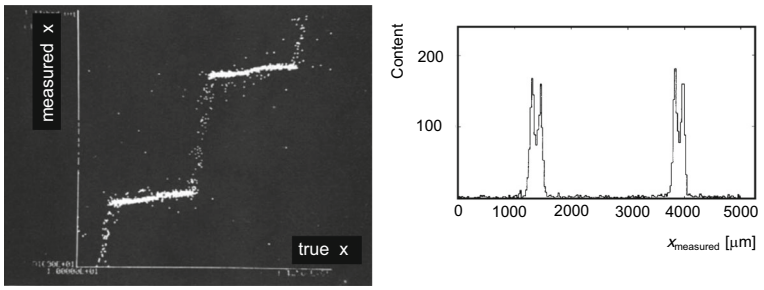

Fig. 4.13 Left: Correlation of the true (horizontal) and measured coordinate in the x direction for uniform irradiation perpendicular to the chamber. Note the quantization effect of the anode wires on the center-of-gravity. Right: Projection of the correlation plot onto the vertical axis showing clearly the left-right separation as two partially overlapping peaks. Both reprinted with kind permission from [39], © 1979, Elsevier. All rights reserved

slope of the clustering caused by the left-right effect. This becomes clearer if we look at the projection of the scatter plot on to the vertical axis as depicted in Fig. 4.13 (right). The two peaks correspond to tracks that cross the anode plane at the right-hand side and left-hand side of the wire, respectively. We can unfold the clustering effect by combining the left-right identification with the drift time measurement,

$$\Delta x = \pm v_d^e \Delta t, \tag{4.27}$$

where Δt is the drift time measurement and $v_d^e = 5.2\,\mathrm{cm}/\mu\mathrm{s}$ is the drift velocity. After correcting the measured position using (4.27) we obtain a linear relation between true and measured positions as shown in Fig. 4.14 (left), which in turn improves the spatial resolution to 120 μm as shown in Fig. 4.14 (right). If the spatial resolution is just taken from the COG distribution, we obtain $\sigma_x = 200$ μm [39].

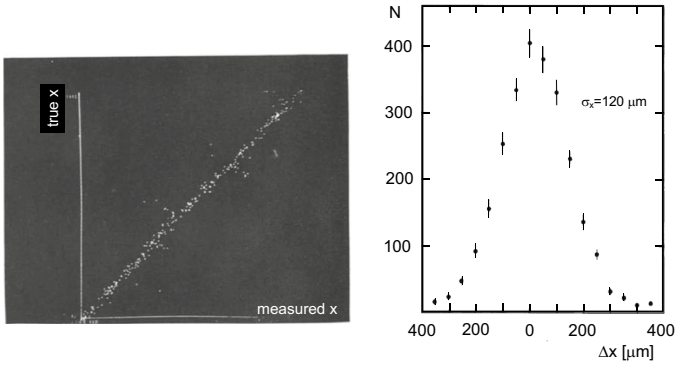

Fig. 4.14 Left: Correlation of the measured versus true x coordinate after corrections based on the drift time. Please note that the horizontal and vertical axes are interchanged with respect to the correlation plotted in Fig. 4.13 (left). Right: Distribution of measured minus true x position after combining the right-left identification given by the COG method with the drift-time measurement. Both reprinted with kind permission from [39], © 1979, Elsevier. All rights reserved

Without cathode readout, the position along the wire can be obtained via charge division requiring readout of both wire ends. For charge measurements Q_A and Q_B on the two ends of a wire, we obtain the position along the wire

$$y = \ell_w \frac{Q_A - b}{Q_A + Q_B - 2b}, \tag{4.28}$$

where ℓ_w is the wire length. The accuracy of the y position is $\sim 0.4\%$ of the wire length, which is much worse than reading out cathode strips directly.

4.1.6 Gas Chamber Aging

The operating gas of an MWPC typically contains organic components like methane or higher C_nH_{2n} molecules. Under the conditions of avalanche formation, the organic molecules dissociate and may form radicals. For example, electrons may trigger reactions like $e^- + CH_4 \rightarrow CH_2 + H_2 + e^-$ as depicted in Fig. 4.15 (left). The CH_2 radicals are ready to polymerize and form higher-complexity molecules containing chains of carbon and hydrogen, which can be liquid or solid. They may form whiskers on the cathode or polymers that get stuck on the anode wire. Figure 4.15 (right) schematically shows polymer chain formation by CH_2 radicals. Figure 4.16 (left, center) show whiskers growth on anode wires. Figure 4.16 (right) shows deposits on the cathode.

Figure 4.17 sketches the different aging effects on the anode and cathode. Deposits on the anode may be conductive (C) or insulating. This leads to an effective increase of the wire diameter, which in turn leads to a gain reduction (see Fig. 4.17 (left)). On the cathode the formation of a thin insulating layer causes an accumulation of i^+ that are produced in an avalanche (see Fig. 4.17 (center left)). The ion neutralization is slowed down depending on the resistivity. The high dipole field created by the ions may result in an emission of electrons from the cathode into the gas (see Fig. 4.17 (center)). This

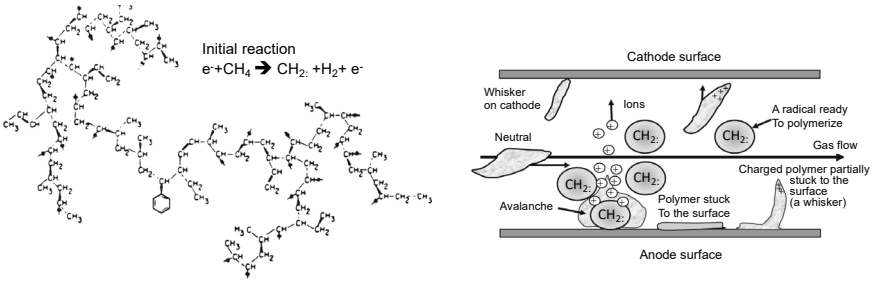

Fig. 4.15 Left: Initial reaction of $e^- + CH_4 \rightarrow CH_{2:} + H_2 + e^-$, where $CH_{2:}$ is a radical. Right: Polymer chain formation started by a CH_2 radical. Both reprinted with kind permission from [47], © 2001, J. Va'vra. All rights reserved

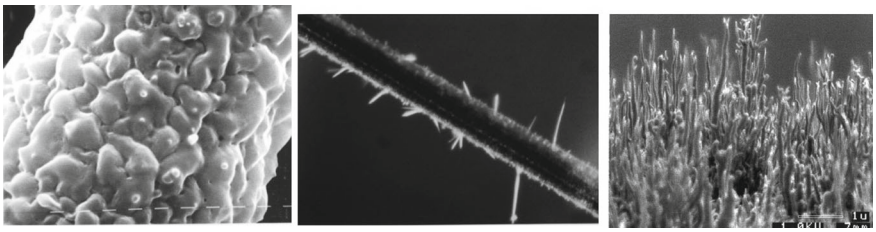

Fig. 4.16 Left: Formation of polymers on the anode wire. Reprinted with kind permission from [48], © 1986, LBNL. All rights reserved. Center: Growth of spikes on the anode wire. Reprinted with kind permission from [49], © 1986, LBNL. All rights reserved. Right: Silicon growth on the cathode. Reprinted with kind permission from [50], © 2003, Elsevier. All rights reserved

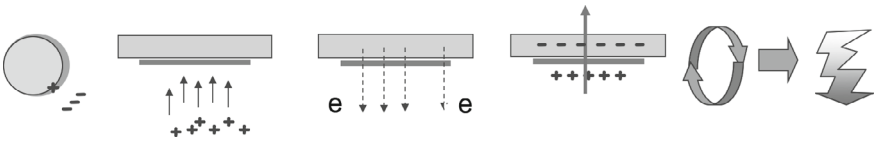

Fig. 4.17 Left: Deposits on the anode wire lead to an increase of the wire diameter, which in turn lead to a gain reduction. Center left: The formation of a thin insulating layer causes an accumulation of positive ions that are produced in an avalanche. Center: The high dipole field created by the ions may result in an emission of electrons from the cathode into the gas called Malter effect [51]. Center right: These electrons generate more avalanches near the anode and thus produce more ions that eventually reach the cathode accumulating on the deposit. Right: When the ion production rate exceeds the neutralization rate, the conditions become unstable and may lead to sparking. All reprinted with kind permission from [52], © 2009, F. Sauli. All rights reserved

is called the Malter effect [51]. These electrons generate more avalanches near the anode and thus produce more ions that eventually reach the cathode accumulating on the deposit (see Fig. 4.17 (center right)). When the ion production rate exceeds the neutralization rate, the conditions become unstable and may lead to sparking (see Fig. 4.17 (right)), which eventually destroys the chamber. So, the use of non-organic gases avoids the formation of Carbon-based polymers.

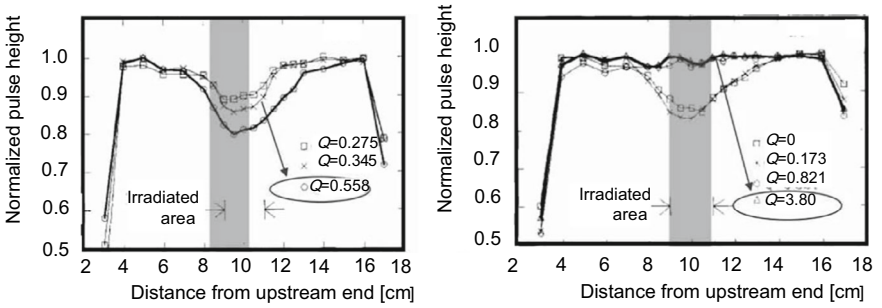

Fig. 4.18 Left: The measured pulse height in an Ar-C_2H_6 mixture after irradiation showing a loss in pulse height in the irradiated region already at low doses. Right: The measured pulse height in a CF_4-iC_4H_{10} gas mixture. Even for high irradiation levels the pulse height remains unaffected. Both reprinted with kind permission from [53], © 1991, Elsevier. All rights reserved

Adding carbon tetrafluoride (CF_4) into gas mixtures is attractive because of its fast drift velocity, low diffusion coefficient and low neutron cross section. Since CF_4 is very reactive, it prevents polymer formation and even removes existing deposits. The etching is particularly efficient for Si compounds. Note that CF_4 is used by the semiconductor industry to etch silicon and SiO_2 [54]. However, the relative balance between polymer formation and etching is difficult to control. Fluorine radicals released in avalanches can combine with water to form HF, which is a strong acid that attacks glass, epoxy and wires. Figure 4.18 (left) shows the measured pulse height in an Ar-C_2H_6 mixture after irradiation. Even for low dose, the pulse height in the irradiated area drops by 10%. For twice the dose it drops by 20%. This is different for a CF_4-iC_4H_{10} gas mixture as shown in Fig. 4.18 (right). Even for high irradiation the pulse height is unaffected. The chamber region that showed irradiation effects when operated without the CF_4 admixture, looks fine after adding CF_4. Further details of MWPCs are given in [42].

4.2 Planar Drift Chambers

In the development of MWPCs, it was realized that spatial information could be obtained also by measuring the drift time of electrons coming from an ionizing event. Note that Charpak used drift time information in improving the spatial resolution with respect to the center-of-gravity method. The start time t_0 is the time when the primary ionization occurs and it is correlated with the time when an interaction occurred. The stop time t_1 is time when the electron enters the high electric field generating an avalanche, which is correlated with the rising edge of the anode pulse. For the drift time $\Delta t = t_1 - t_0$ the drift distance is obtained by

$$z = \int_{t_0}^{t_1} v_d^e(t)\mathrm{d}t, \tag{4.29}$$

where $v_d^e(t)$ is the magnitude of the electron drift velocity. For constant drift velocity the integral simplifies to

$$z = v_d^e(t_1 - t_0) = v_d^e \Delta t. \tag{4.30}$$

Constant drift velocity is obtained from a constant electric field. Note that this cannot be achieved in a conventional proportional chamber because of the zero field region between anode wires. We need to introduce a field wire at negative high voltage between anode wires. Here, we obtain almost a linear relation between drift time and drift path. Figure 4.19 shows the drift field and isochrones (contours of equal drift time) of a drift chamber (bottom) in comparison to that of an MWPC (top). Whereas the MWPC has no field lines in the middle between two anode wires, the drift chamber does. In a large region of a drift cell the electric-field lines are parallel producing a homogeneous field. This is achieved by inserting field wires around the anode wire. This principle was noticed by the Charpak [13] and Walenta-Heintze groups [55].

A complete linear relation requires an $\vec{E}$ field as constant as possible over the entire drift space. This is achieved with different configurations. Here, we present two examples. Figure 4.20 shows a grid of field wires that surround the anode wire. The potential is adjusted linearly from zero near the anode to -HV1 at both ends of the drift cell. The anode wire is kept at positive high voltage (few kV). As indicated by the equipotential lines this produces a constant electric field except in the vicinity of the anode wire. Figure 4.21 shows another configuration in which cathode planes are kept at a fixed potential but a shaping potential is created inside the cell by an appropriate number of field wires. The anode is kept at 3.7 kV while the cathode is at –2.0 kV. Figure 4.22 shows the equipotential lines in one quadrant of the latter drift cell. The electrons see a nearly constant field in the entire drift cell except near

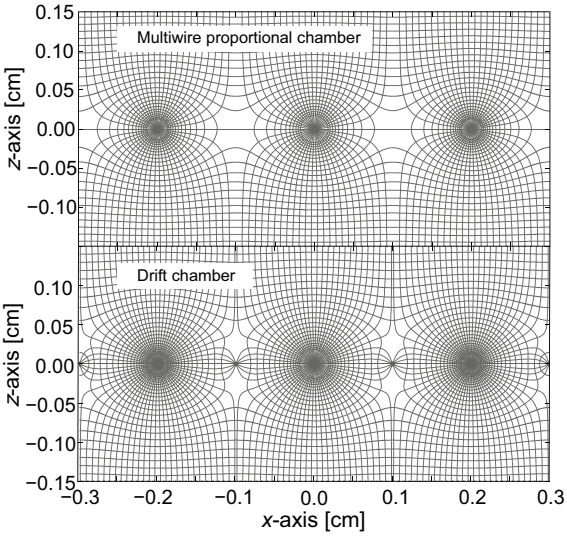

Fig. 4.19 Top: Electric-field lines and isochrones in an MWPC. Bottom: Electric-field lines and isochrones in a drift chamber. While in an MWPC there is a field-free region between two sense wires, this is not the case in a drift chamber due to the field wires. Reprinted under CC-BY-NC-4.0 Licence with kind permission from [56], © 2024, the Particle Data Group LBNL

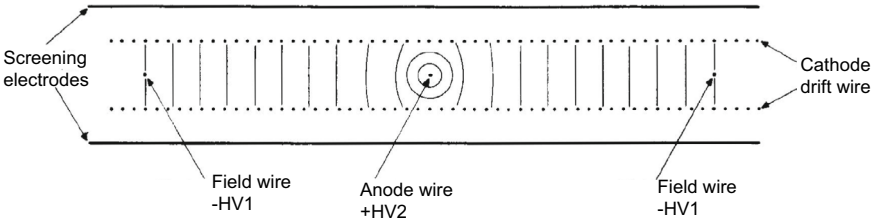

Fig. 4.20 Drift cell consisting of a grid of field wires that surround an anode wire. The potential is adjusted linearly from zero near the anode to -HV1 on the left and right ends of the drift cell. Reprinted with kind permission from [57], © 1975, Elsevier. All rights reserved

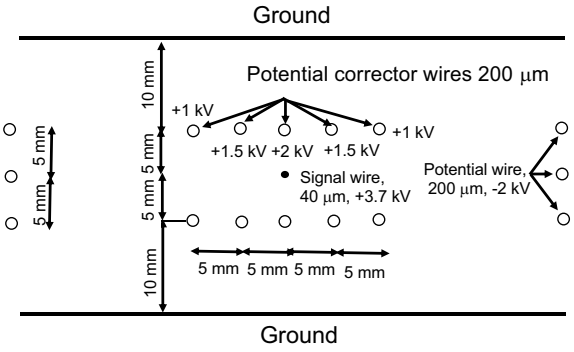

Fig. 4.21 Drift cell in which the cathode planes are kept at a fixed potential. The shaping potential inside the cell is built up by an appropriate number of field wires. Reprinted with kind permission from [58], © 1977, Elsevier. All rights reserved

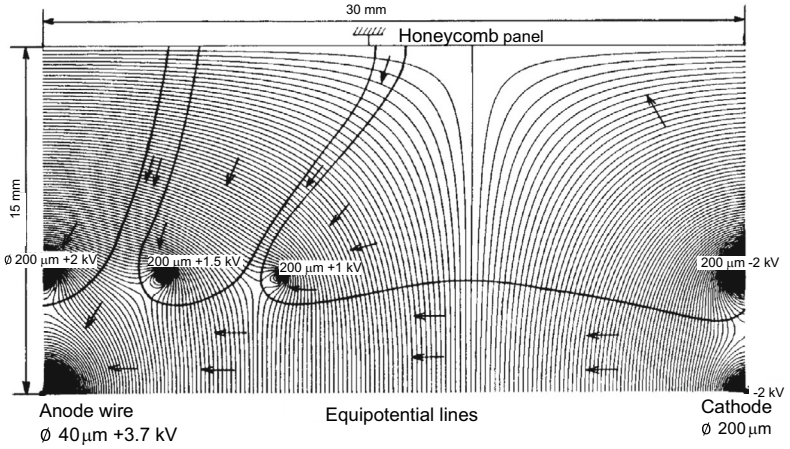

Fig. 4.22 Equipotential lines and electron drift directions (arrows) for the drift cell configuration in Fig. 4.21. Reprinted with kind permission from [58], © 1977, Elsevier. All rights reserved

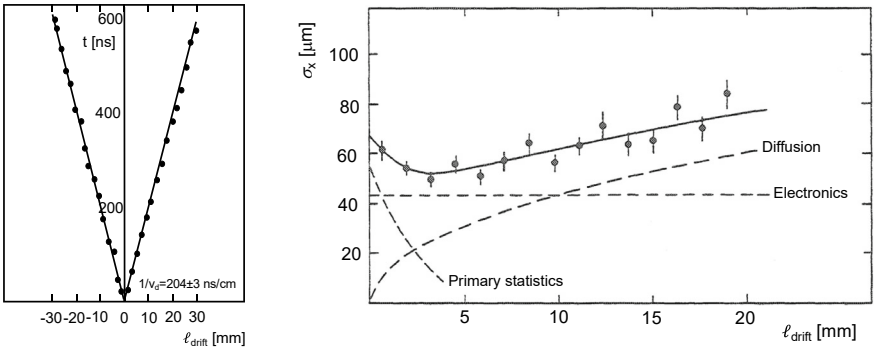

Fig. 4.23 Left: Time-to-distance relation for the drift cell configuration in Fig. 4.21. Reprinted with kind permission from [58], © 1977, Elsevier. All rights reserved. Right: Position resolution for the drift cell in Fig. 4.21 as a function of the drift distance for measurements (points) and a fit (solid line). The contributions from electron statistics, diffusion and electronic dispersion are shown also by dashed lines. Reprinted under CC-BY-3.0 License with kind permission from [17], © 1977–2024, CERN

the cell boundaries and close to the anode wire. The arrows indicate the electron drift direction. Figure 4.23 (left) shows measurements of the drift time versus drift distance. The measurements verify that the relation between drift time and drift distance is linear across the entire cell. While the field wires are just used to define the electric field inside the drift cell, the anode wires carrying the signal are read out.

Another important issue is the choice of gas for various reasons:

(i) The dependence of the drift velocity on the electric field: this is important for obtaining a linear relation between drift path and drift time. For some gas mixtures, v_{d}^{e} is nearly independent of $|\vec{E}|$ (see Fig. 2.48). For example, in a gas mixture of Ar-C_4H_{10} (80:20) the drift velocity is nearly independent of the electric field in the region $0.5 \leq |\vec{E}| \leq 2.0$ kV/cm. If we operate drift chambers in a configuration in which v_{d}^{e} does not depend on $|\vec{E}|$, field inhomogeneities and changes in temperature, pressure and operating voltage become less important.
(ii) Gas purity: we need to eliminate electro-negative gases.
(iii) Magnitude of the drift velocity: high drift velocities are useful for operating a drift chamber at high rates to minimize the dead time. So it is useful to use gas mixtures containing CF4. Slower drift velocities help to optimize the spatial resolution since timing errors are minimized. So here, gas mixtures containing DME, CO_2 or He-C_2H_6 are useful.

4.2.1 Drift Chamber Properties

Large planar drift chambers consist of many (100) such drift cells. Typically different layers are arranged in one chamber. The anode wires run in different directions, e.g. in x direction, y direction and under stereo angles. Thus, these chambers measure

Table 4.2 Examples of planar drift chambers including the large planar drift chambers of the CDHS detector, three drift chamber planes of the NA32 experiment used in the electron spectrometer, the middle muon chambers (MM) of the L3 experiment and the planar drift chambers in the forward track detector (FTD) of the H1 experiment. The notation is $w \times \ell$ for width×length of an individual chamber, total area for the total coverage with chambers in the detector, number of sense wires per cell, number of cells per chamber, sense wire spacing s_w, diameter of a sense wire/grid wire d_w/d_c, maximum drift length ℓ_{drift}, type of z-measurement, gas type, gas type fractions, electric-field strength $|\vec{E}|$, magnetic-field strength $|\vec{B}|$, drift velocity v_{d}^e, efficiency, position resolution in x, double track resolution and resolution in the time-to-distance relation σ_t. †The drift chambers DC1 and DC2 have six layers (X, Y, U, V, X, Y) and (Y, X, U, V, Y, W) while DC3 has five layers (Y, XU, V, W), where the stereo angles are $U = 45°$, $V = -45°$ and $W = 15°$. ‡This is the typical efficiency; individual channels were lower

Experiment	CDHS [58,59]	NA34† [60]	L3 [61,62]	H1 [63–66]
System	Tracking	e^- spectrometer	Muon MM	FTD (planar)
$w \times \ell$ [cm × cm]	400 × 400	DC1: 24 × 49.5	163 × 556	disk: $r_i = 14$
	hexagonal	DC2: 50.4 × 43 DC3: 75.6 × 34	3 layers	$r_o = 78.5$
Total area m^2	720	0.4	∼ 730	5.6
# sense wires/cell	1	6 or 8	16 & 24	4
# cells/chamber	130	8–18	16	32
s_w [mm]	60	6	9	6.0
d_w/d_c [μm/μm]	40/200	20/100	30/75	40/125
ℓ_{drift} [mm]	30	15–21	50	28.1
z-coordinate	Stereo	Stereo	Spec. cham.	Spec. cham.
Gas type	Ar-iC_4H_{10}	CO_2-C_2H_6	Ar-C_2H_6	Ar-C_3H_8
Gas fractions	(70:30)	(90:10)	(62:38)	(90:10)
$\vec{E}$ field [kV/cm]	≥ 1.9	1.2	1.14	5.0
$\vec{B}$ field [T]	0	0	0.51	1.14
v_{d}^e [cm/μs]	4.9	0.89	4.9	0.42
Efficiency [%]	99.5	>99	>99	∼96‡
σ_x [μm]	<700	60	110–210	150–170
$\sigma_{2-\text{track}}$ [mm]	10	0.6	–	<2
σ_t [ns]	12	2	–	–

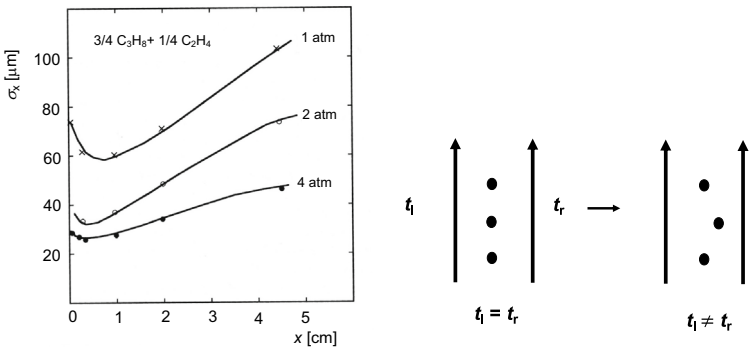

Fig. 4.24 Left: Position resolution as a function of the drift distance for different gas pressures. Reprinted with kind permission from [68], © 1978, Elsevier. All rights reserved. Right: Arrangement of sense wires to break the left-right ambiguity

x, y directions with similar spatial resolution. The construction of large planar drift chambers is done in a similar way as that of MWPCs. In a drift cell, we encounter a left-right ambiguity. A track passing the anode wire on the left-hand side cannot be distinguished from one passing on the right-hand side. One possibility to resolve this issues is to look at the field wires. The field wires on the side the track passed through will see an induced signal earlier than those on the other side [55]. So, by reading out the field wires we can resolve this ambiguity. Another possibility is to stagger the anode wires, which breaks the left-right symmetry (see Fig. 4.24 (right)). Table 4.2 summarizes properties of four planar drift chambers used in the CDHS,[6] NA32,[7] L3 and H1 experiments as examples.

4.2.2 Drift Chamber Performance

To estimate the efficiency of a chamber we can use a naive statistical argument. A charged particle traversing the chamber produces an average number n_c of collisions on its path. The probability for producing the actual number k is given by Poisson statistics [20]:

$$P_k^{\mathrm{n_c}} = \frac{n_c^{\mathrm{k}}}{k!} \exp\left(-n_c\right). \tag{4.31}$$

So, the inefficiency that not a single electron-ion pair is produced is given by $P_0^{\mathrm{n_c}} = \exp\left(-n_c\right)$ and in turn the chamber efficiency

$$\epsilon_{ch} = 1 - \exp\left(-n_c\right). \tag{4.32}$$

[6] CDHS was a neutrino experiment at CERN taking data 1976–84.
[7] NA32 was a charm production experiment at CERN taking data 1982–86.

If we target an efficiency larger than 99%, this implies $\exp(-n_c) < 0.01$ yielding $n_c \geq 5$. So, for five collisions the efficiency is 99.3%. Since this is satisfied for most chambers, drift chambers typically operate with high efficiency. The first chamber built by Walenta [55] reached an efficiency of 98.6%. In many chambers operated in various experiments the efficiency is better than 99%. The aging issues we discussed with respect to MWPCs also hold for drift chambers. A first step is to add water vapor, which improved operations in several chambers.

In smaller chambers, the position resolution is determined by the knowledge of the time-to-distance relation, the diffusion of electrons during their migration towards the anode and a constant electronics dispersion. For large-area chambers ($\geq 100\,\mathrm{m}^2$) mechanical tolerance in positioning the wires ($100 - 300\ \mu$m) and sagging of the wires under their own weight come in addition. Thus, the spatial resolution of a small chamber is given by

$$\sigma_x^2 = \left(\frac{c_{ion}^2}{N_{ion}^2 \cdot x^2}\right) + \frac{2D_e}{v_{\mathrm{d}}^e} \cdot x + \sigma_{\mathrm{noise}}^2, \tag{4.33}$$

where c_{ion} is a constant, N_{ion} gives the number of primary ions produced by a charged track in a cell, D_e is the electron diffusion coefficient defined in (2.144) and v_{d}^e is the magnitude of the electron drift velocity. The first term is determined by the number of produced primary ions, which dominates at small drift distances and drops inversely with the drift distance and N_{ion}. The second term accounts for the diffusion of electrons increasing with drift distance while the third term results from electronic noise. Note that in magnetic fields the diffusion coefficient is reduced by $(1 + \omega_B^2 \tau_e^2)^{-1}$.

Figure 4.23 (right) shows the position resolution for the drift cell in Fig. 4.21 as a function of the drift distance. The data were obtained by measuring the same track in a set of equal chambers, performing a fit to the data in each chamber, calculating the deviation between data and the fits and determining the standard deviation of the differences. The best position resolution is achieved at a drift distance of ~ 4 mm. The ultimate accuracy that can be obtained in a drift chamber depends both on the good knowledge of the time-to-distance relation and on the diffusion properties of electrons in gases. Figure 4.24 (left) shows the position resolution as a function of the drift distance for different gas pressures. At four atmospheres the position resolution improves significantly. The best average resolutions of 60 μm and 120 μm have been achieved in the Na34 [60] and H1 [67] experiments, respectively.

4.3 Cylindrical Drift Chambers

In colliding-beam experiments usually solenoidal magnetic fields around the beam pipe are used. In cylindrical coordinates the magnetic-field components are $B_r = B_\phi = 0$, $B_z \neq 0$. Since charged particles feel a force perpendicular to the $\vec{B}$ field, the charged-particle momentum is deflected in the $r\phi$ plane while their z component remains unaffected. Since the beam line is along the z direction, beam particles are

left undisturbed. Detectors need to follow the cylindrical geometry. In planar drift chambers we use square cells. In cylindrical drift chambers, drift cells are arranged in cylindrical layers. The $\vec{E}$ field lies in the $r\phi$ plane, perpendicular to axial $\vec{B}$ field. It is generated by a suitable arrangement of potential wires, which run parallel to each other surrounding a single anode wire or a group of anode wires that are read out. A large fraction of layers (typically $\geq$50%) have wires running parallel to the magnetic field. They are called axial layers. The remaining layers have wires running skew under stereo angles, which are typically $\pm$ few degrees with $\vec{B}$ field axis and which are called stereo layers. For each signal wire we have to measure t_0, the beginning of the primary ionization and the time-to-distance relation. If signal wires are radially aligned, we encounter a left-right ambiguity. This problem is solved by staggering signal wires, thus breaking the radial symmetry as shown in Fig. 4.24 (right). To reduce the number of field wires, closure of the drift cell in radial direction can be omitted. Such a setup is called open-cell geometry. Here, the homogeneity of the $\vec{E}$ field and linear relation of the drift path to drift time deteriorate.

Axial wires only measure $r\phi$ positions. From the stereo layers we obtain the z information. The determination of the three-dimensional space point is a two-step process. First, we determine the $r\phi$ position from the axial wires and perform a track fit. In the second step, we use the measurements of the stereo layers. We move the z position until the $r\phi$ position matches that of the fit curve. Then the fit is repeated with the information of the stereo layers included. From the best fit the z-positions are obtained.

4.3.1 Conceptual Chamber Design

A cylindrical drift chamber conceptually consists of two circular endplates, an inner cylinder and an outer cylinder which are sealed and filled with gas. Typically, the endplates are made out of aluminum. Precision holes are drilled into the endplates into which feedthroughs are inserted. On the inside sense wires or field[8] wires are soldered. On the outside the sense wires are connected to the readout electronics and high voltage, while field wires are connected to high voltage. The inner cylinder typically consists of a light-weight material such as beryllium, fiber glass or carbon fiber, while the outer cylinder is made of carbon fiber or aluminum. The stringing of the chamber is done with a special winding machine. The endplates are fixed at the correct distance with the inner cylinder in place. The winding machine strings one wire at a time that is correctly tensioned and soldered to the feedthrough. The drift chamber consists of many cylindrical layers, some of which are axial while others are stereo layers. Sense wires typically consist of stainless steel, gold-plated tungsten, rhenium-plated tungsten, or aluminum. They have diameters of 20-30 μm while potential wires and guard wires are much thicker (40–170 μm), typically consisting of gold-plated tungsten, copper-beryllium or aluminum.

[8] Field wires are called also potential wires.

4.3.2 Chamber Properties

The cylindrical drift chamber has been the most widely used tracking detector in colliding-beam experiments. Large-area detectors can be built rather inexpensively, which provide good position resolution in the $r\phi$ plane, $\sigma_{r\phi}$. Using stereo layers, the resolution in the z direction is worsen by

$$\sigma_z = \sigma_{r\phi} / \sin(\alpha_{\text{st}}), \tag{4.34}$$

where α_{st} is the stereo angle. Since for small stereo angles the sine term is of the order of 0.1, the rz resolution is typically a factor of ten worse than the $r\phi$ resolution.

The cell structure provides constant electric fields over nearly the entire drift cell. For example, the experiments MARK III [69,70], TASSO [71,72], ARGUS [73], SLD [74,75], CLEO [76], *BABAR* [77,78], Belle/Belle II [79,80], and CDF [81,82] used a central drift chamber as their main tracking detector. For these experiments, we list properties and performance parameters in Table 4.3. Note that all these experiments have been completed. Drift chambers are used also in several active experiments, such as BES III [83], COMET[9] [84] and the upgraded MEG II[10] detector [85]. However, we refer the interested reader to the cited publications.

Drift chamber efficiencies are very high and spatial resolutions of large chambers are typically 100–250 μm. Please note that the SLD and Belle II drift chambers achieve the best $r\phi$ resolutions of 55–110 μm and 50–120 μm, respectively. While the ARGUS experiment built the largest chamber, the *BABAR* experiment built the smallest. The CDF drift chamber had the largest number of measurements while the TASSO drift chamber had the smallest. The two-track separation is a few mm. Note that all drift chambers provide ionization measurements for each sense wire, which is used for particle identification. This information basically comes for free and will be discussed this in more detail in Sect. 9.1. Before we discuss alignment, track finding and track reconstruction procedures, we present some more details of the TASSO and *BABAR* drift chambers.

4.3.3 The TASSO Drift Chamber

One of the first cylindrical drift chambers, which was built for the Tasso experiment [71], had nine axial and six stereo layers using one-type of open cell structure shown in Fig. 4.25 (left). Three field wires defined the cell size in ϕ while cells were open in the radial direction. However, five separating cylinders made of aluminized Rohacell divided the chamber into six radial compartments. This enhanced

[9] COMET is a muon-to-electron conversion experiment at J-Park that has started data taking in 2022.

[10] The MEG II experiment at the Paul Scherrer Institute, which looks for the lepton-number-violating $\mu \to e\gamma$ decay, started data taking in 2021.

Table 4.3 Examples of cylindrical drift chambers showing the inner radius r_i, outer radius r_o, chamber length $\ell_{\rm dc}$, number of sense wires $N_{\rm sw}$, number of sense wires per cell, cell structure, number of field wires $N_{\rm fw}$, sense wire material, diameter of the sense wire $d_{\rm w}$, field wire material, diameter of the field wire $d_{\rm fw}$, maximum number of measurements $N_{\rm max}$, stereo angle $\alpha_{\rm st}$, maximum drift distance $\ell_{\rm drift}$, method of z measurement, gas mixture, gas fraction, electric-field strength $|\vec{E}|$, magnetic-field strength $|\vec{B}|$, drift velocity $v_{\rm d}^e$, spatial resolution range in $r\phi$, mean spatial resolution in $r\phi$, $\mathrm{d}E/\mathrm{d}x$ resolution [86] and relative transverse momentum resolution $\sigma_{p_{\rm T}}/p_{\rm T}^2$. For the momentum resolution typically all tracking systems are used. *The first value refers to layer 2 and the second value to layers 3–8. †The first layer had 15 wires per cell (12 sense wires) whereas the remaining six layer had 5 wires (3 sense wires) per layer. ‡Both field wire types are gold-plated. §This holds for all but the innermost superlayer, where the electric field is 2.3 kV/cm. #The resolution depends on the drift distance and is best in the center of the cell and poor at the edges

Exp.	MARK III	TASSO	ARGUS	SLD	CLEO II	*BABAR*	Belle II	CDF II
Ref.	[69,70]	[71,72]	[73,87]	[74,75]	[76]	[77,78]	[79,80],	[81,82]
r_i [cm]	14.5	36.7	30	20	17.5	23.6	16	40
r_o [cm]	114.3	122.2	172	100	94.5	80.9	113	137
$\ell_{\rm dc}$ [cm]	177.8/233.7*	352	200	200	215	276.4	232.5	310
$N_{\rm sw}$	2,000	2,340	5,940	5,120	12,240	7,104	14,336	30,240
$N_{\rm sw}$/cell	12/3†	1	1	8	1	1	1	12
Cell	Open	Closed	Closed	Open	Closed	Closed	Closed	Open
$N_{\rm fw}$	2,000	7,020	24,588	32,640	36,240	45,000	42,240	39,840
Sense wire	Au-W	Au-W	Au-W	Au-W	Au-W	W-Re	Au-W	Au-W
$d_{\rm w}$ [μm]	20	30	30	25	20	20	30	40
Field wire	Cu-Be	Au-Mo	Cu-Be	Au-Al	Al/Cu-Be	Al‡	Al	Au-W
$d_{\rm fw}$ [μm]	175	120	75	150	110	120	126	40
$N_{\rm max}$	30	15	36	80	51	40	56	96
$\pm\alpha_{\rm st}$ [°]	$^{+7.7}_{-9.0}$	3.36–4.5	2.4–4.8	2.48	3.77–6.89	2.6–4.2	2.7–4.6	2.0
$\ell_{\rm drift}$ [cm]	1.81–2.99	1.6	1	5	0.7	0.6–0.8	0.8–1.8	0.88
$z_{\rm meas}$	$^{\rm stereo}_{\rm Q-div}$	Stereo	Stereo	$^{\rm stereo}_{\rm Q-div}$	Stereo	Stereo	Stereo	Stereo
Gas Mixture	Ar-CO_2 -CH_4	Ar-CH_4	C_3H_8-C_3H_3OH	Ar-CO_2-iC_4H_{10}	Ar-C_2H_6	He-iC_4H_{10}	He-C_2H_6	Ar-CF_4--iC_3H_8
Fraction [%]	89:10:1	90:10	97:3	21:75:4	50:50	80:20	50:50	50:15:35
$\lvert\vec{E}\rvert$ [$\frac{\rm kV}{\rm cm}$]	0.8	1.54	1–2	0.9	1	1.96	1.26§	1.9–2.4
$\lvert\vec{B}\rvert$ [T]	0.4	0.5	0.76	0.6	1.5	1.5	1.5	1.41
$v_{\rm d}^e$ [$\frac{\rm cm}{\mu\rm s}$]	5.1	~ 2.5	4–5	0.79	1	2.2	3.3	8.8
$\sigma_{r\phi}$ [μm]			100–400	55–110		100–250	50–120	100–200
$\langle\sigma_{r\phi}\rangle$ [μm]#	250/220*	220	190	92	290			140
$\frac{\sigma_{\mathrm{d}E/\mathrm{d}x}}{\mathrm{d}E/\mathrm{d}x}$ [%]	15.0	–	5.0	7.0	6.2	6.9	5.0	10.0
$\frac{\sigma\, p_{\rm T}}{p_{\rm T}^2}$ [$\frac{c}{\rm GeV}$]	0.015	0.02	0.009	0.005	0.0026	0.0013	0.00127	0.0015

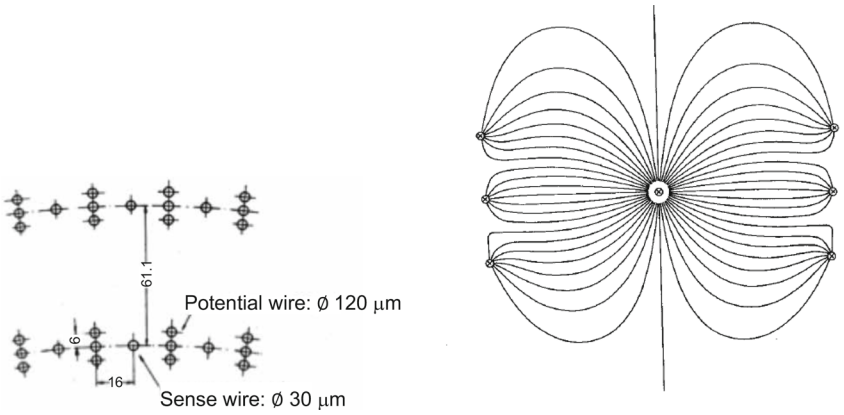

Fig. 4.25 Left: The open drift cell structure of the Tasso drift chamber. Right: The electric-field lines in the Tasso drift cell. Both reprinted with kind permission from [72], © 1978, Elsevier. All rights reserved

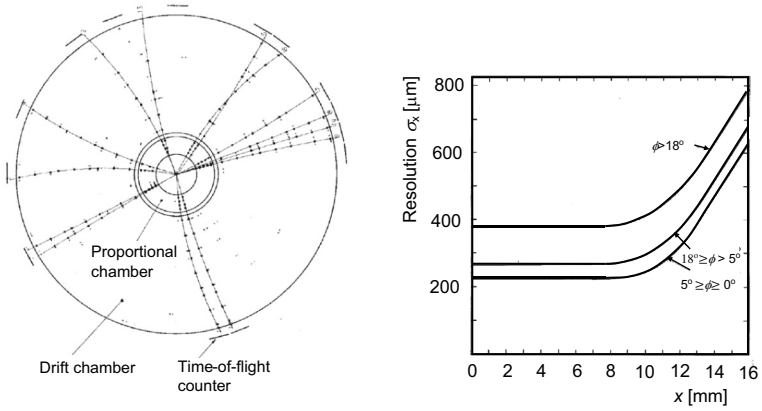

Fig. 4.26 Left: A hadronic event measured with the Tasso drift chamber. The points represent $r\phi$ position measurements and the solid curves show track fits. Right: The position resolution in the Tasso drift chamber as a function of drift length for different dip angles. Both reprinted with kind permission from [72], © 1980, Elsevier. All rights reserved

operational stability in case of broken wires as these would be confined to one compartment. The electric-field lines are displayed in Fig. 4.25 (right), which are quasi parallel over a wide range of the cell.

Figure 4.26 (left) depicts a hadronic event at 35.8 GeV in which only hits in the axial layers are displayed without background removal. Individual tracks from charged particles are visible. Events are rather clean. The solid lines show the fitted tracks. The transverse momentum is extracted from the curvature (see Chap. 6). Figure 4.26 (right) shows the position resolution as a function of drift distance for different entrance angles measured with Bhabhas and hadronic events. In the $r\phi$

plane a position resolution of $\sigma_{r\phi} \simeq 200\ \mu$m is achieved for small entrance angles. For inclined tracks the position resolution becomes worse. For dip angles of $>18°$, the resolution is nearly twice as large.

4.3.4 The *BABAR* Drift Chamber

The *BABAR* drift chamber consists of 40 cylindrical layers arranged into 10 superlayers with four layers each, covering the radial region from 20 cm to 80 cm [77]. Figure 4.27 (left) shows a schematic layout of the ten superlayers. The innermost superlayer is an axial layer followed by a stereo layer with positive stereo angles (U-layer) and a stereo layer with negative stereo angles (V-layer). This pattern is repeated three times followed by an axial layer as outermost superlayer. Figure 4.27 (center) shows an enlarged view of the four innermost superlayers. Typically, a cell consists of one sense wire surrounded by six field wires where the sense wire is kept at 1.96 kV while the field wires are at ground potential. For inner and outer cells of each superlayer, the inner and outer field wires are replaced by two guard wires kept at 340 V. Figure 4.27 (right) shows the electric-field lines and isochrones of cells in layers 3 and 4 of an axial superlayer. Sense wires are tungsten-rhenium wires 20 μm in diameter and 2.75 m long while field wires are gold-plated aluminum wires 120 μm in diameter. The drift chamber is 2.8 m long and is operated with a He-iC_4H_{10} (80:20) gas mixture plus 0.4% water vapor at a pressure of 4 mbar. The endplates, which carry an axial load of $\sim 32,\ 000$ kN, are made of aluminum. The inner cylinder is a 1 mm thick beryllium structure, the outer shell consists of a 1.6 mm thick carbon-fiber structure. The inactive material in the *BABAR* drift chamber corresponds to $1.08\% \cdot X_0$. Some photographs of the *BABAR* drift chamber are depicted in Figure 4.28. The first photograph (top left) shows the stringing of the chamber. The wires are attached onto the feedthroughs on one endplate. The stringing machine drives them to the other endplate, where they are tensioned, cut and soldered to the feedthroughs. The arrangement of the feedthroughs is depicted on the bottom left. The photograph on the top right shows the completely strung drift chamber and that on the bottom right depicts the drift chamber after the outer shell had been put on.

Figure 4.29 (left) shows the drift distance versus drift time relation. Note that the dependence is not linear across the entire cell. For a drift distance less than 3 mm a linear relation gives a good approximation. In addition, there is a small asymmetry between the left-hand side and the right-hand side of the drift cell for drift times larger than 200 ns. However, since the time-to-distance relation is known, precise position measurements are possible. Figure 4.29 (right) shows the track efficiency as a function of transverse momentum (top right) and a function of the polar angle (bottom right). For an operating voltage of 1960 V, the efficiency is above 97% for $p_T > 400$ MeV/c and polar angles greater 0.5 radian.

Figure 4.30 (left) shows the position resolution inside a drift cell. The average resolution is $\sigma_{r\phi} = 125\ \mu$m. The best resolution is found in the center of the chamber yielding $\sigma_{r\phi} = 100\ \mu$m. Using the Kalman fitter method discussed in Sect. 5.2.4, we determine the track parameters, transverse impact parameter (d_0), longitudinal

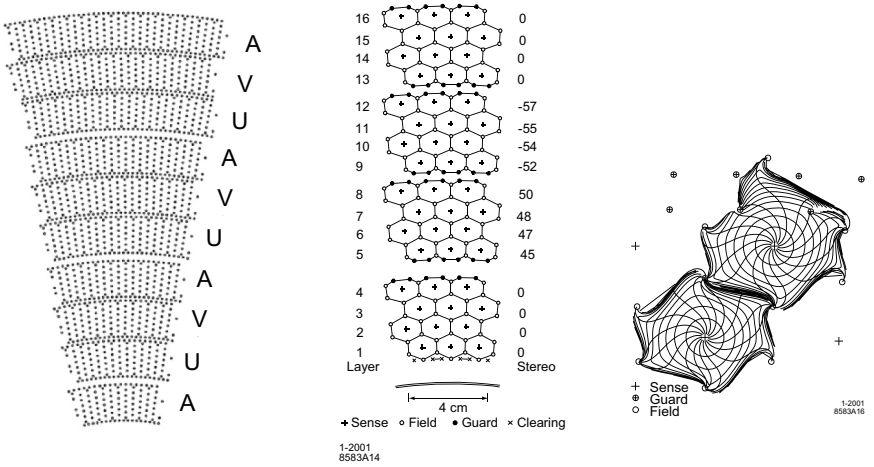

Fig. 4.27 Left: Radial layout of the *BABAR* drift chamber, which consists of ten superlayers arranged in alternating axial *A*, stereo *U* and stereo *V* superlayers and so on. Center: Enlarged view of the first four superlayers. Right: Electric-field lines and isochrones of a drift cell in layers 3 and 4 of an axial superlayer. All cells are closed small drift cells that have six field wires. Inner and outer cells have additional guard wires. All reprinted with kind permission from [88], © 1998, Elsevier. All rights reserved

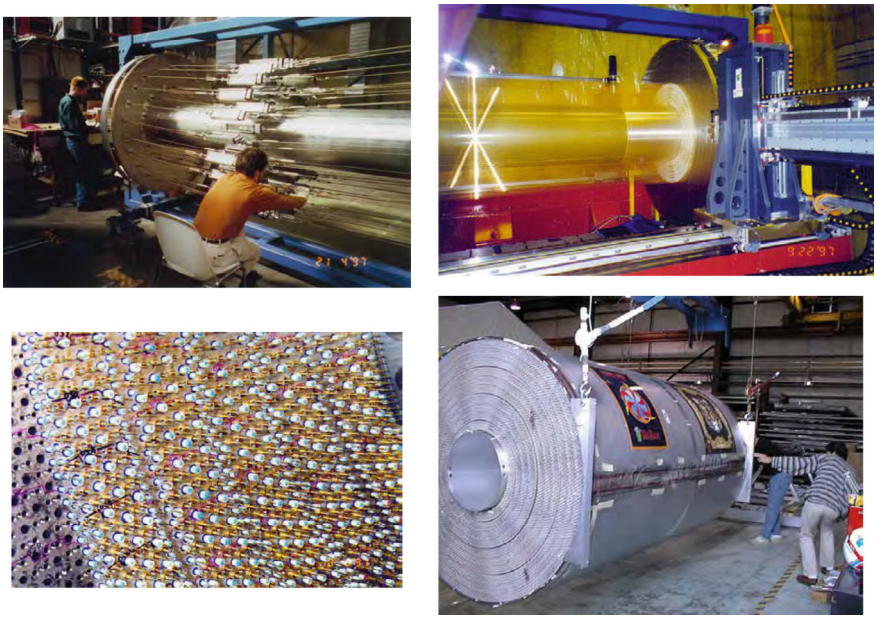

Fig. 4.28 Top left: Stringing of the *BABAR* drift chamber. Top right: The *BABAR* drift chamber after completion of stringing. Bottom left: A view of the feedthroughs on an endplate of the *BABAR* drift chamber. Bottom right: The completed *BABAR* drift chamber. All reprinted with kind permission from [89], © 2000, the *BABAR* Collaboration. All rights reserved

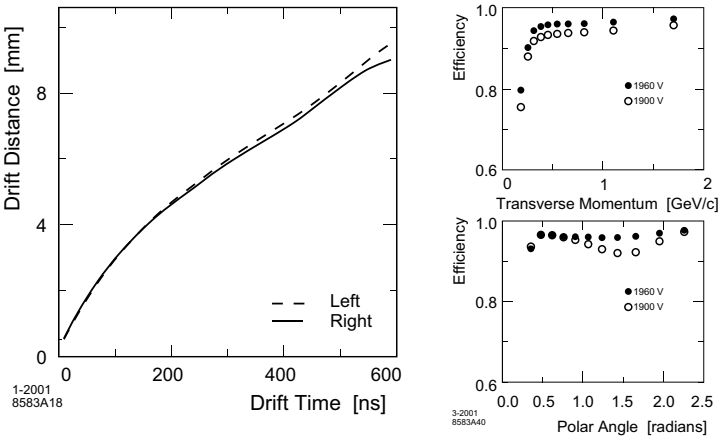

Fig. 4.29 Left: The time-to-distance relation for a *BABAR* drift cell. Top right: Efficiency versus transverse momentum. Bottom right: Efficiency versus polar angle. There is a slight asymmetry between the left-hand side (dashed) and the right-hand side (solid) of the *BABAR* drift cell. The solid (open) points show the efficiency for an operating voltage of 1960 V (1900 V). All reprinted with kind permission from [77], © 2002, Elsevier. All rights reserved

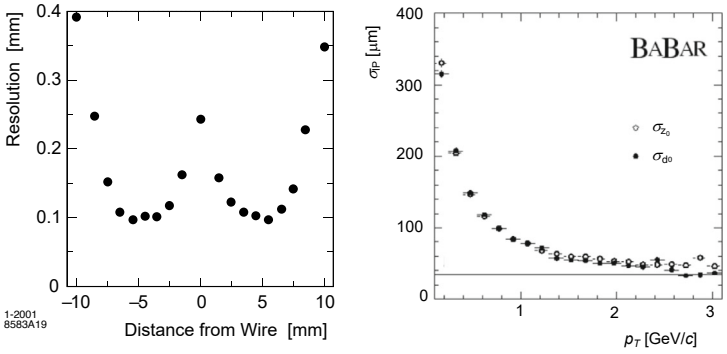

Fig. 4.30 Left: Position resolution as a function of drift distance in the *BABAR* drift chamber cell [77]. Right: Impact parameter resolution in σ_{d_0} (solid points) and σ_{z_0} (open circles) as a function of transverse momentum in the *BABAR* experiment. Both reprinted with kind permission from [77], © 2002, Elsevier. All rights reserved

impact parameter (z_0), azimuth angle (ϕ_0), tangent of the dip angle ($\tan\lambda_d$) and curvature (κ_t) from the measured fits. We will define the impact parameters in Sect. 5.2.2.

Figure 4.30 (right) shows the transverse and longitudinal impact parameter resolutions d_0 and z_0 for tracks in multi-hadron events as a function of the transverse momentum. Both have a rather similar dependence. For $p_T = 0.4$ GeV/c, the longitudinal and transverse impact parameter resolutions are both 200 μm approaching 30 μm at high momenta. For each hit on a track, we also measure the ionization. We perform pedestal subtraction, correct for gain variations and integrate the signal

over a period of approximately 1.8 μs. The ionization measurements are used for particle identification discussed in Chap. 9. The $\mathrm{d}E/\mathrm{d}x$ resolution is 6.9%.

4.3.5 Drift Chamber Alignment

The construction of drift chambers is performed with great care keeping tight tolerance with positioning the wires on the endplates. Typically, the holes are drilled with an accuracy to better than 50 μm. Cosmic muon data are used to perform alignments. The procedure is discussed in detail in [80]. Here, we give a brief summary. The data are taken without the magnetic field and with the magnetic field turned on. Misaligned sense wire positions affect the spatial resolution. We can classify the misalignment of sense wire positions into three categories:

- Misalignment between layers of the drift chamber. This is described by shifts in the three coordinates, δx, δy and δz and a rotation around the z axis, $\delta\phi$.
- A chamber twist, i.e. a rotation of the forward endplate with respect to the backward endplate. The correction depends on the dip angle λ_d.
- Misalignment between the sense wires within a layer. Here, the corrections involve shifts in the x and y directions.

A drift chamber misalignment changes the time-to-distance relation

$$\Delta X(z) = X_{\text{true}}(z) - X_{\text{fit}}(z), \tag{4.35}$$

where $X_{\text{true}}(z)$ and $X_{\text{fit}}(z)$ are the true and fitted time-to-distance relations, respectively. Both depend on the drift distance z. From layer-by-layer misalignments we obtain

$$\Delta X(z) = -r_l \sin\delta\phi + \delta x(z)\sin\phi - \delta y(z)\cos\phi, \tag{4.36}$$

where r_l is the radius of the layer. The first term describes the effect of a rotation $\delta\phi$ while the second and third terms describe the effects of the δx and δy shifts, respectively. The δz shift affects the drift chamber performance for the stereo wires only and its effect is proportional to the sine of the stereo angle. Since the drift chamber has no external reference point, an appropriate internal reference point needs to be chosen for the first iteration. To avoid the effect of twist misalignments, we select vertical muons ($70^\circ < \theta < 110^\circ$). We fit the track with respect to the reference points and extrapolate it to the layers that we want to align. For these we calculate the residual $\Delta X(z)$. We perform this procedure step-by-step for each superlayer. The aligned layers are added to the reference. We use them for track fitting to align the next superlayer. We start with the inner layer moving out. Since alignments are different at the forward and backward planes, we perform the procedure at different z positions. Figure 4.31 (left) shows an example of the $\Delta X(z)$ dependence on z for the alignment of the Belle II drift chamber [80]. The residual shows a linear z dependence. We depict the ϕ dependence in Fig. 4.31 (right), which shows a sinusoidal ϕ dependence.

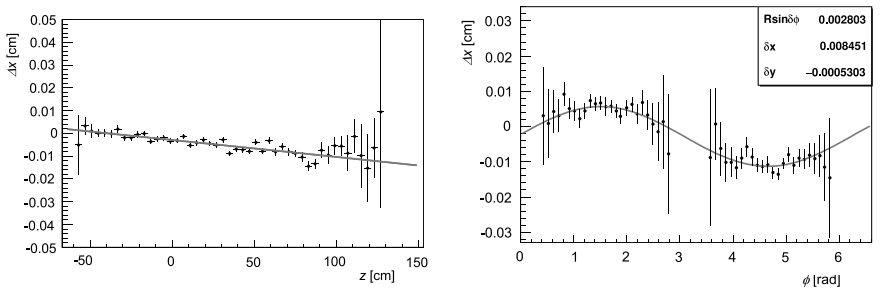

Fig. 4.31 Left: Example of the z dependence of the residual $\Delta X(z)$ in layer 38 determined in the alignment of the Belle II drift chamber. Right: Example of the ϕ dependence of the residual $\Delta X(z)$ in layer 38 determined in the alignment of the Belle II drift chamber. Both reprinted with kind permission from [80], © 2019, Elsevier. All rights reserved

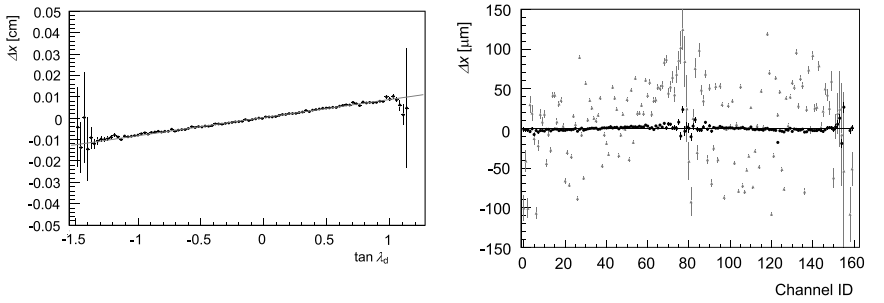

Fig. 4.32 Left: Example of the $\tan\lambda_d$ dependence of the residual $\Delta X(z)$ in layer 55 determined in the alignment of the Belle II drift chamber. Right: Residual distribution $\Delta X(z)$ as a function of the channel number in layer 12 showing data before alignment (triangles) and aligned data (points). Both reprinted with kind permission from [80], © 2019, Elsevier. All rights reserved

The twist misalignment is proportional to $\tan\lambda_d$ of the track,

$$\Delta X(z) = \tan\lambda_d \frac{r_l}{\ell_{\mathrm{dc}}}(r_l - r_0)\sin\delta\phi + p_0, \tag{4.37}$$

where r_0 is the radius of the layer of reference, ℓ_{dc} is the length of the layer and p_0 is constant. We fit a cosmic muon track using the four innermost super-layers and extrapolate it to the outer layers. Figure 4.32 (left) shows the residual $\Delta X(z)$ as a function of $\tan\lambda_d$. The residual increases linearly from $-100\ \mu$m at $\tan\lambda_d = -1.5$ to $100\ \mu$m at $\tan\lambda_d = 1.5$. The final twist angle is $+0.295 \pm 0.001$ mrad.

For the wire-to-wire alignment of sense wires in the ϕ-direction we use small-angle muons. Since we do not have sufficient data available for the incident angle around 90° we cannot perform alignments in the r direction. This can be done with beam data. We determine the residual at the endplate using a similar procedure as that for the layer-to-layer alignment and convert them into δx and δy shifts,

$$\begin{aligned} \delta x &= -\Delta X(z)\sin\phi, \\ \delta y &= -\Delta X(z)\cos\phi. \end{aligned} \tag{4.38}$$

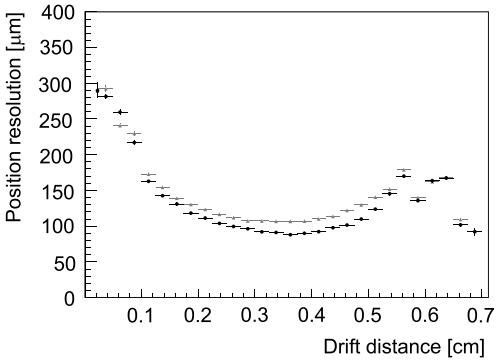

Fig. 4.33 Left: Position resolution as a function of the drift distance in layer 12 of the Belle II drift chamber for muon tracks with small incident angles ($|\alpha_{\rm tr}| < 5°$) and polar angles of $120° < \theta < 150°$ for non-aligned wires (grey points) and aligned wires (black points). Reprinted with kind permission from [80], © 2019, Elsevier. All rights reserved

Figure 4.32 (right) shows the residual $\Delta X(z)$ as a function of the wire channel number. After aligning the wires, the residual distributions are close to zero. The wire-by-wire misalignment is smaller than 50 μm for most of the layers as expected from the hole position survey. Figure 4.33 shows the position resolution as a function of the drift distance. For drift distances of 1–6 mm, the position resolution after alignment is improved significantly. Between 0.3 mm and 0.4 mm drift distance the spatial resolution is 90 μm.

4.4 Jet Drift Chambers

In a jet drift chamber, the number of measured points along a radial track is considerably increased to about one measurement/cm. All signal wires run in the axial direction forming a middle plane of a sector-shaped cell in which the transverse $\vec{E}$ field points into the ϕ direction. The sense wires are closely spaced and are interleaved with potential wires. The drift paths of the electrons in the gas are much longer than those in cylindrical drift chambers. The first jet chamber was reconstructed for the JADE detector [90]. The Mark II [91], H1 [92] and the OPAL experiments also used jet chambers [93,94]. As examples we discuss the JADE and OPAL jet chambers below and summarize properties of all four chambers in Table 4.4. Jet chambers achieve very good spatial resolutions in $r\phi$ of $130 - -170$ μm and a two-track separation of a few mm. Due to the large number of measurements, they also measure ionization losses rather well.

Figure 4.34 (left) shows the layout of two sector-shaped segments of the JADE jet chamber [90], which operated at the PETRA e^+e^- storage ring to search for the top quark. The jet chamber had an inner radius of $r_i = 21$ cm, an outer radius of $r_o = 78$ cm and a length of $\ell_{\rm ch} = 2.4$ m. The cylindrical volume was subdivided into 24 radial segments, each with a 15° opening angle. Each radial segment had 48 signal wires parallel to the magnetic field along the z direction arranged into

Table 4.4 Comparison of Jet Drift Chambers showing the inner radius r_i, outer radius r_o, chamber length $\ell_{\rm ch}$, number of sense wires N_{sw}, number of sense wires per cell, sense wire material, diameter of the sense wire d_w, sense wire spacing s_w, maximum number of measurements $N_{\rm max}$, field wire material, diameter of the field wire, maximum drift distance $\ell_{\rm drift}$, method of z measurement, gas mixture, gas fraction, electric-field strength $|\vec{E}|$, magnetic-field strength $|\vec{B}|$, drift velocity $v_{\rm d}^e$, Lorentz angle α_L, spatial resolution range in $r\phi$, average spatial resolution in $r\phi$, spatial resolution in z, two-track resolution $\Delta_{2-\rm tr}$, $\mathrm{d}E/\mathrm{d}x$ resolution for minimum-ionizing particles, and transverse momentum resolution $\sigma_{p_{\rm T}}/p_{\rm T}^2$. †The drift cells are rotated by the expected Lorentz angle of 30°; the drift cells are arranged into an inner and an outer jet chamber. ‡Tracks are constrained to originate from a single point. #This gas was used for standard e-p running; for other periods the gas mixture was Ar-CO_2-CH_4 (89.5:9.5:1). §A range indicates measured resolutions in a cell; a single value indicates the average resolution over the cell. §§They use a special chamber to get a more precise rz measurement than from charge division. ⋆The latter value is for the end field wires

Experiment	JADE	Mark II	OPAL	H1†
Reference	[90,95]	[91,96]	[93,94,97]	[63,92]
r_i [cm]	2	19.2	25	20.4/45.2
r_o [cm]	80	151.9	185	53/84.4
$\ell_{\rm ch}$ [cm]	240	230	320–400	220
$\mathrm{N_{sw}}$	1,536	5,832	3,816	2,640
$\mathrm{N_{sw}}$/cell	16	6	159	24/32
Sense wire	W-Re-Au	W-Au	W-Re-Au	W-Re-Au
d_w [μm]	20	30	25	20/20
s_w [mm]	10	8.33	10	5.1/5.1
$N_{\rm max}$	48	72	159	24/32
Field wire	Cu-Be	Cu-Be	Cu-Be	Cu-Be
d_{fw} [μm]	100	178/304⋆	125	90/90
$\ell_{\rm drift}$ [cm]	2.6–7.8	3.3	3–25	$^{2.29-4.45}/_{2.85-4.31}$
$z_{\rm meas}$	Q div.	Stereo	Spec. cham.	Q-div.
Gas mixture	Ar-CH_4-iC_4H_{10}	Ar-CH_4-$-CO_2$	Ar-CH_4-iC_4H_{10}#	Ar-C_2H_6
Fraction [%]	(88.7:8.5:2.8)	(89:1:10)	(88.2:9.8:2)	(50:50)
$\vert\vec{E}\vert$ field [$\frac{\rm kV}{\rm cm}$]	0.94	0.9	0.94	1.0
$\vert\vec{B}\vert$ field [T]	0.45	0.45	0.435	1.15
$v_{\rm d}^e$ [$\frac{\rm cm}{\mu\rm s}$]	5.04	5.2	5.29	5.0
α_L	18.5°	17.8°	20°	30°
$\sigma_{r\phi}$ [μm]§	140–185	120–200	100–180	
$\langle\sigma_{r\phi}\rangle$ [μm]§	160	170	135	170
σ_{rz} [mm]	26	0.12–0.20	$1\% \cdot \ell^{\S\S}_{wire}$	$1\% \cdot \ell^{\S\S}_{wire}$
$\Delta_{2-\rm tr}$[mm]	7	3.8	2	2
$\frac{\sigma_{\mathrm{d}E/\mathrm{d}x}}{\mathrm{d}E/\mathrm{d}x}$ [%]	8.1	6.9	3.1	10
$\frac{\sigma p_{\rm T}}{p_{\rm T}^2}\,\mathrm{GeV}/c^{-1}$	0.022	0.0046 (0.0031)‡	0.0015	0.01

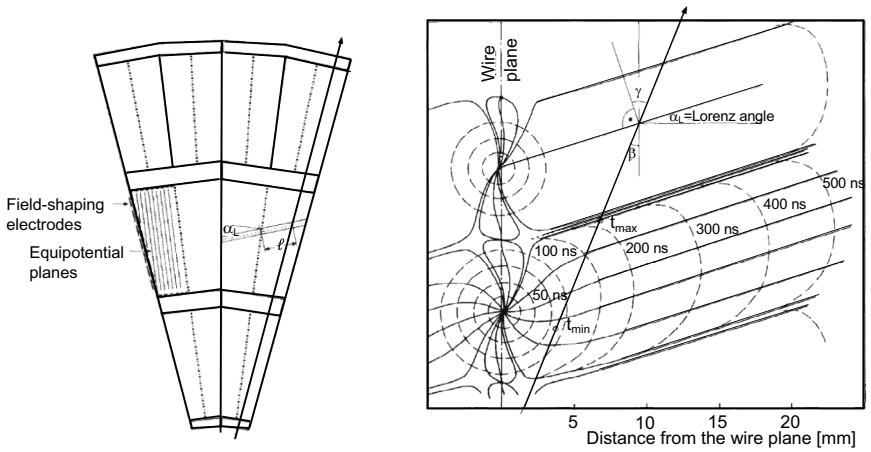

Fig. 4.34 Left: Cross section through two segments of the JADE jet chamber. The field-shaping electrodes are shown on the left-hand edge of the cell in the center partition. Both, equipotential lines and the Lorentz angle are indicated. Right: Drift trajectories (solid lines) and isochrones (dashed curves) of the JADE jet chamber. Both reprinted with kind permission from [90], © 1980, Elsevier. All rights reserved

three radial partitions. One partition had 16 sense wires in the center, which were staggered to break the left-right symmetry. So, a total of 48 measurements were performed over a 57 cm length. On the boundaries of each radial sector, field-shaping electrodes were positioned. Figure 4.34 (right) shows the isochrones and electron drift directions, which have complicated shapes near the signal wire. The jet chamber was operated with an argon-methane-isobutane gas mixture (88.7:8.5:2.8) at a pressure of 4 atmospheres. The electric-field strength was 0.94 kV/cm yielding a drift velocity of $v_{\rm d}^e = 5.04$ cm/μs. Let us recall that the Lorentz angle is given by $\tan\alpha_L = \omega_B \tau_e \sim k(|\vec{E}|) \cdot v_{\rm d}^e \cdot |\vec{B}|/|\vec{E}|$, where $k(|\vec{E}|)$ is a factor that depends on the gas mixture and the $\vec{E}$ field. The Jade experiments operated in a magnetic field of $|\vec{B}| = 0.45$ T, yielding a large Lorentz angle of $\alpha_L = 18.5°$ as shown in Fig. 4.34 (left).

Jet chambers yield good spatial resolutions. Figure 4.35 (left) shows the position resolution of the JADE jet chamber in the $r\phi$ plane as a function of drift length. Near the sense wire the position resolution was $\sigma_{r\phi} = 140\,\mu$m increasing linearly with drift distance to $\sigma_{r\phi} \simeq 180\ \mu$m at 6 cm, where the contribution from the electronic noise was 110 μm. The z position was obtained via charge division yielding a resolution of $\sigma_z = 16$ mm. Using 48 space points provided a momentum resolution of $\sigma_{p_{\rm T}}/p_{\rm T}^2 = 3.3\%\ ({\rm GeV/c})^{-1}$. Figure 4.35 (right) shows an axial projection of an e^+e^- collision at a center-of-mass energy of 30 GeV in the JADE jet chamber. Since the hits are closely spaced track segments are clearly visible without a fit curve. All charged tracks are well resolved.

The OPAL jet chamber was the largest providing the most measurements and achieving a reasonable spatial resolution. Figure 4.36 (left) shows a schematic view of part of one sector. The jet chamber had an inner radius of $r_i = 0.25$ m, an outer

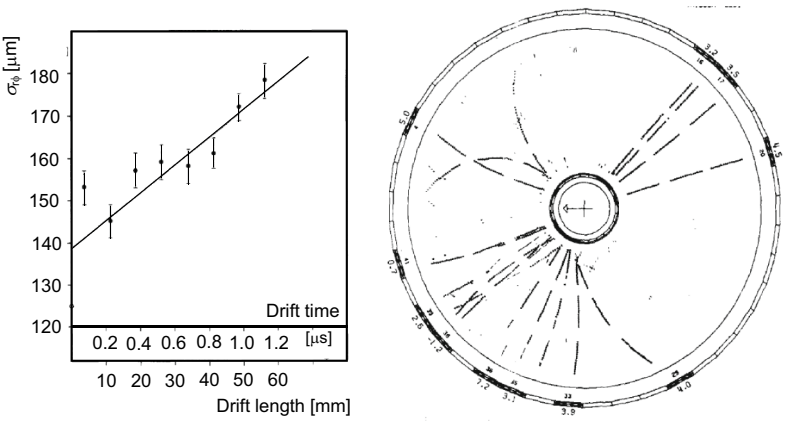

Fig. 4.35 Left: Mean position resolution of single-cell track fits in the $r\phi$-plane as function of the mean drift distance for the Jade jet chamber. Right: The axial projection of the collision process $e^+e^- \rightarrow hadrons$ in the Jade detector. The 16-hit measurements in each of the three partitions appear as three line segments. Both reprinted with kind permission from [90], © 1980, Elsevier. All rights reserved

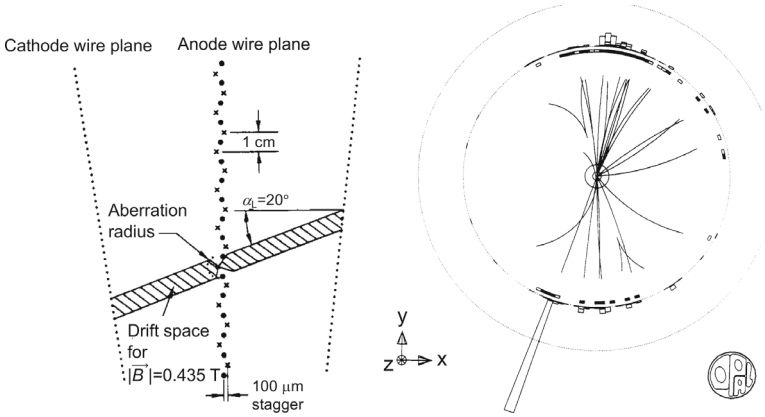

Fig. 4.36 Left: Schematic view of a part of one sector of the 24-sector OPAL jet chamber displaying the staggered sense wires (crosses) and potential wires (points) [94]. Furthermore, the drift space and Lorentz angles are shown. Right: A hadronic Z^0-decay. The lower jet contains a high-energy electron indicated by the straight track pointing to a high-energy shower in the electromagnetic calorimeter on the bottom. Note that the hits on the closely spaced wires already define the trajectories without a fit. The jet chamber only shows hits that belong to charged particles coming from the Z^0 decay. Both reprinted with kind permission from [94], © 1992, Elsevier. All rights reserved

radius of $r_a = 1.85$ m and a length of $\ell_{\rm ch} = 4$ m. It was segmented into 24 identical sectors each having 159 gold-plated tungsten-rhenium sense wires 25 μm in diameter equally spaced at 10 mm, which were kept at ground potential. The sense wires were interleaved with potential wires that were operated at a high voltage of –2.38 kV. At each end a 175 μm thick wire terminated the anode plane. The sense wires were staggered at 100 μm to break the left-right symmetry. Cathode wire planes formed boundaries between adjacent sectors. The cathodes consisted of copper-beryllium wires 125 μm in diameter spaced at 3.1 mm. The first wire in each plane had a diameter of 175 μm. The cathode planes were inclined by 7.5° with respect to the anode planes. Since the equipotential lines in the drift region are parallel to the anode plane, each wire of the cathode plane sat at a different potential. The voltages ranged from –25 kV at the outer radius to –5 kV at the inner radius. Figure 4.36 (right) shows an event display of a hadronic Z^0 decay. The charged tracks in each jet are clearly separated. Besides the hits of the charged tracks from the Z^0 decay, no extra hits are visible.

The chamber was operated with a gas mixture of Ar-CH_4-iC_4H_{10} (88.2:9.8:2.0) in a magnetic field of 0.435 T. Electrons produced in an ionization process drifted with a drift velocity of 5.3 cm/μs in an electric field of 0.94 kV/cm under a Lorentz angle of $\alpha_L = 20°$. The maximum drift distance was 25 cm. Excluding bad channels, which were as low as 0.3%, a single-hit efficiency of >99.2% was measured by studying $Z^0 \to \mu^+\mu^-$ decays [94]. Figure 4.37 (left) shows the $r\phi$ position resolution as a function of drift distance. Close to the wire, a position resolution of $\sigma_{r\phi} = 100$ μm was achieved, while at 20 cm drift length the resolution increased to $\sigma_{r\phi} = 135$ μm. The z position was determined by charge division with a resolution of $\sigma_z = 4.5$ cm for di-muon events and 6 cm for hadron events. The transverse momentum resolution was $\sigma_{p_{\rm T}}/p_{\rm T} = 0.0015 \cdot p_{\rm T} \oplus 0.02$. Figure 4.37 (right) shows the position resolution in the $r\phi$ plane as a function of the local track angle with respect to the anode plane. For larger angles the position resolution became significantly worse. The anode wires also recorded the ionization loss. The $\mathrm{d}E/\mathrm{d}x$ resolution was 3.1% providing good K-π separation at low momenta (see Chap. 9).

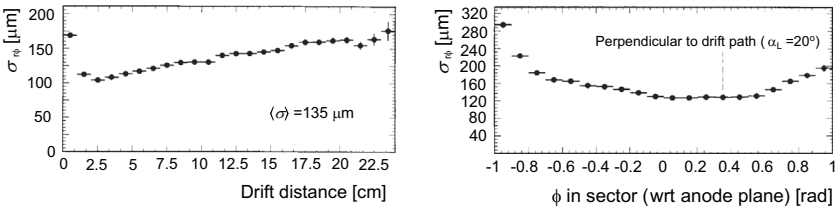

Fig. 4.37 Left: Position resolution as a function of the drift distance in the OPAL jet chamber. The average resolution is $\sigma = 135$ μm. Right: Position resolution as a function of the local track angle with respect to the anode wire plane. Both reprinted with kind permission from [94], © 1992, Elsevier. All rights reserved

4.4.1 Small Jet Drift Chambers

Before the development of solid state detectors small jet drift chambers were built to measure tracks more precisely close to the beam. For example, the Mark II experiment built a vertex jet drift chamber [98]. The chamber extended from 5.0 cm to 17.0 cm in the radial direction and 55 cm in the axial direction. It was divided into ten axial drift cells. To break the left-right symmetry individual cells were tilted with respect to the radial direction. There were 40 anode wires 20 μm in diameter spaced at 2.9 mm of which 38 were read out. They were interleaved with 40 potential wires 225 μm in diameter. The sense wire planes were sandwiched between two grid planes spaced at 1.8 mm and consisting of 150 μm diameter wires. The cell was closed with 59 cathode wires 225 μm in diameter spaced at 2.0 mm on each side of the sector. Extra electrodes at the innermost and outermost radii reduced edge effects. The chamber operated with a CO_2-C_2H_6 (92:8) gas mixture. Voltages on the cathode planes were graded between –3.5 kV and –11.7 kV. The sense wires were operated with +2.94 kV while the potential wires were grounded and the grid wires were held at –0.47 kV. The chamber operated in a 0.475 T magnetic field. The spatial resolution varied with the drift distance between 25 μm and 80 μm yielding an average of 50 μm. Properties and parameters of other small jet drift chambers are summarized in Table 11.3 in [87]. In small drift chambers that have been used as vertex chambers, the typical spatial resolutions were 40–55 μm [87]. In the mini-jet vertex chamber prototype a spatial resolution of 20–25 μm was achieved with a slow gas CO_2-isobutane (80:20) at a pressure of 2.5 bar [99]. These resolutions are rather large with respect to those reached in silicon detectors we discuss in Chap. 6.

4.5 Time Projection Chambers

The time projection chamber (TPC) combines the principles of a drift chamber with that of a proportional chamber. It was proposed first by Nygren for the TPC detector at PEP4 [100,101]. The new idea consisted of making a direct three-dimensional position measurement.

4.5.1 Conceptual TPC Design

Figure 4.38 (left) shows a schematic view of the TPC built by Nygren [100]. A large cylindrical volume ($r = 1$ m, $\ell_{ch} = 2$ m) is filled with an Ar-CH_4 (80:20) gas mixture at a pressure of 8.5 bar. The cylinder is split into two half cylinders that are separated by the high voltage electrode. Field-defining electrodes are placed on the outer shell and the inner cylinder. The potential is defined by a voltage divider. Both endcaps of the barrel are equipped with one layer of MWPCs,[11] each subdivided

[11] In newer TPCs, the MWPCs are replaced with GEM detectors or Micromegas.

into six sectors. Each sector has 183 proportional signal wires for multiple ionization measurements along the $r\phi$ projection of the track. In addition, the cathode plane below the anode is segmented with pads that are read out. The size in the radial direction covers 15 anode wires. On each half cylinder, a high electric field is placed parallel to the beam axis pointing towards the center so electrons can drift towards the endcaps. A high magnetic field (1.5 T) lies parallel to the electric field so that the electrons are not exposed to any Lorentz force and $\vec{v}_{\mathrm{d}}^{\,e}$ is parallel to $\vec{E}$. Since drift lengths are much longer than those in drift or jet chambers, the electric field has to be kept precisely uniform over the entire length requiring strict mechanical tolerances and precise manufacturing of field-defining electrodes on the outer shell and inner cylinder. The image of the electron cloud is broadened by diffusion during the drift process. The broadening is considerably reduced by the strong $|\vec{B}|$ field. The electrons move along a helical path around the magnetic-field lines. The transverse diffusion coefficient is reduced by $1/(1+\omega_B^2\tau_e^2)$.

Figure 4.38 (right) illustrates the layout of the endcaps. The anode plane is sandwiched between a cathode plane above and a pad-segmented cathode plane below that is also read out. In addition, a gating plane is placed above the upper cathode plane. When a trigger is accepted the gating plane is opened so the electrons can drift towards the anode. Once the electrons start to avalanche near the anode wires the gating plane is closed to prevent the positive ions to move back into the drift region. This is achieved by applying a positive high voltage to the gating plane. Signals recorded on the wires yield measurements of r while signals induced on the pads provide ϕ measurements. Note that the main contribution comes from the positive ions. The z position is obtained from the drift time the electrons need for traveling

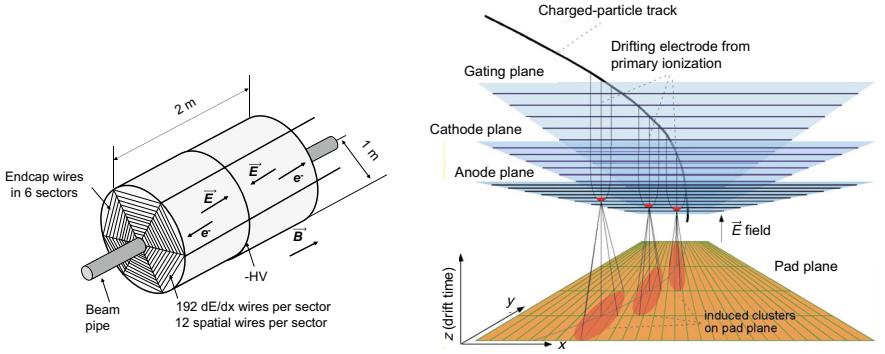

Fig. 4.38 Left: Schematic view of the time projection chamber built by Nygren. The cylindrical volume is segmented into two halves. The electric field in each half points to the center. The magnetic field is parallel or antiparallel to the electric field. Each endcap is segmented into six sectors equipped with one layer of multi-wire proportional chambers. Right: Schematic layout of the endcaps. The electrons produced by primary ionization of a traversing charged particle drift through a gating plane and a cathode plane towards the anode, where they are collected. The clusters on the anode wires induce charge clusters on a cathode pad plane located below the anode. Once the electrons have passed the gating plane it will be switched on to prevent the ions to drift back into the drift volume. Reprinted with kind permission from [102], © 2013, P. Christiansen. All rights reserved

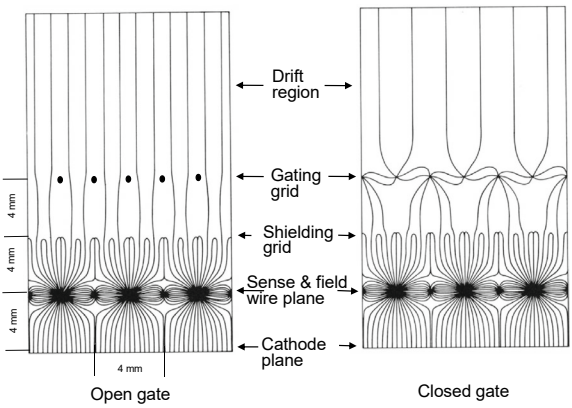

Fig. 4.39 The electric-field configuration for open (left) and closed gates (right). Reprinted with kind permission from [103], © 1985, Elsevier. All rights reserved

from the primary ionization point to the anode wires of the MWPCs. Figure 4.39 shows the electric-field configuration for open (left) and closed gates (right). In the open-gate configuration the electrons can move towards the anode. In the closed-gate configuration the ions are blocked from moving into the drift region.

At high event rates, field distortions will occur, which come from the space charge of positive ions formed in avalanches near the signal wires. The ion density is given by

$$\rho_{ion} = \frac{1}{\ell_w} \frac{f_{ion}}{\mu_{ion}} \frac{A_\gamma}{|\vec{E}|} \frac{N_e}{s_w}, \tag{4.39}$$

where f_{ion} is the fraction of ions migrating back to the drift region, A_γ is the gas amplification at the anode, N_e is the number of electrons reaching the anode wire per unit time, ℓ_w is the wire length, μ_{ion} is ion mobility, $|\vec{E}|$ is the drift field strength and s_w is the wire pitch. The closed-gate configuration reduces the ion density considerately.

Like cylindrical drift chambers, TPCs have been used in various experiments, for example in TOPAZ [104–106], ALEPH [35,107–109], DELPHI [36] and ALICE [110]. Properties of these TPCs and the PEP4 TPC are summarized in Table 4.5. Except for ALICE, all TPCs use an argon–methane gas mixture. The $r\phi$ position is measured by wires and pads in the endplate detectors while the z position is determined by the drift time. The drift velocities are all rather high. The PEP4 TPC, the smallest with a 1 m drift length, achieved the best spatial resolutions in $r\phi$ and rz. The ALICE TPC whose schematic layout is depicted in Fig. 4.40 is the largest with a drift length of 2.5 m. It has the poorest resolution in $r\phi$ and a rather poor resolution in rz. The ALEPH TPC with the second best rz spatial resolution achieved the best momentum resolution. We present some more details of the ALEPH and ALICE TPCs below. Before, we would like to mention two other types of TPCs. In searches for weakly-interacting massive particles the XENONnT [111] and LZ [112] experiments use a liquid xenon TPC, which is operated in dual phase. We discuss the principle in Sect. 7.2.5.2. The long-baseline neutrino experiment Dune will use a liquid argon TPC, both in the near and far detectors [113].

Table 4.5 Examples of time projection chambers used in high-energy physics experiments showing outer and inner radii (r_o, r_i), drift length ℓ_{drift}, number of sense wires N_{sense}, sense wire spacing s_w, number of pads N_{pad}, pad dimension, maximum number of pad measurements $N_{\text{max}}^{\text{pad}}$, maximum number of sense wire measurements $N_{\text{max}}^{\text{wire}}$, gas mixture, gas fractions, gas pressure, gas amplification, electric-field strength $|\vec{E}|$, magnetic-field strength $|\vec{B}|$, drift velocity v_{d}^{e}, factor $\omega_B \tau_e$, average spacial resolution in $r\phi$ from pads, spacial resolution in rz, two-track resolution in $r\phi$, relative transverse momentum resolution from the TPC alone, relative transverse momentum resolution from all trackers and $\text{d}E/\text{d}x$ resolution. More examples are listed in [116]. †This included the DELPHI inner detector (ID) and outer detector (OD)

Experiment	PEP4	TOPAZ	ALEPH	DELPHI	ALICE
Reference	[100,107]	[104–107]	[35,107–109]	[36,107]	[110]
r_o [cm]	100	127	180	116	278
r_i [cm]	20	30	31	32	61
ℓ_{drift} [cm]	2 × 100	2 × 122	2 × 220	2 × 134	2 × 249.7
N_{sense}	2,196	2,816	6,336	1,152	No readout
s_w [mm]	4	4	4	4	2.5
N_{pad}	13,824	8,192	41,004	20,160	557,568
Pad $r \times r\phi$ [mm × mm]	7.0 × 7.5	12×9.1–10.7	30 × 6	8 × 7.	4 × 7.5 6 × 10(15)
$N_{\text{max}}^{\text{pad}}$	15	10	21	16	32 & 64
$N_{\text{max}}^{\text{wire}}$	183	175	338	192	–
Gas mixture	Ar-CH_4	Ar-CH_4	Ar-CH_4	Ar-CH_4	Ne-CO_2-N_2
Fractions	(80:20)	(90:10)	(90:10)	(80:20)	(85.7:9.5:4.8)
Pressure [bar]	8.5	3.5	1	1	1
Amplification	1,000		3,000–5,000	5,000	7,000–8,000
$\lvert\vec{E}\rvert$ [kV/cm]	0.55	0.353	0.125	0.15	0.4
$\lvert\vec{B}\rvert$ [T]	1.32	1.0	1.5	1.2	0.5
v_{d}^{e} [cm/μs]	5.0	5.3	5.24	6.7	2.65
$\omega_B \tau_e$	1.5	4.9	8.9	5.2	0.32
$\langle\sigma_{r\phi}\rangle$(pads) [$\mu$m]	150	185	173	180	1,100/800
σ_z [mm]	0.160	0.335	0.5	0.9	1.25/1.1
$\sigma_{2-\text{track}}$ [mm]	24	25	15	15	–
$\frac{\sigma p_{\text{T}}^{\text{TPC}}}{p_{\text{T}}^2}$ $[\frac{\text{GeV}}{c}]^{-1}$	0.009	0.01	0.0012	–	0.002
$\frac{\sigma p_{\text{T}}^{\text{all}}}{p_{\text{T}}^2}$ $[\frac{\text{GeV}}{c}]^{-1}$	0.0065	–	0.0008	0.0015	–
$\frac{\sigma_{\text{d}E/\text{d}x}}{\text{d}E/\text{d}x}$ [%]	2.7	4.6	4.5	5.7	5.0

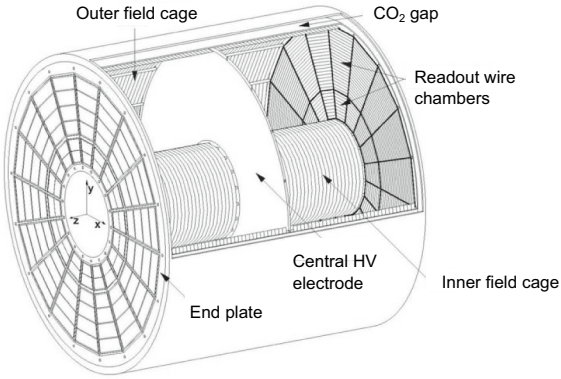

Fig. 4.40 Schematic view of the ALICE time projection chamber. The outer radius is 2.47 m and the inner radius is 0.85 m. The TPC has a 5.1 m length. Each endcap is segmented into 2×18 sectors. The electric-field strength is 400 V/cm. Reprinted with kind permission from [110], © 2010, Elsevier. All rights reserved

4.5.2 The ALEPH and ALICE Time Projection Chambers

The ALEPH experiment used a TPC as the main tracking detector, which consisted of a 2×2.2 m long segmented cylinder with circular endplates having an outer radius of 1.7 m and an inner radius of 0.33 m. The two halves were separated by a graphite-coated mylar membrane of 25 μm thickness. The endplates were segmented into 18 wire chamber sectors, six identical inner sectors plus 12 outer sectors coming in two shapes. The endplates contained 20,502 pads and 3,168 sense wires. The TPC was operated with an Ar-CH_4 (91:9) gas mixture at atmospheric pressure in a magnetic field of 1.5 T. The electric field was 125 V/cm, yielding a drift velocity of $v_{\mathrm{d}}^{e} = 5.24\,\mathrm{cm}/\mu\mathrm{s}$. The misalignment between $\vec{E}$ and $\vec{B}$ fields was found to be 0.03°. The factor affecting the transverse diffusions was $\omega_B \tau_e = 8.9 \pm 0.3$. Figure 4.41 (left) shows the ALEPH TPC from the inside. The endplate wire chamber sectors are well visible. The TPC performed very well. The spatial resolution in $r\phi$ was 173 μm while that in rz was 740 μm for tracks with polar angles $80° < \theta < 100°$. The energy loss was measured in each sense wire. With a 4 mm pitch this gave a total of 338 possible $\mathrm{d}E/\mathrm{d}x$ measurements per track.

At the LHC, the ALICE experiment uses a TPC as central tracker, which is 5.1 m long (2×2.55 m) and has an inner (outer) radius of 0.845 m (2.466 m) (see Fig. 4.40). It operates with a Ne-CO_2-N_2 (85.7:9.5:4.8) gas mixture in a magnetic field of 0.5 T. The electric field is 400 V/cm yielding a drift velocity of $v_{\mathrm{d}}^{e} = 2.65\,\mathrm{cm}/\mu\mathrm{s}$, which is about a factor of two smaller than that in the ALPEH TPC. Each of the two endcaps is instrumented with 81 inner and 18 outer trapezoidal MWPCs containing a total of 557,568 pads that determine the $r\phi$ position. Figure 4.41 (right) shows a photograph of the field cage of the ALICE TPC. The MWPCs have four planes: the gating grid, cathode wire, anode wire and cathode pad planes that are separated by 3 mm each. While the gating grid has a wire spacing of 1.25 mm, the wires in the cathode and anode wire planes are separated by 2.5 mm. The sense wires are gold-plated tungsten wires 20 μm in diameter. All other wires are copper-beryllium wires 75 μ in diameter. For the inner chamber pad sizes are 4 mm $\times$ 7.5 mm while for the outer chambers two pad sizes are used, 6 mm $\times$ 10 mm and 6 mm $\times$ 15 mm for radii below and

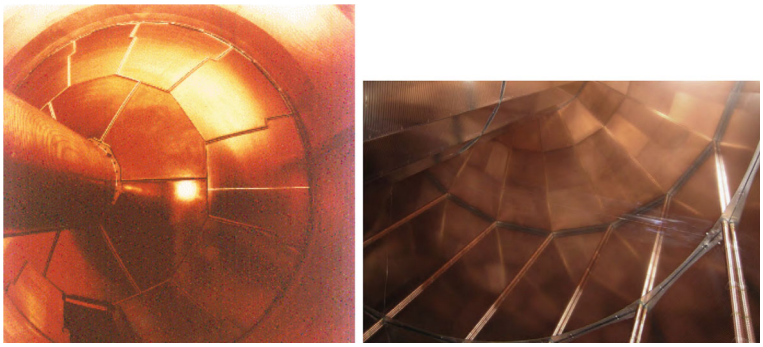

Fig. 4.41 Left: View of the inner side of the endcap in the ALEPH TPC showing the 18 sectors of the endplate [114]. Reprinted with kind permission from [114], © 1989, the ALEPH Collaboration. All rights reserved. Right: Field cage of the ALICE TPC. The trapezoidal sectors with the MWPCs are visible. Reprinted with kind permission from [110], © 2010, Elsevier. All rights reserved

above 1.99 m, respectively. Since $\omega_B \tau_e = 0.32$ the transverse diffusion is not much reduced by the magnetic field. The inactive material amounts to less than $3\% \cdot X_0$. For run 3 the MWPC readout will be replaced by four-GEM stacks [115].

4.5.3 Calibration and Monitoring

A system of UV lasers is used to calibrate the TPC, monitor its performance and measure distortions as well. For example in the ALEPH TPC, the laser calibration system allowed the generation of five laser beams on both sides of the TPC at three different azimuthal angles. This provided 30 straight ionization tracks that seemed to originate from the center of the TPC. It was used to measure and correct residual inhomogeneities of the electric and magnetic fields, which produce systematic displacements of reconstructed coordinates. It also served to measure the modulus of the drift velocity of electrons in the TPC gas.

In the ALICE TPC, each half has six rods, which are equipped with four micromirror bundles of which each contains seven small mirrors. The light of one laser in each half is split and guided into the six rods. The two lasers are synchronized to provide simultaneous laser pulses in the entire TPC yielding a total of 336 simultaneous narrow laser rays. The lasers are equipped with two frequency doublers producing UV light of 266 nm wavelength. The laser system runs every 30 min interspersed between physics events to measure the drift velocity and assess space charge effects.

4.5.4 Performance

The spatial reconstruction of ionizing tracks is performed by measuring two-dimensional projected images in the $r\phi$ plane on endcaps typically using the signal-induced charge on the cathode pads. The positions are determined using the center-

of-gravity method. The z coordinate is obtained by measuring the arrival time of the primary electrons. So, with the $r\phi$ information from the MWPCs we get three-dimensional track segments. Thus, pattern recognition and track finding are considerably alleviated compared to chambers that have uncorrelated coordinate information as in drift chambers. In the PEP4 TPC, the spatial resolution in $r\phi$ with pad readout was $\sigma_{r\phi} = 100\ \mu$m while the spatial resolution in z obtained from the drift distance was $\sigma_z = 300\ \mu$m. The resolution of the COG cluster can be parameterized in the following way,

$$\sigma^2_{\mathrm{COG}} = \sigma^2_0 + p^2_{\mathrm{L}}\ell_{\mathrm{drift}} + p_{\mathrm{A}}\tan^2\alpha_{\mathrm{tr}}, \tag{4.40}$$

where σ_0 is the resolution for zero drift length ℓ_{drift} and zero crossing angle α_{tr}. The parameters p_{L}, p_{A} and σ_0 are typically obtained from a fit. Note that p_{L} increases with gas gain fluctuation as $\sqrt{A_{\mathrm{gas}}}$ and the diffusion resolution σ_D and decreases with the pad length as $1/\sqrt{\ell_{\mathrm{pad}}}$ while p_{A} increases with $\sqrt{\ell_{\mathrm{pad}}}$ and the landau fluctuation of the ionization energy loss factor as $\sqrt{W_{\mathrm{landau}}}$.

Figure 4.42 shows the spatial resolutions in $r\phi$ (left) and in rz (right) measured by the ALEPH TPC in $Z^0 \to \ell^+\ell^-$ events. The best spatial resolution in $r\phi$ was achieved for tracks with zero pad crossing angle yielding $\sigma_{r\phi} = 173\ \mu$m. In the z direction the best spatial resolution of $\sigma_z = 0.74$ mm was obtained for a dip angle of zero degrees. Larger pad crossing angles and dip angles worsen the spatial resolution as Fig. 4.43 (left, right) illustrate.

Figure 4.44 shows the measured spatial resolutions in $r\phi$ (left) and in rz (right) as a function of the drift distance for the ALICE experiment. For 250 cm drift distance and small inclination angles, the spatial resolutions are $\sigma_{r\phi} = 800 \pm 80\ \mu$m and $\sigma_z = 900 \pm 100\ \mu$m. For a drift distance of 50 cm or smaller, the resolutions improve by a factor of ~ 2. For large inclination angles and large drift distances, the spatial resolutions increase to $\sigma_{r\phi} = 1.3{-}2.0$ mm and $\sigma_z = 1.5{-}2.3$ mm.

The separation of two close-by tracks is another important property. Figure 4.45 sketches the geometric layout of the cathode plane for separating two close-by tracks. The double track resolution is

$$\Delta z = v^e_d t_c + v^e_d t_d = v^e_d t_c + h/\tan\theta, \tag{4.41}$$

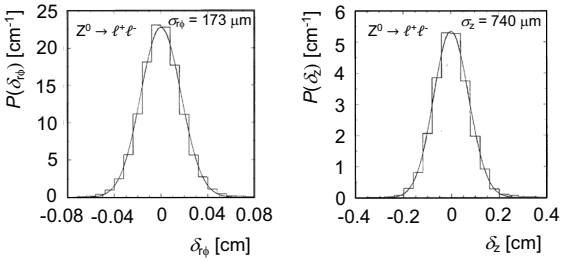

Fig. 4.42 The ALEPH position resolution in the $r\phi$ direction (left) and in the z direction (right) measured in $Z^0 \to \ell^+\ell^-$ decays. The $r\phi$ resolution is 173 μm while the z resolution is 740 μm. Reprinted with kind permission from [108], © 1991, Elsevier. All rights reserved

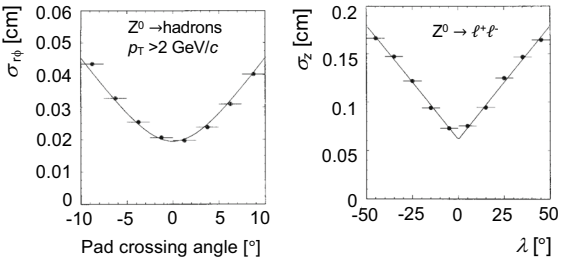

Fig. 4.43 Left: The $r\phi$ position resolution of the ALEPH TPC versus pad crossing angle measured in $Z^0 \rightarrow hadron$ events [108]. Right: The rz position resolution of the ALEPH TPC versus dip angle measured in $Z^0 \rightarrow \ell^+\ell^-$ decays. Both reprinted with kind permission from [108], © 1991, Elsevier. All rights reserved

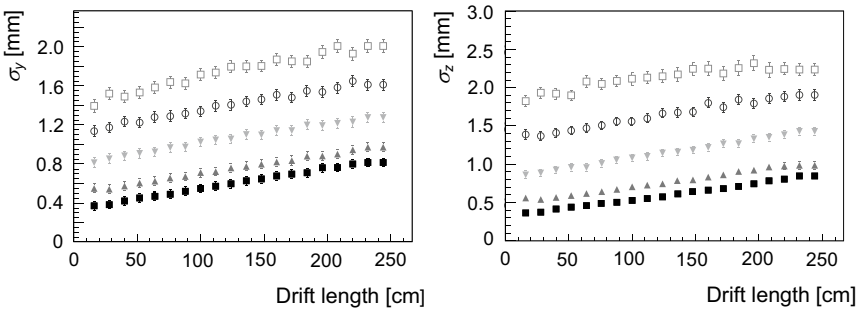

Fig. 4.44 The ALICE spatial resolution in the $r\phi$ (left) and z (right) directions as a function of the drift distance for different track inclination angles, $\tan(\alpha_{tr}) = 0$ (solid squares), $\tan(\alpha_{tr}) = 0.23$, (upward triangles), $\tan(\alpha_{tr}) = 0.46$ (downward triangles), $\tan(\alpha_{tr}) = 0.69$ (open circles) and $\tan(\alpha_{tr}) = 0.92$ (open squares). Reprinted with kind permission from [117], © 2010, Elsevier. All rights reserved

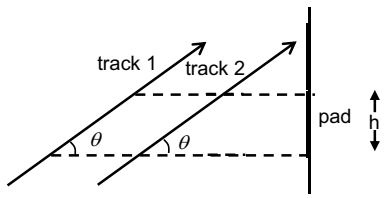

Fig. 4.45 Illustration of the separation of two-tracks

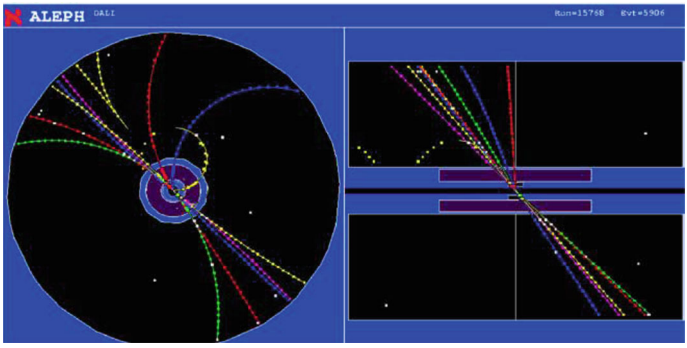

Fig. 4.46 One-event display of $Z \rightarrow hadrons$ in the ALPEH detector in the $r\phi$ and rz views, respectively. Reprinted with kind permission from [119], © 1996, the ALEPH Collaboration. All rights reserved

where v_d^e is the drift velocity, t_c is the intrinsic electronic pulse length, t_d is the drift time and h is the pad size. In the azimuth direction two tracks have to be separated by two to three pad widths in order to be resolved. We conclude this section with a one-event display from the ALEPH TPC in Fig. 4.46 showing the decay $Z^0 \rightarrow 2\ jets$. The individual charged tracks are well measured and clearly separated from each other.

4.6 Micro Strip Gas Chambers

Though the MWPC is one of the most widely used tracking detector it has two limitations. First, the spatial resolution in the direction perpendicular to the anode wires is limited by the wire spacing being ≥ 1 mm. Second, for rates $\geq 10^4$ particles/s/cm MWPCs develop an inefficiency that is caused by the slowly moving positive ions. To improve on these limitations, we have to reduce the wire spacing and the anode-cathode distance. However, wire spacings below 1 mm and anode-cathode gaps below 2 mm become difficult due electrostatic instabilities. Oed proposed a novel design by using photolithographic techniques that have accuracies of 0.1–0.2 μm [118]. This method allowed for the production of chambers with reduced anode wire pitch and anode-cathode gaps called MicroStrip Gas Chambers (MSGC). They consist of an array of parallel thin metallic strips, which are deposited by photography on an insulating support structure. Figure 4.47 (left) shows a schematic layout of an MSGC. The detector is made of two parts, a low electric-field drift region and a high electric-field amplification region as illustrated in Fig. 4.47 (right). Alternating anode strips and cathode strips are sandwiched between a conductive plane on the top kept at intermediate potential V_d and a cathode plane on the bottom at potential V_b that consists of strips orthogonal to the anode strips. The anode strips are kept at positive potential V_a while all cathode strips are kept at negative potential V_c.

Anode strips are typically 5–10 μm wide while cathodes strips are 60–100 μm wide and the anode pitch is 120–200 μm. The gap between the top plane and the

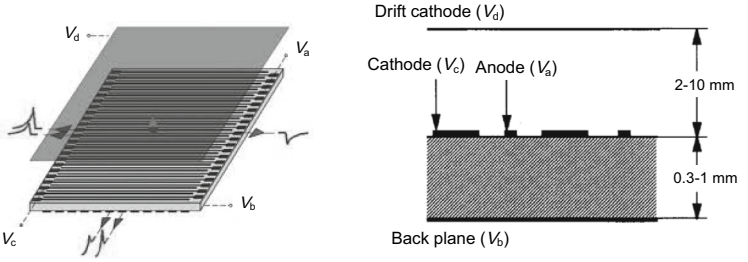

Fig. 4.47 Left: Schematic layout of a microstrip gas chamber [120]. Alternating anode strips and cathode strips are sandwiched between a drift cathode plane on top and cathode strips running perpendicular to the anode strips on the bottom. Reprinted with kind permission from [120], © 2004, IGI Publishing. All rights reserved. Right: A cross section through a microstrip gas chamber showing typical dimensions. Reprinted with kind permission from [121], © 1994, Elsevier. All rights reserved

plane containing the anode strips is the drift region and is 5–10 mm deep. The back cathode plane has wider strips (150 μm) and is separated from the anode plane by 500 μm thick glass, plastic or amorphous material, which has high resistivity (10^9-10^{15} Ω-cm).[12] This is necessary to prevent the build-up of ion clouds between strips at high rates. The chamber is operated with typical gas mixtures like Ar-CO_2, Ar-CH_4, Ar-DME, or Xe-DME. Primary electrons produced in an ionization process of a traversing charged particle produce an avalanche near the anode strips, which induces a negative signal on the anode strips and a positive signal on both neighboring cathode strips.

Several particle physics experiments have designed large arrays of MSGCs [31, 122]. The CMS experiment considered them as a baseline option. The HERMES experiment at DESY used them for tracking closest to the target [31]. The detector consisted of six planes, where four planes had strips running under angles of ±30°. The detector acceptance was 40 mrad $\leq |\theta_{\text{vertical}}| \leq$ 140 mrad and $|\theta_{\text{horizontal}}| \leq$ 170 mrad. For an anode strip width of 7 μm and a cathode strip width of 85 μm an anode pitch of 193 μm was chosen. The HERMES MSGC operated with a $\sim$ 94% efficiency. The average resolution was 71 μm. Despite large development efforts, MSGCs appeared to develop a fast degradation and discharge issues when operated at gains needed to observe MIPs, which sometimes caused irreversible damage. Though the chambers worked well in the laboratory under very high fluxes of X rays, they experienced instabilities and discharge-related damage when operated in test beams [123]. Thus, other technologies were favored for tracking detectors.

[12] The term Ω-cm refers to the volume resistivity or bulk resistivity of the semi-conductive material.

4.7 Gas Electron Multiplier

In 1996, Sauli introduced a new concept of gas amplification, called the gas electron multiplier (GEM) [126]. Instead of wires he used kapton sheets with holes as shown in Fig. 4.48 (left). The holes have a typical size of 50–100 μm in diameter with a pitch of 100–200 μm. Figure 4.48 (right) shows a microscope picture of a GEM foil. A high-gradient field is applied across the hole such that electrons start to avalanche in the hole. Using 200 V, the field strength reaches 40 kV/cm. Typical chamber gas mixture are used such as Ar-CH_4 (70:30).

The production of a GEM is a simple process, depicted in Fig. 4.49. We start with a sheet of copper-clad kapton. Using masking and exposure to ultraviolet light, we produce a pattern on the top and bottom of the copper layer. The copper is removed at the marked positions by etching and the channels are opened using a kapton solvent. Coupled with a drift electrode above and a readout electrode below the GEM layer, the device acts as a highly performing micro-amplifier. Figure 4.50 (left) shows the electric-field and equipotential lines. The advantage of this detector is that amplification and detection are decoupled allowing an operation of the readout at zero potential. The gain depends on the hole size and lies typically between a few hundred and 2000. The GEM foils are typically characterized by three parameters,

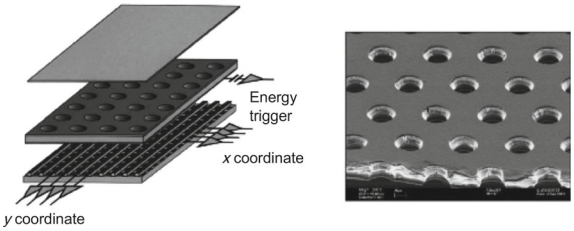

Fig. 4.48 Left: Schematic layout of a GEM detector. Reprinted with kind permission from [124], © 2016, Elsevier. All rights reserved. Right: Electron microscope picture of a GEM detector. Reprinted with kind permission from [125], © 2002, Elsevier. All rights reserved

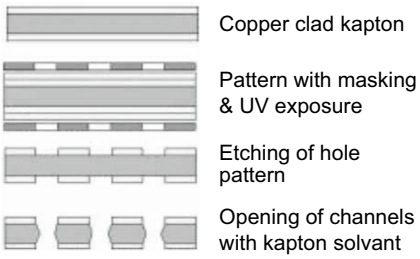

Fig. 4.49 Production of a GEM detector: a sheet of copper-clad kapton (top) is masked and exposed to ultraviolet light producing patterns on the top and bottom of the copper layer (center top). With etching the copper is removed at the marked positions (center bottom) and channels are opened using a kapton solvent (bottom). Reprinted with kind permission from [124], © 2016, Elsevier. All rights reserved

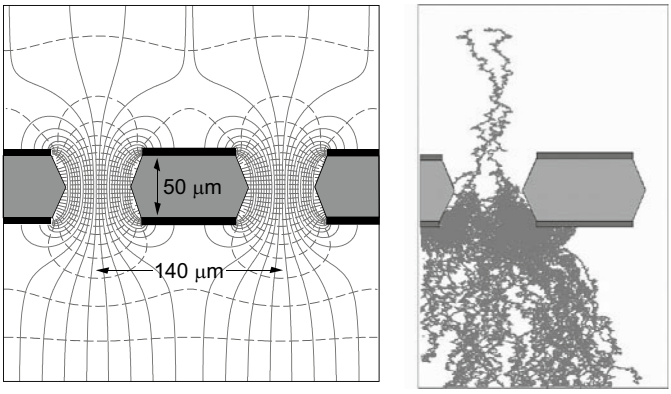

Fig. 4.50 Left: Electric-field configuration in a GEM detector depicting electric-field lines (solid curves) and equipotential lines (dashed curves) [56]. The top part is the conversion and drift region, the GEM layer is the amplification region and the bottom part is the transfer region. Reprinted under CC-BY-NC-4.0 Licence with kind permission from [56], © 2024, the Particle Data Group LBNL. Right: Avalanche formation of two primary electrons in the hole of a GEM detector [127]. Reprinted with kind permission from [10], © 1992, CERN. All rights reserved

the hole pitch (h_p), the hole diameter at the foil surface (h_2) and the hole diameter at foil center (h_1). Due to the etching process, the holes are not cylindrical but conical.

Figure 4.50 (right) illustrates the avalanche formation of two primary electrons in the hole. Primary electrons produced by a traversing charged particle drift towards the GEM, where they encounter a very high electric field and start to avalanche. The avalanche of electrons moves to the readout plane, where it is recorded. Assuming parallel plate geometry, the gain is obtained from the first Townsend coefficient α_I and the distance between the electrodes d_el by

$$A_\mathrm{GEM} \approx \exp(\alpha_\mathrm{I} d_\mathrm{el}). \tag{4.42}$$

The Townsend coefficient can be approximated by (3.16). Figure 4.51 (left, right) shows measurements of $\ln(A_\mathrm{GEM})/(P \cdot d_\mathrm{el})$ versus the electric field inside the hole divided by the pressure for pure argon, an Ar-CO_2 (70:30) gas mixture and methane in comparison to the calculated reduced Townsend coefficient α_I/P assuming parallel plate geometry.

Figure 4.52 shows the gain of GEM detectors as a function of the potential across the hole for different geometries. Using an Ar-CO_2 (70:30) gas mixture, the electric drift field in these measurements is set to 1 kV/cm. The highest gains of $A_\mathrm{GEM} >$ 1000 are achieved with small holes ($h_p/h_2/h_1$)=(140/45/30) and (140/60/30). The corresponding gains for large holes (200/140/110) are about 30. Figure 4.53 (left) shows the GEM amplification factor as a function of the metal hole diameter for the same geometries depicted in Fig. 4.52. The gain drops exponentially with the hole diameter. At hole diameters below 70 μm a saturation is observed. This is probably caused by a loss of charge due to diffusion. The pitch plays no role in the gain characteristics but restricts the values of the drift field for full collection. To increase

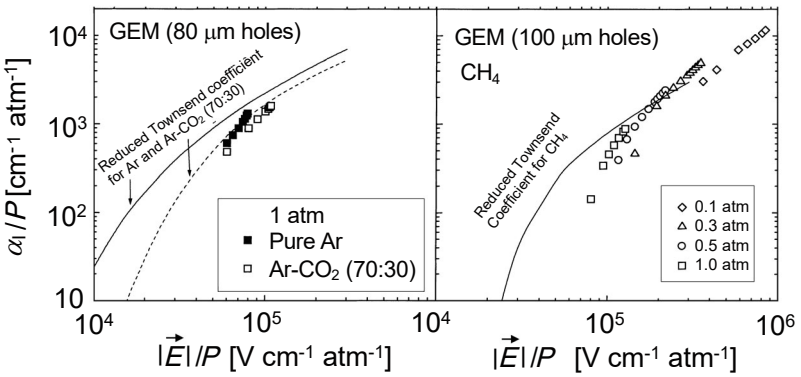

Fig. 4.51 Measurements of $\ln(A_{\mathrm{GEM}})/(P \cdot d_{\mathrm{el}})$ versus $|\vec{E}|/P$ in comparison to calculated reduced Townsend coefficients α_{I}/P for pure argon and Ar-CO_2 (70:30) (left) and CH_4 (right) at different pressures. Both reprinted with kind permission from [128], © 1999, Elsevier. All rights reserved

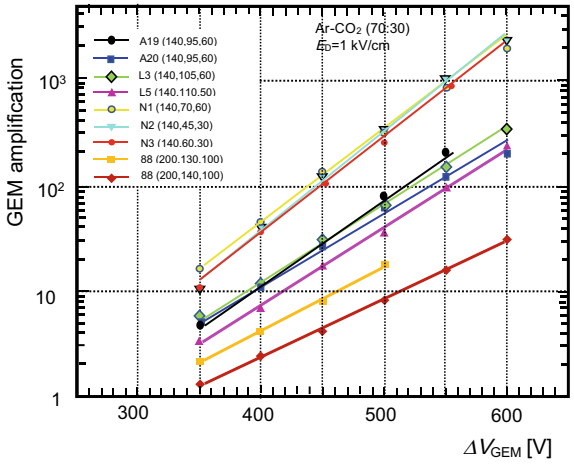

Fig. 4.52 Amplification factor of GEM detectors as a function of applied voltage for different GEM geometries: 140/95/60 (black solid points and blue solid squares), 140/105/60 (green solid diamonds), 140/110/50 (magenta solid upward triangles), 140/70/60 (yellow open circles), 140/45/30 (cyan solid downward triangles), 140/0/30 (red solid points), 200/130/110 (orange squares) and 200/140/110 (brown diamonds). The notation corresponds to the pitch/the diameter of the hole/the diameter of the hole at the center in units of μm. The drift electric field is $E_{\mathrm{drift}} = 1$ kV/cm in an Ar-CO_2 (70:30) gas mixture. Reprinted with kind permission from [129], © 1998, CERN. All rights reserved

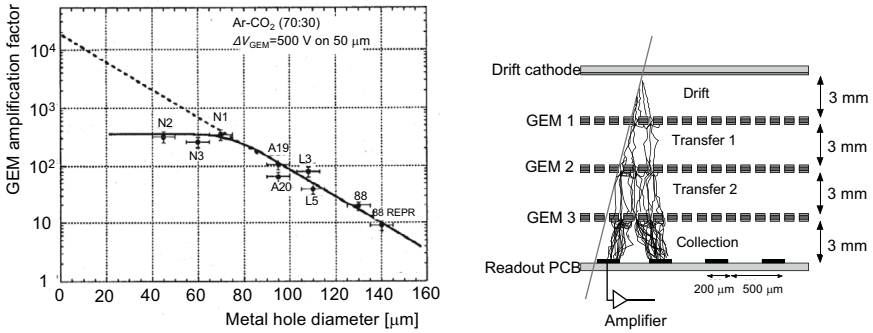

Fig. 4.53 Left: Amplification factor of the same GEM detectors as a function of the metal hole diameter. Reprinted with kind permission from [128], © 1999, CERN. All rights reserved. Right: Schematic view of a triple GEM used in the CMS experiment. The avalanche formation in the three GEMs is clearly visible. Reprinted with kind permission from [134], © 2020, IOP Publishing. All rights reserved

the gain several GEM layers may be combined. Figure 4.53 (right) shows a schematic layout of a triple GEM detector. It consists of a drift region, two transfer regions and a collection region. Electrons produced in the drift region start amplification in the first GEM foil. They transfer to the second GEM foil where amplification continues. The final amplification then occurs in the third GEM. Thus, higher amplifications are achieved than in a single GEM detector. Figure 4.54 (left) shows the gain of a triple GEM detector as a function of the applied voltage for different gas mixtures. In an Ar-CO_2 (70:30) gas mixture gains above 10^5 are achieved with voltages above 1,200 V distributed over the three GEM sections. An effective gain of 10^4 is achieved with an Ar-CO_2-C_4H_{10} (65:28:7) gas mixture around 1 kV.

Another important issue is the ion backflow. In a single GEM, the ion backflow fraction is close to the ratio of the drift field to the induction field. In a triple GEM a suitable sharing of the gains can substantially reduce its value. Figure 4.54 (right) shows the ion backflow fraction as a function of the gain in a double logarithmic scale for two drift field strengths and for different gas mixtures. The ion backflow fraction drops with increasing gain. A reduction of the drift field by a factor of five reduces the ion backflow by an order of magnitude. At a drift field of 0.5 kV/cm and low gains, the Ar-CF_4 (90:10) gas mixture shows a lower ion backflow than the Ar-CH_4 (90:10) gas mixture. At higher gains, however, the ion backflow for both gas mixtures becomes similar. For example, at a gain of 5×10^4 the ion back flow is less than 2%.

Several experiments use triple GEM detectors, including COMPASS[13] [130,131], TOTEM[14] [132,133], LHCb and CMS. For the readout of the ALICE TPC, the wire chambers are replaced by four-layer GEM detectors [137]. The GEM foils can be

[13] COMPASS is a fixed-target experiment at the SPS at CERN.
[14] TOTEM is located on both sides of the CMS detector and measures total, elastic and diffractive cross sections.

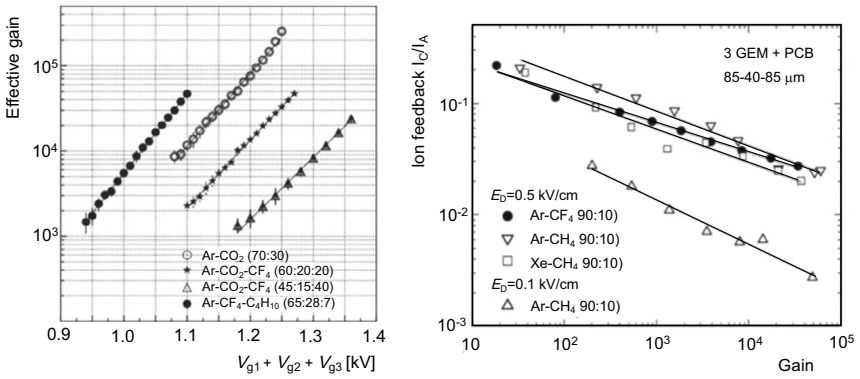

Fig. 4.54 Left: Effective gain of a triple GEM as a function of the applied voltage ($V_{g1} + V_{g2} + V_{g3}$) in the three GEM sections for different gas mixtures, Ar-CO_2 (70:30) [open circles], Ar-CO_2-CF_4 (60:20:20) [stars], Ar-CO_2-CF_4 (45:15:40) [triangles] and Ar-CF_4-C_4H_{10} (65:28:7) [solid points]. Reprinted with kind permission from [135], © 2004, Elsevier. All rights reserved. Right: The ion backflow fraction of a triple GEM with 85-40–85 μm hole sizes in the three layers. Data are shown for gas mixtures of Ar-CF_4 (90:10) [solid points], Ar-CH_4 (90:10) [downward triangles], Xe-CH_4 (90:10) [open squares], all for an electric drift field of $E_D = 0.5$ kV/cm and Ar-CH_4 (90:10) [upward triangles] for an electric drift field of $E_D = 0.1$ kV/cm. Reprinted with kind permission from [136], © 2003, Elsevier. All rights reserved

formed also into cylindrical shape as shown in Fig. 4.55 (left). This technology is used in the BoNus[15] TPC [138] and the upgraded four-layer KLOE tracker [139]. Further details on GEM detectors are given in reference [124]. We focus here on the LHCb and COMPASS chambers as an example and show some properties of the CMS GEM detectors.

The LHCb experiment used 12 GEM chambers in the innermost region of the first muon station because of their performances and radiation hardness [28,140]. Each chamber consisted of two triple GEM detectors superimposed. The sensitive area was 20 cm × 24 cm. The three GEM foils were sandwiched between anode and cathode planes. A GEM was made by a 5 μm thick kapton foil that was copper clad on each side and was perforated with a high surface density of holes. Each hole had a bi-conical structure with an external (internal) diameter of 70 μm (50 μm) and a pitch of 140 μm. The foils were stretched and were attached to fiber glass frames that defined the gaps. In order to limit the damage in case of discharge, one side of the GEM foil was divided into six sectors, 33 mm × 240 mm in size with a separation of 200 μm between sectors. The anode electrodes were segmented into 192 pads of size 1 cm × 2.5 cm. The detectors were read out on two sides. The chambers were operated with a gas mixture of Ar-CO_2-CF_4 (45:15:40) since a time resolution of 3 ns was measured instead of 10 ns for the Ar-CO_2 (70:30) gas mixture. The typical voltage difference between the two copper sides was 350 V to 500 V yielding electric

[15] BoNus is an experiment at the Thomas Jefferson Laboratory that studies the neutron structure in electron-neutron interactions.

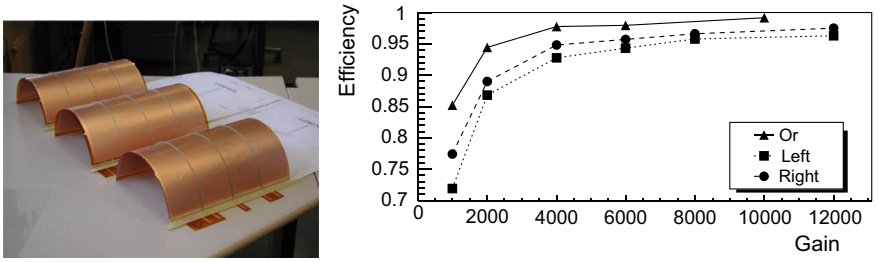

Fig. 4.55 Left: Cylindrical GEM electrodes. Reprinted with kind permission from [124], © 2016, Elsevier. All rights reserved. Right: The efficiency versus gain in a 20 ns time window for a chamber consisting of two triple GEM detectors. The terms left and right refer to one and the other triple GEM. Reprinted with kind permission from [141], © 2007, Elsevier. All rights reserved

fields up to 100 kV/cm inside the holes. Figure 4.55 (right) shows the efficiency as a function of gain for a chamber consisting of two triple GEM detectors. For a gain of 4,000 an efficiency over 98% was achieved if both sides of the chambers were read out.

The Compass experiment at CERN, which was built to study the spin structure in the proton and perform hadron spectroscopy, was the first experiment to use a triple GEM tracking detector [130,131]. The three GEM foils consisted of 50 μm thick kapton sheets covering an area of 31 cm $\times$ 31 cm with 5 μm copper cladding on each side. The holes were 70 μm in diameter and had a pitch of 140 μm. The three GEM foils were separated from each other and from the two-dimensional readout board by 2 mm spacers. The readout anode consisted of two sets of perpendicular strips placed at 400 μm pitch. The drift electrode was separated from the top GEM foil by a 3 mm spacer. The electric field for the drift region was 2.49 kV/cm while that across each GEM foil was 3.73 kV/cm. The gas mixture consisted of Ar-CO_2 (70:30). The amplification of the three-layer GEM was 9,800. The GEM detectors were mounted in pairs onto a large-area tracking detector with one detector rotated by 45° with respect to the other. This way, four projections (X,Y and U,V) were measured for each track crossing both GEM detectors of one station. The average efficiency was 97.2% in a single dimension and 95.6% in two dimensions. The position resolution in each plane was $\sigma_{x,y} = 71.6$ μm. If large-angle tracks were discarded the resolution improved to $\sigma_{x,y} = 69.6$ μm.

The CMS experiment has started to upgrade the inner region of the first two layers of the forward muon system using triple GEM detectors [142]. The first layer will have 144 chambers. The GEM foils are 50 μm thick copper-cladded polyimide foils with holes etched in a hexagonal pattern. The holes have a diameter of 70 μm separated by a 140 μm pitch resulting in a distance of 70 μm between two consecutive holes. The chambers are operated with an Ar-CO_2 (70:30) gas mixture. The electric field in the hole is 60 kV/cm. The efficiency is expected to be larger than 97%.

4.8 Micro Mesh Gaseous Structure

To overcome limitations of MWPCs, the micro-strip gas chamber was developed. However, one limitation of MSCGs is that the gain does not exceed 10^4 because the electric field cannot be increased further due to the electric breakdown of the insulator. One new approach proposed by Giomataris [143] is the Micro-Mesh Gaseous Structure (Micromegas), which overcomes this problem. Figure 4.56 (left) shows a schematic layout of a Micromegas detector, which is a two-stage parallel plate avalanche chamber. Figure 4.56 (right) shows a cross section through a Micromegas detector [144]. A drift electrode is placed 3–5 mm above a micro-mesh, which in turn is positioned 50–130 μm above the anode plane consisting of 9 μm thick and 200–400 μm wide gold-plated copper strips that are printed on a 1 mm substrate. Using vacuum deposition, thinner strips can be produced. If needed, both metal deposition techniques are applicable on a 50 μm thick Kapton substrate. The strip pitch is 50–100 μm larger than the strip width. Each readout strip is connected to a low-noise charge-sensitive amplifier ($\sim$ 4 V/pC) with a feedback capacitor. With high-precision polymide spacers, a precise gap can be maintained. The micro-mesh, a 3 μm thick metallic grid with 17 μm openings every 25 μm, is made of nickel using the electroforming technique [145]. With use of this high-resolution emulsion process, a high precision is ascertained to better than 1 μm. The transparency of the micro-mesh was measured to be 45%. The drift electrode consisted of a 100 μm thick nickel mesh having a transparency of 80%. The gas consisted of Ar or Ne with 5–10% admixtures of CO_2, CH_4, C_4H_{10} or DME. A window is built in the center of the chamber allowing to place radioactive sources that are necessary for testing. A newer production technique is based on a woven wire mesh [146].

While readout strips are at ground potential, the micro-mesh and the drift electrode are at different high voltage. The electric field $\vec{E}_D$ in the drift region is 1–5 kV/cm, while the electric field $\vec{E}_A$ in the amplification region is 40–100 kV/cm. The ratio $|\vec{E}_A|/|\vec{E}_D|$ is tuned to large values to achieve optimal operation of this detector. It is also required to catch the positive ions produced in the amplification gap. The high electric field in the amplification region is necessary to quickly collect the positive ions on the micro-mesh. Figure 4.56 (right) also shows the ionization processes of a straight and an inclined charged track traversing the Micromegas detector. The primary electrons from the ionization processes of the straight track are closely spaced. They drift to the amplification region and produce avalanches that are collected by the resistive strips and induce signals on the readout strips. Typically, only one or two strips record the signal. For the inclined tracks the electrons are more spread out. So more readout strips record the signal.

Figure 4.57 (left) shows the electric-field configuration in the drift region and in the amplification region. Due to the two different magnitudes of $|\vec{E}_D|$ =1–5 kV/cm and $|\vec{E}_A|$ =30–50 kV/cm, a funnel effect occurs as illustrated in Fig. 4.57 (right). The electric-field lines are compressed between drift region and the amplification region. Due to the funnel effect, the signal S_1 in the drift region will be projected into the signal S_2 on the anode plane. The ratio S_1/S_2 is approximately given by the ratio $|\vec{E}_A|/|\vec{E}_D|$. For large values of $S_1/S_2 \sim 25/1$, where S_2 is small with respect

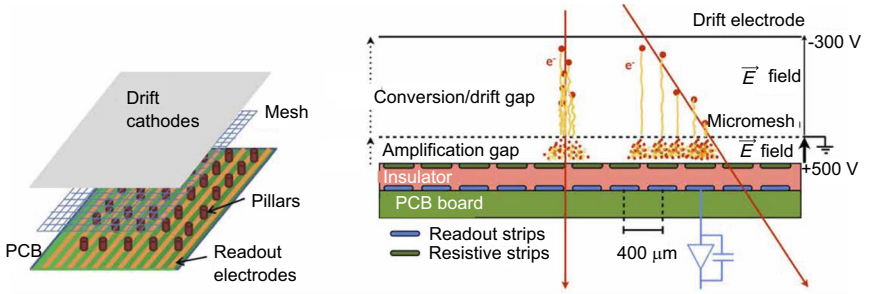

Fig. 4.56 Left: Schematic layout of a Micromegas detector (see text). Reprinted with kind permission from [147], © 2004, Elsevier. All rights reserved. Right: Cross section through a Micromegas detector showing the drift electrode, the micro-mesh, the amplification gap and the readout electrodes. The production of primary ions in the drift region and the avalanche formation in the amplification region is shown for a straight track and an inclined track. Reprinted with kind permission from [148], © 2017, Elsevier. All rights reserved

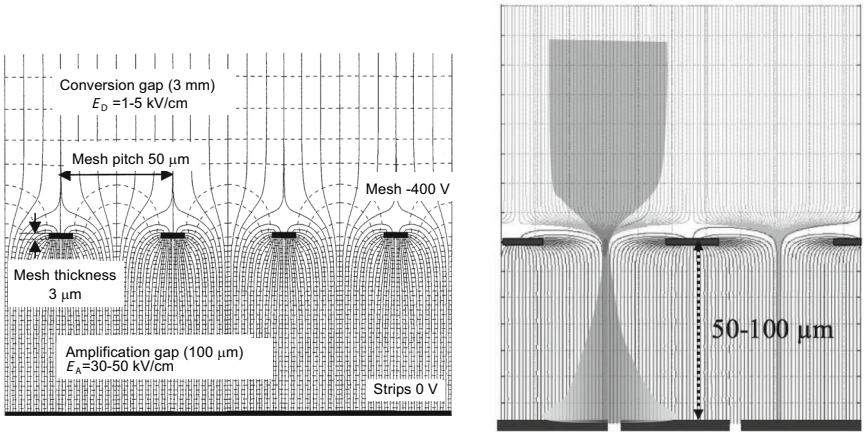

Fig. 4.57 Left: Micromegas electric-field map showing the 3 mm thick conversion gap, the 3 μm thick mesh and the 100 μm thick amplification gap. The electric field in the drift region is $|\vec{E}_D|$ =1–5 kV/cm and that in the amplification region is $|\vec{E}_A|$ =30–50 kV/cm. Reprinted with kind permission from [149], © 1999, Elsevier. All rights reserved. Right: The funnel effect in a Micromegas detector. Charge produced in the drift region is transmitted through a narrow funnel into the amplification regions where due to diffusion a broadening occurs before collection by the resistive strips. Reprinted under CC-BY-4.0 Licence from [150], © 2013, M. Titov

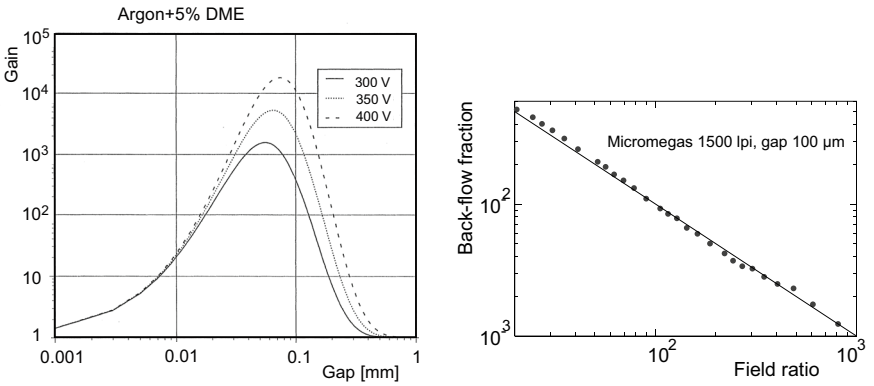

Fig. 4.58 Left: Gain as a function of the gap distance between the micromesh and the anode plane in an Ar-DME (95:5) gas mixture for three different voltages. The optimal gap size is 50–100 μm. Reprinted with kind permission from [149], © 1999, Elsevier. All rights reserved. Right: Ion backflow fraction as a function of the field ratio for a Micromegas detector with 1500 lines per inch and a 100 μm gap size. Reprinted with kind permission from [147], © 2004, Elsevier. All rights reserved

to the avalanche cloud size, it is unlikely that the ions will follow back the field lines into the drift region. Most ions get collected by the mesh.

Figure 4.58 (left) shows the gain as a function of the gap between the micro-mesh and the anode plane in an Ar-DME (95:5) gas mixture for different voltages. The optimal gap size is 50–100 μm. Micromegas detectors operating with such gap sizes are not sensitive to defects in flatness and to variations of the gas pressure. Thus, they have a much larger dynamic range of operation before breakdown. For gap sizes of 50 - 100 μm, signals are fast. Similar gap sizes have been found for a He-isobutane (92:8) gas mixture [144]. Another important parameter is the ion back flow, which drops with a larger $|\vec{E}_A|/|\vec{E}_D|$ ratio. Figure 4.58 (right) shows the ion back flow fraction as a function of the field ratio $|\vec{E}_A|/|\vec{E}_D|$ for an Ar-CH_4 (93:7) gas mixture. The Micromegas detector has a 100 μm gap and uses a mesh of 1500 lines per inch (lip). The ion back flow is independent of magnetic fields [147].

In the narrow amplification gap the electron avalanche is typically collected by one strip. Thus, the spatial resolution is determined by the strip pitch. In order to spread the electron avalanche among several strips two modifications can be done. The first one is to introduce a pre-amplification in the drift gap. This is accomplished by adding a second high-voltage grid in the drift gap as shown in Fig 4.59 (left) [151]. With a potential of 1.52 kV, the electrons are accelerated sufficiently to produce several secondary electrons before reaching the amplification region. With a conversion gap of 3 mm the charge distribution is sufficiently broadened when reaching the amplification region. The avalanche formation in the amplification region broadens the charge distribution further, which is recorded by multiple cathode strips.

The second procedure consists of using a resistive readout. To make a Micromegas detector resistive the pads are covered by a 200 μm insulating layer acting as the capacitance and then a 50 μm kapton with a thin Diamond-Like Carbon layer provid-

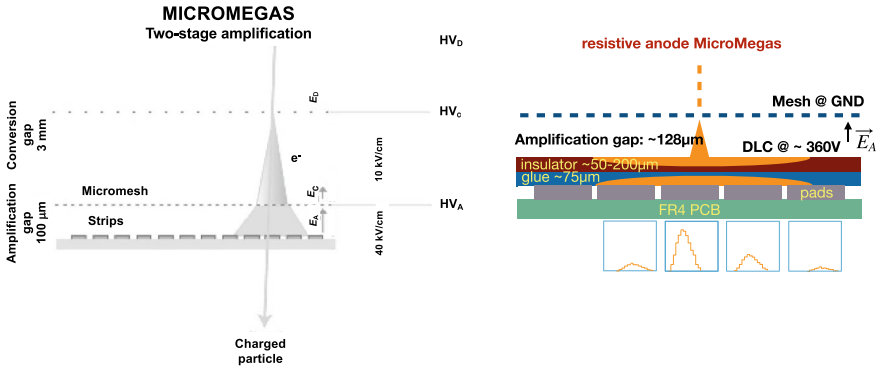

Fig. 4.59 Left: Micromegas detector with preamplification. Here, a high-voltage plane is introduced into the drift region to produce secondary electrons. Since these are more spread out than the primary electrons, the amplification in the amplification gap yields a more spread out charge distribution that induces signals on more readout strips. Reprinted with kind permission from [151], © 2002, Elsevier. All rights reserved. Right: Layout of the resistive Micromegas detectors. The bottom plots show the signal distributions. The electron distribution (light grey) is spread across several pads. With the COG method excellent spatial resolutions are achieved. Reprinted with kind permission from [152], © 2020, IOP Publishing. All rights reserved

ing a designed resistivity of 2.5 MΩ/square.[16] Figure 4.59 (right) shows the layout of a resistive Micromegas detector. The electron avalanche in resistive Micromegas detectors is spread over several strips. Thus, the position is obtained from the COG method yielding better spatial resolutions than for a single strip.

Micromegas detectors may encounter sparking. Though sparking does not damage the chambers it leads to increased dead times. Figure 4.60 shows the efficiency and spark probability as a function of amplification for a Micromegas detector operating with a Ne-isobutane gas mixture (95:5). For a gain above 7,000, the efficiency reaches a plateau above 98% independent whether pre-amplification is used or not. The spark probability is rather low. Without a preamplifier the spark rate is less than 10^{-6} for a gain of 10,000. With a preamplifier the spark rate is further reduced by more than two orders of magnitude. Furthermore, dead zones are potentially very small and the chambers are robust with respect to aging. So, Micromegas detectors are stable devices that are easy to build at low costs. They operate at high efficiencies at high rates. Figure 4.61 (left) shows a comparison of the relative gain versus rate for an MWPC, an MSCG and a Micromegas detector. While the efficiency of MWPCs already starts to drop at rates above 10^4 mm^{-2}s^{-1} and that of MSGCs drops above 10^6 mm^{-2}s^{-1}, Micromegas detectors are still 100% efficient at rates around 10^{10} mm^{-2}s^{-1}. Thus, they are superior to the other two tracking chambers. They also provide ionization measurements.

[16] This is the sheet resistance, which is used when measuring a layer or thin film of a semi-conductive material.

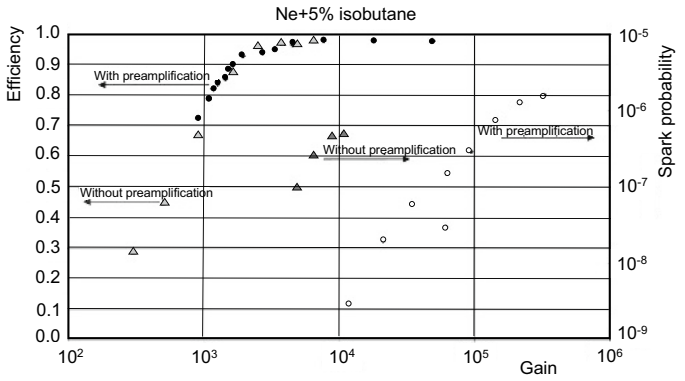

Fig. 4.60 Efficiency (solid points and triangles on the left-hand side of the plot) and spark probability (open points and triangles on the right-hand side of the plot) of a Micromegas detector as a function of the total gain for a Ne-isobutane gas mixture (95:5). Measurements are shown with pre-amplification (points) and without pre-amplification (triangles). Reprinted with kind permission from [151], © 2002, Elsevier. All rights reserved

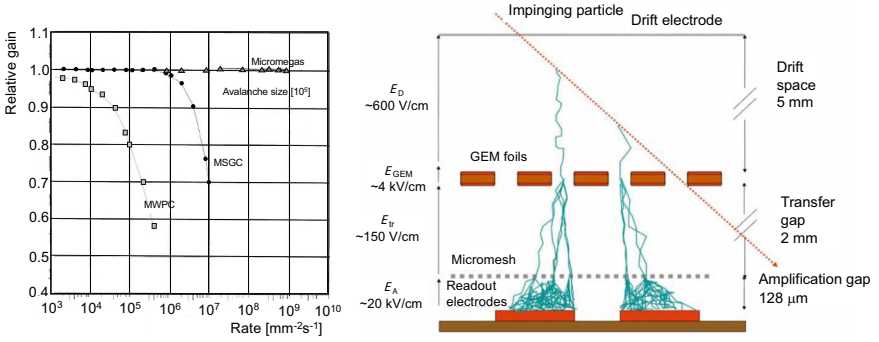

Fig. 4.61 Left: Comparison of the relative gain for an MWPC (squares), an MSGC (points) and a Micromegas detector (triangles) as a function of exposed event rate [154]. Reprinted with kind permission from [154], © 1998, Elsevier. All rights reserved. Right: Schematic layout of a Micromegas detector with a GEM foil in the drift gap [155]. The drift region is 5 mm, followed by a 2 mm transfer gap and a 128 μm amplification gap. The drift field is 600 V/cm and the electric field in the GEM is 4 kV/cm. In the transfer region the electric field is 150 V/cm increasing to 20 kV/cm in the amplification gap. Reprinted under CC-BY-3.0 Licence from [155], © 2013, F. Thibaud

Resistive Micromegas detectors have excellent spatial resolution. In his first prototype, Charpak measured the spatial resolution with two detectors placed back-to-back [149]. Since the two measurements on the track are so close, multiple scattering is negligible. Assuming that both Micromegas have the same resolution, the standard deviation of the position difference measurement divided by $\sqrt{2}$ yields the position resolution of one Micromegas detector. For a detector with a 3 mm drift gap and a 100 μm amplification gap in an Ar-DME (90:10) gas mixture, Charpak measured a spatial resolution of the order of 65 μm independent of the gain of the chamber.

Simulation studies indicate that the resolution is mainly determined by the transverse diffusion in the gas. For a 3 mm drift, the measurements are consistent with a transverse diffusion of 200 μm. Using mixtures with CF_4 instead of cyclohexane reduces the diffusion coefficient by a factor of three and increases the number of primary electrons by a factor of 3–4. Simulations indicate that for this geometry a resolution of 10 μm is expected. For drift fields of 0.4 kV/cm and 2.7 kV/cm in a CF_4-iC_4H_{10} (80:20) gas mixture, measurements yielded position resolutions of 18 μm and 11 μm, respectively [153]. In fact, Charpak built Micromegas prototypes at Saclay that consisted of nickel-electroformed micromesh cathodes with square holes of 39 μm $\times$ 39 μm at a 50.8 μm pitch with 500 lines per inch (LPI). The anodes consisted of copper strips on a PCB with a pitch of 100 μm. The drift gap was 3 mm and the amplification region was 100 μm thick. All gaps were maintained with precise spacers. The chambers were operated with a CF_4-isobutane gas mixture (80:2). For a drift electric field of $E_D = 1.5\,\mathrm{kV/cm}$, the measured spatial resolution was 14 ± 3 μm [153].

Micromegas detectors are used in several experiments, for example, in the COMPASS tracker, the T2K TPCs, in digital hadron calorimeters (DHCAL) and ATLAS New Small Wheels. Their properties are summarized in Table 4.6 and photographs of a 1.8 m $\times$ 0.8 m plane with 12 detectors for the T2K TPC, a 1 m $\times$ 1 m plane with six detectors for a DHCAL prototype and a 1 m $\times$ 2 m plane of a Micromegas prototype for the ATLAS Small Wheel are shown in Fig. 4.62 (left, center, right), respectively. We present some more details of the COMPASS and the ATLAS Micromegas.

The COMPASS experiment was the first high-energy physics experiment to use Micromegas detectors for tracking. The 12 Micromegas detectors had an active area of 40 cm $\times$ 40 cm with a blind disk of 5 cm diameter around the beam direction [156, 157]. The chambers were arranged in three sets of X, Y, U (45°) and V (−45°) layers. The drift gap was 2.5 mm and the amplification gap was 100 μm. While the drift electric field was 1 kV/cm, the amplification electric field was 50 kV/cm. The chambers were operated with a Ne-C_2H_6-CF_4 (80:10:10) gas mixture at a typical gain of 6,000. The readout strips had a pitch of 360 μm in the central part of the detector (512 strips), which was increased to 420 μm in the outer part (2 $\times$ 256 strips). The chambers performed well. The detection efficiency was above 98%. The spatial resolution was 70 μm for inner strips and 78 μs for outer strips. The time resolution was measured to 9.3 ns. However, an issue of discharges remained. To reduce the rate by a factor of 10–100 one solution was to add a GEM foil into the drift region.

The upgraded COMPASS experiment uses 12 layers of Micromegas detectors arranged into three stations with four layers each [164]. The active area is 40 cm $\times$ 40 cm around the beam pipe with a hole 5 cm in diameter cut out around the beam pipe. To reduce the spark probability a GEM foil is inserted into the drift gap as shown in Fig. 4.61 (right). The anode plane is divided into three zones, a central zone with 512 strips placed at a 360 μm pitch and two outer zones, each with 256 strips placed at a 420 μm pitch. The detectors have a parallel plate electrode structure with a volume separated into a 5 mm conversion gap, a 2 mm transfer gap and a 128 μm amplification gap. The electric fields in the drift region, across the

Table 4.6 Examples of Micromegas detectors showing the task, amplification mesh structure, drift mesh structure, diffusion gap size, amplification gap size, active area, total area, gain, gas mixture, gas fraction, electric field in the drift region $|\vec{E}_D|$, electric field in the amplification region $|E_A|$, readout strip pitch, readout pad pitch, efficiency and spatial resolution in $r\phi$. Note that LPI stands for lines per inch. ‡Four active detector layers are combined into a quadruplet. †The spatial resolution depends on the electron drift distance in the TPC, which is affected by diffusion. The two values correspond to the small and maximum drift distance, respectively. §The first value is for inner strips, the second for outer strips; the old detector COMPASS measured 65 μm

Experiment	COMPASS	T2K	DHCAL	ATLAS
Reference	[157,158]	[159,160]	[161,162]	[163]
Task	Tracking	TPC readout	Hadron energy	Muon tracker‡
Amplification mesh [LPI]	500	400	230	325
Diffusion gap [mm]	3.2	–	3	5
Amplification gap [μm]	100	128	128	128
Active area [cm × cm]	40 × 40	96 × 96	33 × 50	
Total area [m^2]	0.32 × 12	9	1	1,280
Gain	6,000	500–2,000	4×10^4	7,000
Gas mixture	Ne-C_2H_6-CF_4	Ar-CF_4-iC_4H_{10}	Ar-CF_4-iC_4H_{10}	Ar-CO_2-iC_4H_{10}
Fraction [%]	(80:10:10)	(95:3:2)	(95:3:2)	(93:5:2)
$\lvert\vec{E}_D\rvert/\lvert\vec{E}_A\rvert$ [kV/cm]	1/50	0.2/25–28.1	0.3/28.9	0.6/40.6
Strip pitch [μm]	360/420§§	–	–	& 425–450
Pad pitch [mm × mm]	–	9.8 × 7.0	10 × 10	–
Efficiency [%]	>98	≈ 100	≈100	>90
$\sigma_{r\phi}$ [μm]	70/78§	300–700†	–	109

GEM layer and in the amplification region are 0.6 kV/cm, 4 kV/cm and 20 kV/cm, respectively. The micromesh consists of a 5 μm thick non ferromagnetic copper grid foil. The chambers are run with the same gas mixture as before. The GEM foil reduces the spark probability as shown in Fig. 4.63 (left), which decreases with a larger electric field across the GEM gap. For a gap voltage of 1260 V the spark probability is already reduced by more than two orders of magnitude with respect to the Micromegas detector without the GEM foil. The mean efficiency of the chamber pixels is better than 97%. The spatial resolution of the pixels (strips) is < 87 μm (72 μm) and the time resolution for both is about 9 ns.

The ATLAS New Small Wheels consists of 16 detector planes, eight detection layers of small-strip Thin Gap Chambers for the trigger (discussed in Sect. 4.14)

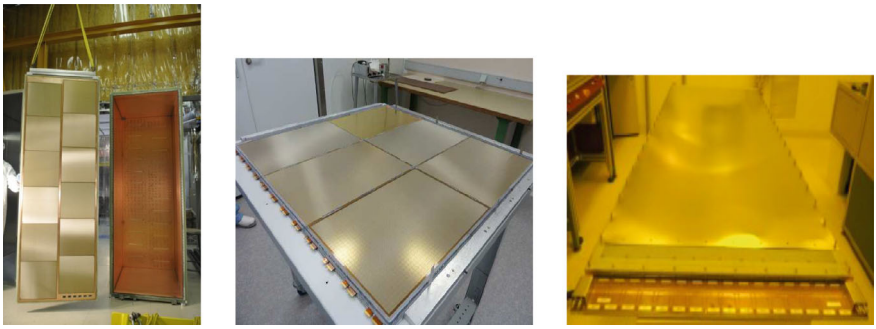

Fig. 4.62 Left: Photograph of a T2K-TPC Micromegas readout plane that consists of 12 detectors spanning an area of 1.8 m × 0.8 m. Reprinted under CC-BY Licence from [165], © 2011, A. Delbart. Center: Photograph of a 1 m × 1 m Micromegas prototype for reading out a digital hadron calorimeter. Reprinted under CC-BY Licence from [161], © 2011, C. Adloff. Right: Photograph of a 1 m × 2 m Micromegas prototype for the ATLAS New Small Wheel. Reprinted with kind permission from [166], © 2023, ATLAS Collaboration. All rights reserved

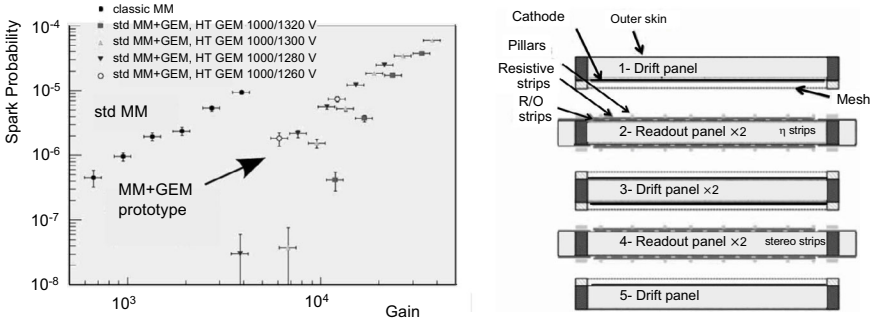

Fig. 4.63 Left: Spark probability of a Micromegas detector with and without a GEM foil as a function of gain for different potentials across the GEM, 1,320 V (squares), 1,300 V (upward triangles), 1,280 V (downward triangles) and 1,260 V (open circles). Reprinted with kind permission from [167], © 2010, the COMPASS Collaboration. All rights reserved. Right: Expanded view of an ATLAS quadruplet Micromegas detector used in the New Small Wheel. The top panel houses the first Micromegas detector with the drift region (light grey), cathode and the micromesh. The second panel, which houses the readout (dark dashes) and resistive strips (grey dashes) of the first Micromegas is just separated by pillars (light grey dots) from the first panel. For illustrative purpose, the panels are pulled apart. The bottom part of this panel holds the readout and resistive strips of the second Micromegas, which follows on the top of the third panel. The bottom side of this panel houses the third Micromegas whose readout is placed on the top side of the fourth panel. The bottom side houses the strips of the fourth Micromegas, which is placed on the fifth panel. Reprinted with kind permission from [163], © 2019, ATLAS Collaboration. All rights reserved

and eight resistive Micromegas layers for precision muon tracking [163]. The Micromegas layers use four axial layers and four U and V stereo layers with angles of $\pm 1.5°$, respectively. Four layers are combined into a quadruplet as shown in Fig. 4.63 (right). The chambers have a 5 mm conversion gap and a 128 μm amplification gap. The electric fields in the two regions are 0.6 kV/cm and 44.5 kV/cm, respectively. The resistive strips have a resistivity of 10 to 20 MΩ/cm. The copper readout strips have a width of 300 μm with a pitch of 425 μm or 450 μm. The mesh is supported by 128 μm high pillars, which guarantee the uniformity of the amplification gap. The cathode is also a PCB having a copper surface. The chambers operate with an Ar-CO_2 (93:7) gas mixture. The drift velocity is $v_d^e = 5$ cm/μs leading to a maximum drift time of 100 ns. For an electric field of $|\vec{E}_A| = 4.5$ kV/cm the gain is 20,000 yielding 100% efficiency. A spacial resolution of 90 μm has been measured.

4.9 Resistive Plate Chambers

Resistive plate chambers (RPCs) were first proposed by Santonico and Sardelli [168]. Figure 4.64 shows the layout of a generic single-gap RPC, which consists of two parallel plates made of a semi-conductor material like painted glass or bakelite covered with linseed oil. The semi-conductor has high resistivity of $\rho_{sc} = 10^{11} - 10^{13}$ Ω-cm. A 2 mm thick gas gap between the plates is introduced by PVC spacers or fishing lines. Graphite layers on the outside of the semiconductor plates define electrodes. The top layer is at ground potential while the bottom layer is set to high voltage. The chamber is read out by x and y strips that are separated from the graphite electrodes via an insulator. Instead of strips also readout pads are used. The charge on the strips or pads is produced via capacitive coupling. While the x strips record positive signals the y strips see negative signals. The RPC is enclosed in a copper sheet providing a

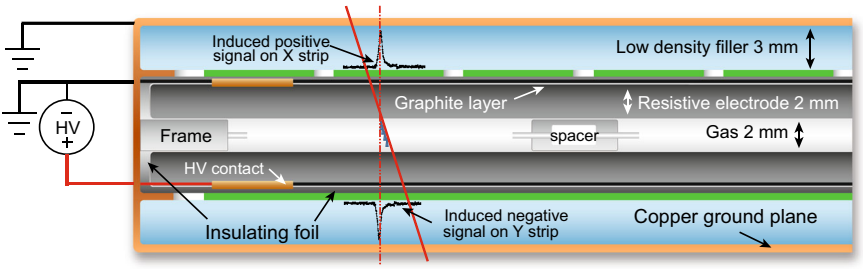

Fig. 4.64 Schematic cross section of a generic single-gap resistive plate chamber. A frame and spacers or fishing lines define a 2 mm gas gap between 2 mm thick resistive electrodes. The electrodes are connected to high voltage, where the cathode is on top and the anode on the bottom. An insulating foil decouples the readout strips from the high voltage. Strips on the top (bottom) run in the x (y) direction. The strips are covered by a 3 mm thick layer of low-density filler and a copper ground plane. A traversing charged particle induces a positive (negative) signal on the x (y) strips. Reprinted under CC-BY-NC-4.0 Licence with kind permission from [56], © 2024, the Particle Data Group LBNL

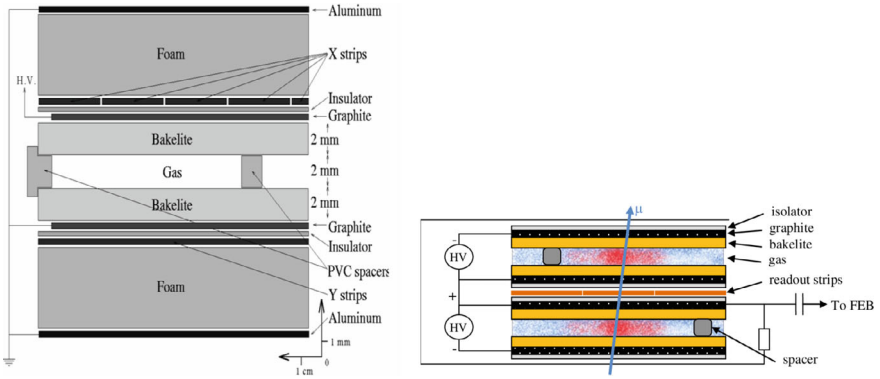

Fig. 4.65 Left: Schematic layout of a single-layer resistive plate chamber used in the *BABAR* experiment. Reprinted with kind permission from [169], © 2003, Elsevier. All rights reserved. Right: Schematic layout of the CMS double-gap RPC. The readout strips at ground potential lie between the two gaps [170]. Reprinted with kind permission from [170], © 2020, IOP Publishing. All rights reserved

shield, which is insulated from the readout strips by a low-density filler like foam. Note that these chambers use no wires in the sensitive region. Large chambers can be built. Typical sizes are 2 m length and 1 m width. The potential across the gas gap is 8 kV or even higher. Most RPCs use either argon-based gases with admixtures of freon and isobutane or $C_2H_2F_4$-based gases with admixtures of C_4H_{10} and SF_6. For example, the ATLAS RPCs use $C_2H_2F_4$-C_4H_{10}-SF_6 (94.7:5.0:0.3).

The *BABAR* experiment had instrumented the iron flux return with 19 single-layer planar RPCs in the barrel and 18 single-layer planar RPCs in each endcap [77]. Figure 4.65 (left) shows the layout of the planar RPCs. The readout strips run both parallel (ϕ strips) and orthogonal to the beam direction (z strips). The layers in the barrel were arranged into hexagonal sectors. A barrel layer was segmented into three modules of rectangular shape. In addition, a cylindrical double layer of RPCs was inserted between the electromagnetic calorimeter and the coil with a total of 32 curved modules. So, there were 374 RPC modules in the barrel and 216 RPC modules in each endcap. The endcap modules had trapezoidal-shaped RPCs in the top, center and bottom regions. The two center modules had an additional circular cutout for beam elements. All single-layer RPCs had a 2 mm gas gap while the double-layer RPCs had two 2 mm gas gaps. Each barrel planar layer had 96 ϕ (z) strips running parallel (perpendicular) to the beam direction. For all layers the z strip pitch was 2.8 cm while the ϕ strip pitch varied between 2 cm and 3.5 cm depending on the layer position. Besides ϕ and z strips, the cylindrical double layers had two planes of strips rotated by 30° in addition to reduce ambiguities. An endcap layer had 64 horizontal strips with 2.8 cm pitch in each region and between 55 and 80 vertical strips with 3.8 cm pitch depending on the position in the layer. The RPC electrodes were high-resistivity ($10^{11} - 10^{12}$ Ω-cm) bakelite plates painted with graphite. Two pick-up strip planes, placed on both sides of the chamber provided two-dimensional readout. The chambers used a gas mixture of Ar-$C_2H_2F_4$-C_4H_{10} (60.6:34.9:4.5).

The two graphite surfaces were connected to high voltage (8 kV) and ground, and protected by an insulating mylar film. The position resolutions was of the order of 1 cm.

Other multi-gap devices have been built as well. The CMS experiment uses two-gap RPCs. Figure 4.65 (right) depicts a schematic layout of them. Each 2 mm thick gap is sandwiched between two 2 mm thick layers of bakelite having a resistivity of $1 - 2 \times 10^{10}$ Ω-cm. The readout strips kept at ground potential and being parallel to the beam direction are located between the two gaps. In the barrel 480 rectangular RPCs are installed, most of which have a length of 2.455 m. The strip widths increase from the inner stations to the outer ones to preserve projectivity. Each strip covers 0.13° in the azimuth angle. The high voltage across each gap is 12 kV. The chamber gas consists of $C_2H_2F_4$-iC_4H_10-SF_6 (96.2:3.5:0.3). Further details are given in reference [171]. Some experiments use even higher-gap RPCs. For example, the ALICE experiment uses a ten-gap chamber in the time-of-flight counters [172].

If a charged particle passes through the gas, an electron from an electron-ion pair produces an avalanche with high amplification. Depending on the electric-field strength the electron produces an avalanche (proportional mode) or a streamer (streamer mode). Thus, Resistive Plate Chambers can be operated in the proportional (avalanche) or in the streamer mode. For example, the *BABAR* planar RPCs were operated in the streamer mode. Figure 4.66 (left) shows the RPC efficiency versus particle rate for operation in the proportional and streamer modes. In the avalanche mode, the chamber is more efficient at higher rates than in the streamer mode. Figure 4.66 (right) shows the RPC efficiency versus high voltage for operation in proportional and streamer modes. For operation in the proportional mode high efficiency is obtained at lower high voltages. Increasing the high voltage keeps the efficiency of the chamber high. However, the contribution from proportional signals to streamer signals changes.

Resistive Plate Chambers are simple, cheap, large area detectors with high efficiency. Thus, they are used in multipurpose detectors, typically in muon systems,

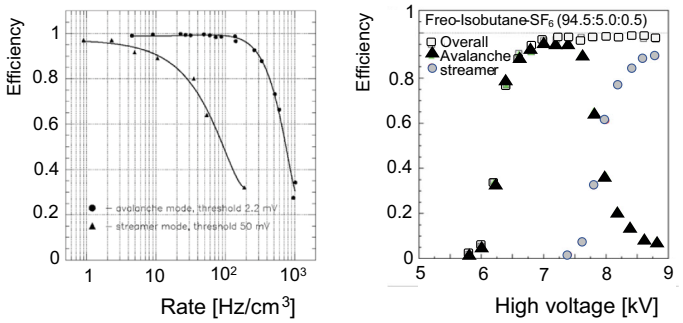

Fig. 4.66 Left: Efficiency of RPCs as a function of event rate for avalanche mode (points) and streamer mode (triangles). Reprinted with kind permission from [173], © 2004, Elsevier. All rights reserved. Right: Efficiency of RPCs as a function of the applied high voltage for avalanche mode (triangles), streamer mode (points) and their combination (squares). Reprinted with kind permission from [174], © 2005, World Scientific. All rights reserved

where large areas need to be instrumented. Besides *BABAR* also Belle [176] used RPCs in the segmented muon systems, where two RPCs with two readout planes were merged into one superlayer unit. We already mentioned the RPC systems in the ATLAS [180,181] and CMS [171] muon systems as well as the usage in the ALICE time-of-flight system [185]. The ALICE experiment also uses RPCs in the muon system [172]. Table 4.7 summarizes characteristics of RPCs in some multipurpose detectors. We selected a few examples out of the many RPCs used in experiments [186–191]. Most RPCs are single-gap devices. The main gas component is $C_2H_2F_4$. Some are operated in the streamer mode, some in the proportional mode. Since most of the RPCs are used in muon systems for the trigger, the spatial resolution was not optimized. However, good timing resolution and high efficiencies are important for the trigger, which RPCs have. Figure 4.67 (left) shows the time resolution of the ATLAS RPCs in η and ϕ directions yielding $\sigma_t^{\eta} = 1.44$ ns and $\sigma_t^{\phi} = 1.64$ ns. Time resolutions measured in the CMS experiment are 1–2 ns. Figure 4.67 (right) shows the muon efficiency in the CMS experiment as a function of the effective high voltage for different background rates. For a low background rate, an efficiency $> 95\%$ is achieved around 7.2 kV. For a background rate of 2.3 kHz the high voltage has to be increased to$>$7.5 kV to obtain an efficiency of $> 95\%$. The CMS experiment will replace RPCs in the inner rings of station 3 and 4 in the endcaps [170]. In the new chambers both the thickness of the electrode and that of the gas gap will be decreased to 1.4 mm. This reduces the recovery time and thus increases the rate capability in the high-luminosity running of the LHC. In addition, a smaller gap reduces the cluster size for readout strips with a smaller strip pitch ($<$10 mm). Also, the chambers will operate at lower high voltage.

In *BABAR*, the RPCs developed problems [193]. Dark currents increased and efficiencies dropped down to 40%. This was caused by the formation of linseed oil stalagmites. Three basic conditions have to be met enable the formation of stalagmites:

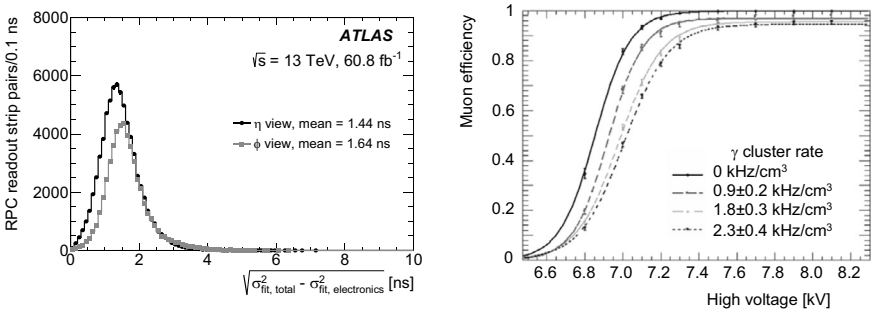

Fig. 4.67 Left: Intrinsic ATLAS RPC time resolution in the η and ϕ directions. Reprinted with kind permission from [192], © 2021, ATLAS Collaboration. All rights reserved. Right: Muon efficiency in the CMS experiment as a function of the effective high voltage measured at different background rates, 0 kHz (solid curve), 0.9 kHz (dashed curve), 1.8 kHz (dash-dotted curve) and 2.3 kHz (dotted curve). Reprinted with kind permission from [170], © 2020, IOP Publishing. All rights reserved

Table 4.7 Examples of resistive plate chambers in recent experiments at B-factories and at the LHC. Listed are the detector system, total area, number of layers (barrel/endcaps), operation mode, number of gaps per chamber, gap size, type of semiconductor electrode, high voltage, bulk resistivity ρ_b, surface resistivity ρ_{surf}, gas mixture, gas fractions, readout pitch in the barrel (ϕ/z or η/ϕ), readout pitch in the endcaps (x/y or ϕ/θ)), efficiency per layer, position resolutions $\sigma_{r\phi}(\sigma_\eta)$, $\sigma_{rz}(\sigma_\phi)$ and time resolution σ_t. In CMS strips run parallel to the beam in the barrel and in radial direction in the endcaps. †There are two one-gap chambers. *In layer 2 chambers in the center have 3 gaps. *This is for the barrel. For the endcaps it is a factor of ten higher. ‡The efficiency deteriorated over time. §The first value refers to η strips and the second to ϕ strips. #The first value is for clusters with one strip and the second for clusters with two strips

Experiment	*BABAR*	Belle	ALICE	ATLAS	CMS	ALICE
Reference	[77,175]	[176,177]	[172,178, 179]	[180–182]	[171,183]	[184,185]
System	muon	muon	muon	muon trigger	muon	TOF
Area [m^2]	2,000	2,200	143	3,650	2,953	141
# Layers b/e	19/18	15/14	-/4	2 × 3/-	6/4	1/-
Mode	Streamer	Streamer	Streamer	Prop	Prop	Prop
# gaps	1	2†	1	1	2 (3)*	10
Gap [mm]	2	1.9	2	2	2	0.25
Electrode	Bakelite	Glass	Bakelite	Bakelite	Bakelite	Glass
HV [kV]	8.0	8.0	10.3	9.35/9.55	8.5–9.0	12–13
ρ_b [Ω-cm]	$10^{11}-10^{13}$	10^{12}	3×10^9	10^{10}	$1-2\times10^{10}$	10^{13}
ρ_{surf} [MΩ/square]	0.1	1–10*	–	0.1	–	few
Gas mixture	Ar-$C_2H_2F_4$-iC_4H_{10}	Ar-$C_2H_2F_4$-C_4H_{10}	SF_6-$C_2H_2F_4$-C_4H_{10}	$C_2H_2F_4$-C_4H_{10}-SF_6	$C_2H_2F_4$-C_4H_{10}-SF_6	$C_2H_2F_4$-C_4H_{10}-SF_6
Composition [%]	60.6:34.9:4.5	30:62:8	0.3:89.7:10	94.7:5:0.3	96.2:3.5:0.3	90:5:5
b: RO strip	ϕ/z	ϕ/z	–	η/ϕ	ϕ	–
[cm]	2.0–3.3/3.8	5/5	–	2.3–3.5/same	2.3–4.1/2.0–3.6	–
e: RO strip	x/y	ϕ/θ	x/y	–	ϕ	–
[cm]	2.8/3.8	1.9–4.7/3.6	1,2,4/same	–	1.95–3.63	-
Pad RO [cm^2]	–	–	–	–	–	3.5 × 2.5
Efficiency [%]	94.8‡	≥ 98	95	98.5	96–97	99
σ_ϕ (σ_η) [mm]	10	11–17	2.1–5.9	(3.7, 7.3)#	b: 8.1–13.2	–
σ_z (σ_ϕ) [mm]	10	11–17	2.1–5.9	(5.8, 6.3)#	e: 8.6–12.8	–
σ_t [ns]	1.3	few	2	1.46, 1.56§	≤ 2	0.056

- Sufficient linseed oil on the bakelite surface.
- Elevated temperature to soften the uncured oil film so oil molecules become movable.
- A high electric field on the surface to help pull the softened oil film away from the electrode and reach the opposite electrode.

Since the oil stalagmites could not be removed from the chambers without opening them, three procedures were tried out in a test chamber to reduce the impact of the stalagmites:

- Flow of an N_2-O_2 (60:40) gas mixture.
- Flow of dry air.
- Placing the chamber in a metal box maintained at 10% of relative humidity by flushing it with dry nitrogen gas and flowing pure argon gas through the chamber.

After some short-term improvements the efficiency dropped again. Thus, *BABAR* replaced poorly working RPCs in the barrel with limited streamer tubes. Some of the Belle RPCs developed problems showing increased dark currents and lower efficiencies [194]. This was tracked down to high levels of water vapor that was coming through the plastic tubing. After replacing the plastic tubes with copper tubes the chambers returned to normal behavior.

4.10 Limited Streamer Tubes

Limited streamer tubes (LST) were first developed by Iarocci and collaborators at Frascati [195]. Thus, they are also called "Iarocci Tubes". The basic structure is an eight-cell extruded PVC open profile with a cross section of (1–3 cm) × (1–3 cm) and a length of 1–10 m. Figure 4.68 shows an exploded view (left) and a cross section (right) of a single-layer LST. In the center, we see the extruded PVC open profile with anode wires. On top we have a ground plate covered with ϕ strips and on the bottom a ground plate with z strips. The tube walls are coated with graphite having a resistivity of $10 - 10^2$ kΩ/cm. The center of each cell holds an anode wire that is typically 100 μm in diameter. The cathode strips run both parallel and perpendicular to the wires. The whole system is inserted into an uncoated PVC box. A high voltage of 4.5–5.0 kV is applied. The gas typically consists of an Ar-CO_2-iC_4H_{10} mixture, where CO_2 is the dominant component. Figure 4.69 (left, right) shows the construction of a *BABAR* LST chamber and a close-up view of the readout side, respectively.

A charged particle produces electron-ion pairs in the gas volume. The electrons drift towards the anode wire and start to avalanche in the vicinity of the wire. Due to the high electric field, some avalanche clusters grow large and dense enough to excite neighboring ions and create a streamer. The streamer grows throughout the cluster and the high charge density affects the sensitivity of the wire in a region around the streamer. This region of the wire will be unable to produce new streamers until the ions have moved away. Atac and collaborators have photographed limited streamers in an Ar-ethane (50:50) gas mixture [199]. They found that limited streamers are filaments that are 150 μm to 200 μm wide extending along the electric-field lines. The filaments grow with increasing high voltage to a few millimeters from the anode wire. Similar streamer sizes are expected for other gases.

In the proportional mode, the measured charge of the anode wire is proportional to the charge of the primary ionization. In the limited streamer mode, this is different.

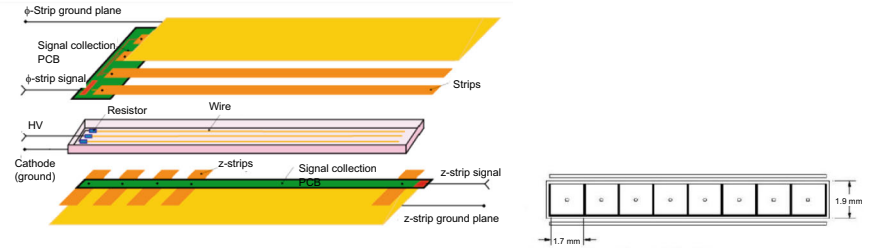

Fig. 4.68 Left: Exploded view of a limited streamer tube [196] showing the extruded PVC profiles hosting the anode wires, a top ground plate with ϕ strips and a bottom ground plate with z strips. Reprinted with kind permission from [196], © 2003, *BABAR* Collaboration. All rights reserved. Right: Cross section through the *BABAR* single-layer LST [197] showing the eight cells with the anode wire in the center and the top lid. The cell size is 17 mm × 15 mm. Reprinted with kind permission from [197], © 2005, SLAC. All rights reserved

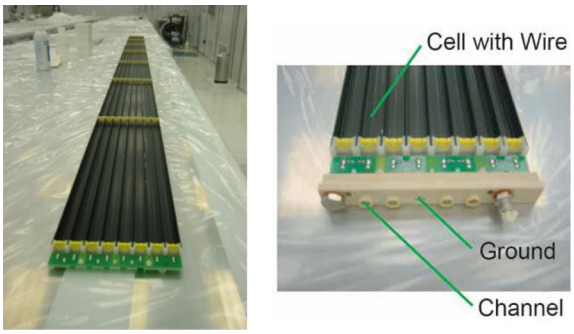

Fig. 4.69 Left: Construction of a *BABAR* LST chamber. Reprinted with kind permission from [198], © 2005, *BABAR* Collaboration. All rights reserved. Right: Close-up view of a *BABAR* LST module near the readout side. Reprinted with kind permission from [78], © 2013, *BABAR* Collaboration. All rights reserved

The discharge is nearly independent of the primary ionization. It occurs on a section of the anode wire. It has been shown that the discharge takes place over a small region of the wire and does not extend the entire distance between the anode and the cathode [199]. Therefore, it is different from a Geiger-Müller discharge in which the entire cell would be discharged. The limited streamer mechanism is observed in chambers using thick wires (>40 μm) and heavily quenched gases such as Ar-CO_2-iC_4H_{10}.

Limited Streamer Tubes have several advantages:

(i) A large anode signal of ∼50 mV/50 Ω load, which permits the usage of simple readout electronics.
(ii) A small dead zone ($30 - 300\ \mu s \cdot cm$).
(iii) Easy fabrication and reliable performance due to the thick anode wire.
(iv) No need for preamplifiers since signals are large (30 pC).
(v) Reasonably fast pulses with a rise time of the order of 30 ns.

(vi) Low cost detector allowing to cover large areas.
(vii) High efficiencies, typically >95%.

In the proportional mode the charge is approximately given by [17],

$$Q(V) = Q_0 \exp\left\{\kappa_p \sqrt{\frac{V_0}{V_{\rm tp}}}\left(\sqrt{\frac{V_0}{V_{\rm tp}}} - 1\right)\right\} \simeq Q_0 \exp\left(\kappa_p \frac{V_0}{V_{\rm tp}}\right), \tag{4.43}$$

where Q_0 is the initial ionization charge, κ_p is a constant depending on the gas mixture, temperature and pressure, V_0 is the applied voltage and $V_{\rm tp}$ is the threshold for operation in the proportional mode. In the streamer mode the relation simplifies to

$$Q(V) = \beta_{\rm ls}(V_0 - V_{\rm ts}), \tag{4.44}$$

where $V_{\rm ts}$ is the threshold for operation in the streamer mode and β_{ls} is another constant. Note that the anode charge Q depends only weakly on the input charge. To minimize crosstalk between adjacent strips, the termination resistor in the high-voltage board circuit was tuned to $R_T = 150\ \Omega$. The efficiency for x-strips is larger than 90% and for y-strips it is about 90%. Figure 4.70 (left) illustrates that the linearity in (4.44) holds for higher voltages. Another important characteristics of an LST is that the slope $\beta_{ls} = dQ/dV$ is independent of the gas composition [200]. Furthermore, for different wire diameters d_w the slopes and anode voltages satisfy the relation,

$$\beta_1 V_1 = \beta_2 V_2, \tag{4.45}$$

or

$$Q - Q_c = \beta_i V_i, \tag{4.46}$$

where Q_c is a constant independent of the wire diameter. Figure 4.70 (right) shows that the data follow the linear behavior of the charge on $V_0 - V_{\rm th}$. The anode voltages for different wire diameters and the same outer diameter $d_{\rm out}$, satisfy the relation

$$\frac{V_1}{V_2} = \xi_{12} = \frac{\log(d_{\rm out}/d_2)}{\log(d_{\rm out}/d_1)}. \tag{4.47}$$

Figure 4.71 (left) depicts the voltage ratio as a function of ξ_{12} demonstrating that the linear relation is correct. The positive ions produced near the anode wire influence the electric field and thus shape the avalanche formation. The number of electrons increases exponentially,

$$\mathrm{d}N_e = N_e \alpha_I(r)\mathrm{d}r, \tag{4.48}$$

where $\mathrm{d}N_e$ is the number of electrons produced in the radial segment $\mathrm{d}r$ and $\alpha_I(r)$ is the first Townsend coefficient, which was defined in (3.16). The total number of electrons in the avalanche is given by

$$N_e = N_{0,e} \exp \int_{d_w/2}^{r_0} \alpha_I(r)\mathrm{d}r, \tag{4.49}$$

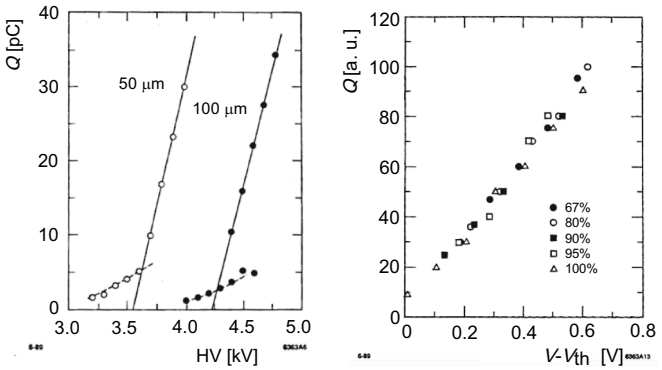

Fig. 4.70 Left: Anode charge versus anode voltage for a chamber with 50 μm diameter wires (open points) and 100 μm diameter wires (solid points) measured in reference. The low-charge points are measurements in the proportional mode while the high-charge points are those in the streamer mode. Note that the charge in the proportional modes has an exponential dependence on the voltage while that in the streamer mode has a linear voltage dependence. Reprinted with kind permission from [201], © 1989, Elsevier. All rights reserved. Right: The collected charge versus $V - V_{\text{th}}$ (V_{th} is threshold voltage) for wires with 70 μm diameter in an 8 mm × 8 mm cell for different Ar-CO_2 gas mixtures, with CO_2 contents of 67% (solid points), 80% (open circles), 90% (solid squares), 95% (open squares) and 100% (triangles). Reprinted with kind permission from [200], © 1989, Elsevier. All rights reserved

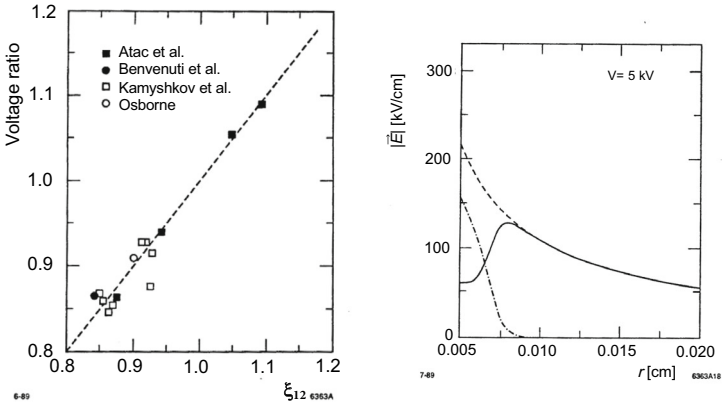

Fig. 4.71 Left: The voltage ratio versus ξ_{12} for data from Osborne [202] (open circles), Benvenuti [201] (solid points), Kamyshkov [203] (open squares) and Atac [199] (solid squares). Right: Electric-field strength as a function of the distance from the wire for an anode voltage of 5 kV showing the total electric field (solid line), that of the positive ions $|\vec{E}_{ion}(r)|$ (dash-dotted curve) and that of the wire $|\vec{E}_w(r)|$ (dashed curve). Both reprinted with kind permission from [200], © 1989, Elsevier. All rights reserved

where the integral extends from the wire radius to the radius of primary ionization and $N_{0,e}$ is the number of primary electrons. So the electron avalanche is highly non-linear but is proportional to the number of primary electrons. Let us look at an example. For argon gas, $c_1^{\mathrm{Ar}} = 14/\mathrm{cm/Torr}$ and $c_2^{\mathrm{Ar}} = 180$ V/cm/Torr while for CO_2 we get $c_1^{CO_2} = 20/\mathrm{cm/Torr}$ and $c_2^{CO_2} = 466$ V/cm/Torr. Thus, for a wire of 100 μm in diameter held at 4.75 kV the electric field is $|\vec{E}| = 2.1 \times 10^5$ V/cm yielding Townsend coefficients of $5.6 \times 10^3/\mathrm{cm}$ for argon and $2.8 \times 10^3/\mathrm{cm}$ for CO_2. Most of the multiplication occurs near the wire. This causes a large space charge effect of slowly moving ions reducing the electric field

$$|\vec{E}_{\mathrm{total}}| = \frac{V}{r \ln (d_{\mathrm{out}}/d_1)} - |\vec{E}_{\mathrm{ion}}(r)|, \tag{4.50}$$

where $|\vec{E}_{\mathrm{ion}}(r)|$ is the field of the positive ions. The electric field of the wire $|\vec{E}_w(r)|$ becomes distorted by the positive ions. The total electric field near the anode becomes quasi constant as shown in Fig. 4.71 (right). As the voltage increases, the distortion increases but the value of the total electric field does not change.

Most LSTs are used in muon systems or in hadron calorimeters. Thus, the spatial resolution is not crucial and has not been pushed. Typical resolutions are of the order of few mm to more than 10 mm. D'Agostini and collaborators built a prototype chamber at CERN to study the spatial resolution [204]. The LST chamber had a sensitive area of about 40 cm $\times$ 40 cm built from five basic modules. A basic module consisted of eight 9 mm $\times$ 9 mm cells, each of which had an anode wire 100 μm in diameter placed in its center. The walls of the eight-cell single extruded PVC profile were coated with graphite having a resistivity of 150–200 kΩ/square. The chambers were operated with an argon-isobutane (33:67) gas mixture at 4.8 kV. For the signal readout, the chambers used two planes of strips. Strips parallel to the wires had a pitch of 0.5 cm while those perpendicular to the wires had a pitch of 1 cm. In the direction perpendicular to the wires the spatial resolution was 350–500 μm and that parallel to the wires was 600 μm. The reason for having a worse resolution for the smaller pitch strips was allocated to higher noise.

As examples, we list properties of the SLD, *BABAR*, OPAL, DELPHI, ZEUS, H1 and MACRO LSTs in Table 4.8. Like RPCs, LSTs have a wide range of applications for large systems like tracking, muon detection and hadron calorimeters. The main gas component is CO_2, butane or pentane operating at high voltages typically above 4 kV. For high reliability, the diameter of the sense wires is typically 100 μm. Efficiencies are high and spatial resolution are less important. We give some more details of the SLD and *BABAR* LSTs.

The warm-iron calorimeter of the SLD detector, which served as a tail catcher of hadron showers and as a muon identifier, used 10,000 LSTs in the iron flux return yoke of the SLD magnet. The LSTs consisted of single layers sandwiched between two electrode sheets. Their lengths varied between 1.9 m to 8.6 m. The LSTs covered an area of 4,500 m^2. The tube walls were covered with graphite with resistivities between 50 kΩ/square and 2 MΩ/square. In addition to the sense wires, the tubes were equipped with 0.8 cm wide copper cathode strips ($x-$strips) on the bottom

Table 4.8 Examples of limited streamer tubes in different experiments showing the detector subsystem, number of LST cells N_{cell}, number of cells per extrusion N_{cell}/ext, profile material, wire material, cell size, cell length ℓ_{LST}, wire diameter d_w, pitch of strips running parallel to anode wires x_{str}, pitch of strips running perpendicular to anode wires y_{str}, pad size, anode high voltage, resistivity of cathode coating ρ_c, gas mixture, gas fractions, efficiency, spatial resolution in $r\phi$ or x and spatial resolution in z or y. All Cu-Be wires have a silver wire coating. Note that b (e) stands for barrel (endcap), w (s) stands for wire (strip) and h (v) stands for horizontal (vertical). ‡Properties are for the endcap muon detectors, which have two double layers. A double layer contains one layer with horizontal wires and one with vertical wires. †The resolution is determined from the pitch divided by $\sqrt{12}$. ⋆The hadron calorimeter has a tower structure; so, the pad sizes are given by $\Delta\theta \times \Delta\phi$, which correspond to pad sizes of about 20 cm × 30 cm. In the endcaps the polar angle bin is $\Delta\theta = 2.62°$. *The wire pitch is 10 mm. §The first value refers to the barrel and the second to the endcaps. #The strips are at a stereo angle of 26.5°. &Two of the 63 planes have an efficiency of 60%. §§The resolution of the pads is 10 cm

Exp.	SLD	*BABAR*	OPAL	DELPHI	ZEUS	H1	MACRO
Ref.	[201]	[78,206]	[207,208]	[209,210]	[211,212]	[63,213]	[214,215]
System	Muon	Muon	Muon ‡	HCAL	Muon	Muon	Tracking
N_{cell}	40,336	9,096	42,496	19,032	43,392	103,000	49,536
N_{cell}/ext	8	7,8	8	8	8	8	8
Material	PVC	PVC	PVC	PVC	Noryl	Luranyl	PVC
Wire	Cu-Be	Au-W	Cu-Be	Cu-Be	Cu-Be	Cu-Be	Cu-Be
Cell [cm^2]	0.9 × 0.9*	1.5 × 1.7	0.9 × 0.9*	0.9 × 0.9*	0.9 × 0.9*	1.0 × 1.0*	2.9 × 2.7
ℓ_{LST} [m]	1.9–8.6	3.75	6	0.4–4.1	0.7–10.1	0.4–2.4	12
d_w [μm]	100	100	100	80	100	100	100
x_{str} (ϕ) [mm]	8	w: 17	8	8	–	–	31+1.5#
y_{str} (z) [mm]	40/20§	(35+2)	8	–	13+2	17+3	55+5
Pad size	20 × 20	–	–	$\Delta\phi$: 3.75°	–	b: 40 × 50	–
[cm^2]	–	–	–	$\Delta\theta$: 2.96°⋆	–	e: 28 × 28	–
HV [kV]	4.75	5.5	4.3	3.92	4.8	4.5	4.23
ρ_c [$\frac{\text{k}\Omega}{square}$]	50–2,000	100–600	5,000	50& 150	100	10–30 & 10^4	< 1kΩ
Gas mixture	Ar-CO_2-iC_4H_{10}	Ar-CO_2-iC_4H_{10}	Ar-iC_4H_{10} –	Ar-CO_2-iC_4H_{10}	Ar-iC_4H_{10} -	Ar-CO_2-iC_4H_{10}	He-C_5H_{12} –
Fraction [%]	(2.5:88:9.5)	(3:89:8)	(25:75)	(10:60:30)	(25:75)	(2.5:88:9.5)	(73:27)
Efficiency [%]	90	88	96.7	>95	80–90	80 ± 10&	95
σ_x (σ_ϕ) [mm]	2.3–3.5	w: 4.9†	h: 3	$\Delta\phi$ 1.08°†	w: 2.5	w: 3–4	w: 10
σ_y (σ_z) [mm]	11.5–17/5.8–8.6	(10.7)†	v: 1	$\Delta\theta$ 0.85°†	s: 0.94	s: 10–15§§	s: 0.2°

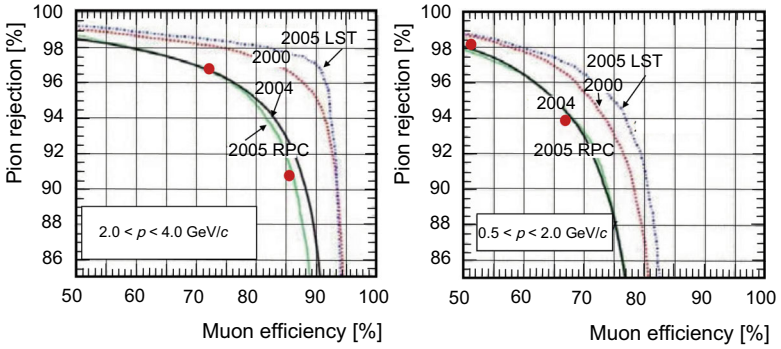

Fig. 4.72 Left: Pion rejection versus muon efficiency for high-momentum muons of the *BABAR* limited streamer tubes (upper dotted curve) compared to that of the resistive plate chambers in 2000 (lower dotted curve), 2004 (solid black curve) and 2005 (solid green curve). The red point points represent cut-based selections made in 2000. Right: The same curves for low-momentum muons. Both reprinted with kind permission from [218], © 2005, SLAC. All rights reserved

running parallel to the wires and cathode pads (20 cm × 20 cm) on top of the tube. Some chambers also had 4 cm wide copper strips ($y-$strips) that ran perpendicular to the anode wires. Signals were induced via capacitive coupling similarly as in the RPCs. The LSTs were operated with an Ar-CO_2-iC_4H_{10} (2.5:88:9.5) gas mixture at a high voltage of $\sim$ 4.7 kV [201].

As mentioned before the *BABAR* experiment replaced all RPCs in the barrel with single-layer LSTs made from extruded PVCs. The cell size was 1.5 × 1.7 cm^2. The inner surface was coated with graphite providing a resistivity between 0.2 to 1 MΩ/square. In addition, ϕ- and z- cathodes strips were implemented both having a width of 38.5 mm. The ϕ-strips ran parallel and the z-strips perpendicular to the anode wires. The sense wires were connected to 5.5 kV while the cathode was kept at ground. The LSTs operated with an Ar-iC_4H_{10}-CO_2 (3:8:89) gas mixture. The efficiency was above 95%. Figure 4.72 (left, right) displays the performance of the *BABAR* LSTs with respect to that of the *BABAR* RPCs. The LSTs showed a higher efficiency at a higher pion rejection than the RPCs even before degradation. For low-momentum muons, the LSTs performed better than the RPCs.

4.11 Drift Tubes

A drift tube consists of a few-meter-long aluminum pipe that has a diameter of a few centimeters. In its center an anode wire is positioned with a precision of better than 20 μm. The anode wire is on a high potential while the tube is grounded. The counter is operated with an Ar-CO_2 gas mixture. The tubes are glued together to form layers. Typically, three or four layers are combined to form a chamber. Thus, large-area chambers can be built easily at low costs. Since they have excellent spatial resolution, they are used as large-area tracking detectors in muon systems as in the ATLAS and CMS experiments, which we discuss briefly below. Figure 4.73 (left) shows

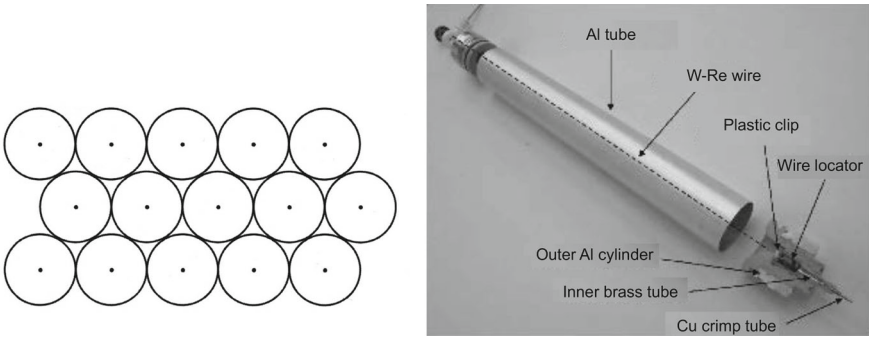

Fig. 4.73 Left: Schematic layout of a three-layer monitored drift tube chamber. Reprinted with kind permission from [42], © 2014, F. Sauli. All rights reserved. Right: Photograph of a monitored drift tube. Reprinted with kind permission from [219], © 2007, Elsevier. All rights reserved

a schematic layout of a monitored drift tube (MDT) chamber and Fig. 4.73 (right) shows a photograph of an individual MDT counter. Besides cylindrical drift tubes also square tubes are used. In the preparations for the GEM (Gammas, Electrons, Muons) detector [205] at the Superconducting Super Collider (SSC) in Texas,[17] studies with drift tubes operating in the streamer mode were conducted. The aluminum tubes had a square cross section of 22.8 mm $\times$ 22.8 mm in a 4 $\times$ 4 layout. The anode wires in the center of each cell consisted of gold-plated tungsten wires 100 μm in diameter. Readout strips 2.5 cm wide were placed orthogonal to the wires. The chamber was tested with different gas mixtures. For an Ar-C_4H_{10} (25:75) gas mixture at 5.4 kV a spatial resolution of 55 μm was measured in a muon beam [216]. Figure 4.74 (left) shows the drift-time-to-drift-distance relation in this prototype, which is nearly linear. Figure 4.74 (right) shows the spatial resolution as a function of the drift distance. The dependence of the spatial resolution on the drift distance is given by (4.33). For muons the resolution was about 50 μm except in the vicinity of the wire.

The ATLAS muon system uses monitored drift tubes (MDTs) for precision tracking of muons from 10 GeV to 1,000 GeV [217]. The MDT chambers are assembled in three nested cylindrical barrel stations and three main coaxial disks in each endcap. A fourth annulus of endcap chambers covers a limited pseudo-rapidity region spanning from the barrel to the endcap. The 354,000 drift tubes are arranged in 1,172 MDT chambers covering an area of 5,000 m^2. They are constructed with pairs of close-packed multilayers of 3 cm diameter cylindrical aluminum drift tubes. Their lengths vary from 1 m for the inner stations close to the beam up to 6 m for the outer stations. Each multilayer comprises of either three or four single planes, depending on the barrel (endcap) chamber radial (z-axis) position. Each plane contains from 12 to 72 tubes. In the center of each tube, a 50 μm diameter gold-plated tungsten-rhenium sense wire is positioned with an accuracy of $<$20 μm. Each tube operates

[17] The project was cancelled in 1993.

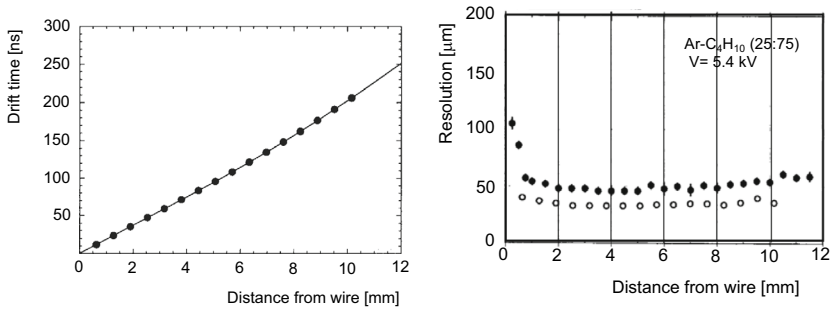

Fig. 4.74 Left: The drift-time-to-drift-distance relation in the drift tube prototype for the GEM detector showing laser data (points) and a fit (solid curve). Right: The spatial resolution as a function of the drift distance from the wire in the drift tube prototype for 500 GeV/c muons (solid points) and laser data (open circles). Both reprinted with kind permission from [216], © 1994, Elsevier. All rights reserved

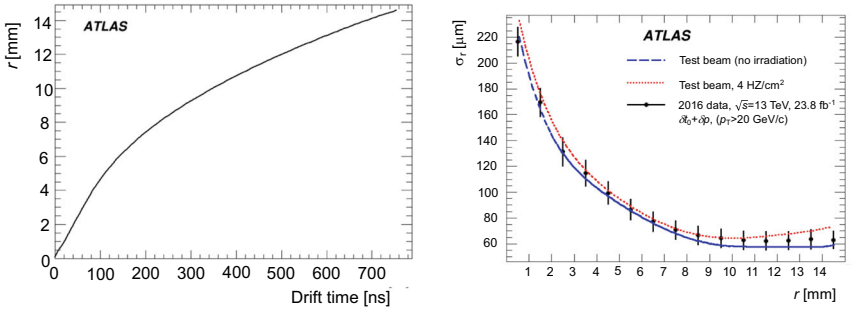

Fig. 4.75 Left: Drift-distance-to-drift-time relation in the ATLAS Monitored Drift Tube. Right: Spatial resolution as a function of drift distance (points with error bars) for the ATLAS MDTs in comparison to that of test beam data before (solid line) and after (dotted line) irradiation. Both reprinted under CC-BY-3.0 Licence from [217], © 2019, ATLAS Collaboration

with an Ar-CO_2 (93:7) gas mixtures at a pressure of 3 bar. The anode wire is at a high voltage of 3.08 kV yielding a gain of 2×10^4.

Figure 4.75 (left) shows the drift-distance-to-drift-time relation, which is not linear but may be approximated by a piecewise linear dependence. The slopes decrease with increasing drift time. Figure 4.75 (right) shows the spatial resolution as a function of the drift distance, which is around 200 μm at 1 mm drift distance from the wire improving to $\sim$60 μm for distances above 9 mm. The average spatial resolution of a single tube in the barrel is $81.7 \pm 0.2_{\text{stat}} \pm 2.2_{\text{sys}}$ μm after time-slewing correction at low background. In the endcap the resolution is 100 μm. At a background rate of 500 Hz/cm^2, the single-tube spatial resolution deteriorates to 104 μm. The tube efficiency is $\sim$100% for nearly the entire track impact radius. The accuracy in momentum measurement is 3% at 100 GeV/c increasing to 10% at 1,000 GeV/c over a pseudo-rapidity range of $|\eta| \leq 2.7$. The dead time is 790 ns.

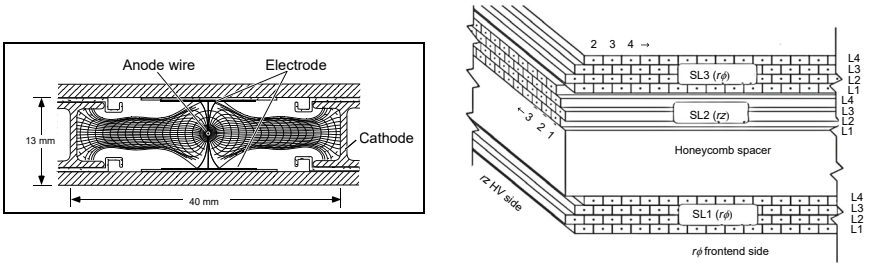

Fig. 4.76 Left: Schematic layout of a CMS drift tube. The electric-field lines and isochrones are also shown. Right: Schematic layout of a CMS drift tube chamber showing three superlayers that consist of four layers each. Superlayer 1 is separated from the other two superlayers by a honeycomb spacer. Both reprinted with kind permission from [220], © 2010, IOP Publishing. All rights reserved

For the high-luminosity upgrade, ATLAS will build new MDTs. The tube diameter is reduced to 15 mm. The chambers operate with the same gas mixture and pressure at 2.73 kV. Each chamber consists of 624 aluminum drift-tubes 2.2 m in length arranged in two multi-layers. Each multilayer is composed of 4 layers with 78 tubes yielding a total width of 1.2 m. Each drift-tube is a multi-component device and must satisfy three requirements. First, the sense wires must be placed in the center of the tube with high precision (better than 20 μm). Second, the wires must be tensioned to 3.5 ± 0.15 N. Third, they must be crimped correctly to the feedthrough.

The CMS experiment uses drift tubes in the muon system in the barrel [221]. The muon barrel consists of five wheels. Each wheel has 12 sectors each covering 30° in azimuth angle. Each sector has four stations equipped with RPCs and drift tubes. In the top and bottom sectors the outer stations are split into two distinct chambers. The drift tubes have a square profile with a cross section of 4 cm $\times$ 1.4 cm. In its center a stainless steel wire 50 μm in diameter is placed. The wire lengths vary between 2 m and 4 m. The cell is made from aluminum I-beams on the sides serving as cathode and aluminum plates on the top and bottom as shown in Fig. 4.76 (left). Copper electrodes are placed on the plates above and below the wire. A drift tube chamber is made of three super layers, each made by four layers of rectangular drift cells staggered by half a cell as shown in Fig. 4.76 (right). The wires in the innermost and outermost superlayers are parallel to the beam line and provide the track measurement in the magnetic bending plane. In superlayer 2, the wires are perpendicular to the beam direction and measure the track position in the z direction. The barrel uses a total of 250 drift tube chambers arranged in four layers containing 172,000 individual cells. The drift tubes are filled with an Ar-CO_2 (85:15) gas mixture. While anode wires are kept at a potential of +3.6 kV, electrodes on the plates are set at +1.8 kV and cathodes are set at –1.2 kV. The single-hit spatial resolution is about 200 μm while resolutions on the segment position and angle in the bending plane are 70 μm and 0.5 mrad, respectively [220].

4.12 Straw Tube Chambers

Straw Tube trackers are similar to drift tube trackers. They are built from straw tubes whose diameters are typically less than 1 cm. A sense wire is placed in its center. Many straws are combined into chambers. Before the era of silicon detectors straw tubes have been used frequently as vertex chambers. Table 4.9 lists properties of straw tube chambers in the HRS, MAC, Mark II, Mark III, AMY and ATLAS experiments. Most of these chambers have 4–6 layers and thin anodes wires of $15 - 30\ \mu m$ diameter. The closest chambers are about 4 cm from the interaction point. The typical gas mixture is argon with ethane. The chambers are very efficient and position resolutions are 50–100 μm. The best resolution is achieved in the MAC chamber yielding 45 μm. The ATLAS transition radiation tracker is somewhat different and will be discussed below after giving some more details about the Mark III straw tube chamber.

Table 4.9 Examples of straw tube chambers used in different experiments as vertex detectors. We show the inner and outer radius r_i, r_o, the wire length ℓ_{wire}, straw tube thickness d_{tube}, sense wire diameter d_w, wire material, number of straws N_{straws}, number of layers N_{layer}, high voltage, gas mixture, gas fraction, gas pressure (P), efficiency and spatial $r\phi$ resolution. [†]PC stands for polycarbonate. [§]The first value refers to wires in layers one and two, while the second refers to wires in layers three and four. [#]The first value refers to the barrel and the second to the endcaps. If only one value is shown it refers to both barrel and endcaps

Experiment	HRS	MAC	Mark II	Mark III	AMY	ATLAS[#]
Reference	[222]	[223]	[224]	[225]	[226]	[180,227]
Material	Al-mylar	Al-mylar	Al-mylar	Al-mylar	Al-PC[†]	Al-polymide
r_i [cm]	9.1	3.56	9.49	5.42	11.8	55.4/61.5
r_o [cm]	11.5	9.04	14.76	13.0	14.7	108.2/110.6
ℓ_{wire} [cm]	40.6–45.7	43.2	75	83.8	57.15	144/37
d_{tube} [mm]	13.82	6.9	8.0	7.8	5.28–5.94	4
d_w [μm]	20	30	20	50	16.3, 15[§]	31
Wire	Au-W	Au-W	Au-W	Au-W	Au-W	Au-W
N_{straw}	352	324	552	640	576	5.044×10^6 4.915×10^6
N_{layers}	4	6	6	12	4	73/160
HV [kV]	1.65	3.9	1.9	3.9	1.75–1.8	1.53
Gas Mixture	Ar-C_2H_6	Ar- CO_2 CH_4	Ar-C_2H_6	Ar-C_2H_6	Ar-C_2H_6	Xe-O_2 -CO_2
Fraction [%]	(75:25)	(49.5:49.5:1)	(50:50)	(50:50)	(50:50)	(70:3:27)
P [atm]	1	4	1	3	1.45	1
Efficiency [%]	92	93.9	93		95–97	96
$\sigma_{r\phi}$ [μm]	100	45	90	49	80	130

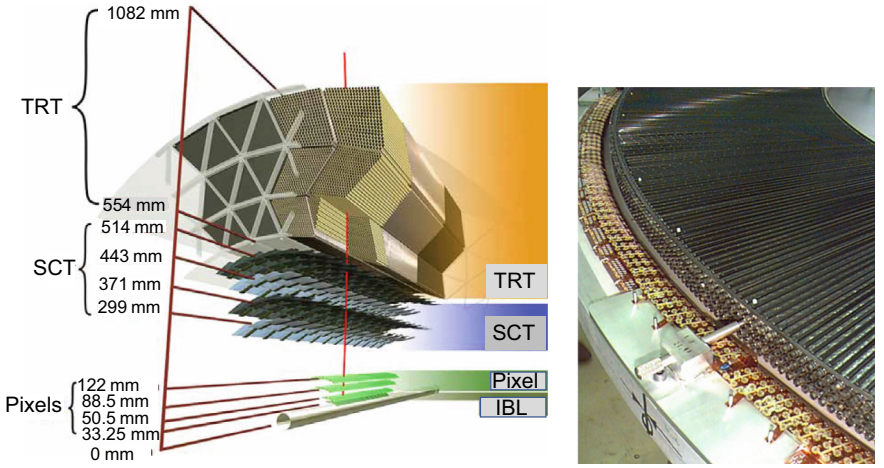

Fig. 4.77 Left: Schematic layout of the ATLAS Inner Detector in the barrel consisting of the Pixel detector, SCT and TRT. Right: Photograph of a four-plane TRT endcap wheel during assembly. Both reprinted with kind permission from [180], © 2008, IOP Publishing. All rights reserved

The Mark III experiment [225], for example, used a 12-layer straw tube array as vertex chamber with eight axial layers and four stereo layers. It was placed at radii between 5.4 cm and 13 cm. The chamber consisted of 640 straws, 8 mm in diameter and 84 cm in length. They were operated with an Ar-C_2H_6 (50:50) gas mixture at 3 atmospheres. The maximum drift distance was 4 mm corresponding to a drift time of 80 ns. The sense wires consisted of gold-plated tungsten wires, 50 μm in diameter. The chambers were operated with a high voltage of 3.9 kV yielding a gain of few $\times\ 10^5$. The chamber worked rather well. The overall spatial resolution was 49 μm, which was close to the spatial resolution of 45 μm achieved by the MAC straw chamber. Note that this is still more than an order of magnitude worse than spatial resolutions achieved with silicon vertex detectors that are discussed in Chap. 6.

The ATLAS Transition Radiation Tracker (TRT) depicted in Fig. 4.77 (left) is a straw-tube tracker, which is used for tracking and for electron identification via transition radiation measurements [180]. The straw tubes are 4 mm in diameter. The walls are wound kapton foils reinforced with thin carbon fibers. In the center of each tube a gold-plated tungsten wire 31 μm in diameter is placed. While sense wires are kept at ground potential, the high voltage (+1.5 kV) is placed on the straw tube walls. The tubes operate with a Xe-CO_2-O_2 (70:27:3) gas mixture. Figure 4.77 (right) shows a photograph of a four-plane TRT endcap wheel during assembly. The TRT barrel contains 5,044,224 straw tubes arranged in 73 layers interleaved with fibers running parallel to the beam axis. They are 156 cm in length and extend from 55.4 cm to 108.2 cm in radial direction covering a pseudo-rapidity range of $|\eta| < 1$. The sense wires are read out on both ends. The endcaps have 0.4 m long straws that run perpendicular to the beam direction covering the pseudo-rapidity range from $0.8 < |\eta| < 2.7$. Each endcap consists of 2,457,600 straw tubes (4 mm in diameter,

31 μm diameter sense wire in the center) arranged in 160 layers, which are read out at the outer end. To use the TRT for tracking, we need to know the t_0 for each straw, which is the offset between the start of the readout and the arrival of particles, and the time-to-distance relation. The latter is modeled well with a third-order polynomial. The measured spatial resolution in $r\phi$ is 110 μm.

4.13 Cathode Strip Chambers

A Cathode Strip Chamber (CSC) is a multi-wire proportional chamber that has cathode strips perpendicular to the beam direction that are read out [39]. However, the CSC technology has some advantages with respect to drift chamber technology, such as performance stability and inherent mechanical precision. Furthermore, low-cost detectors can be produced allowing to cover large areas. Since typically charge is induced on several strips, an excellent spatial resolution is achieved via the center-of-gravity method.

In the CMS muon system each endcap has 270 CSCs arranged on four disks (ME1, ME2, ME3, ME4) [228]. The trapezoidal-shaped chambers come in six different sizes, the largest being 3.4 m $\times$ 1.5 m. They cover an overall area of more than 1,000 m^2. Figure 4.78 (left) shows the layout of a CSC trapezoidal wedge. All chambers have six wire planes interleaved between seven cathode planes. The wires run at approximately constant η with a pitch of 3.2 mm while the precise ϕ measurement is made by radial strips whose widths vary from 2.5 mm at the inner edge to 15.9 mm at the outer edge. Figure 4.78 (top right) shows the avalanche formation near an anode wire coming from a passing muon in the x direction. Charge is induced on the cathode strips that run perpendicular to the anode wires as shown in the y view in Fig. 4.78 (bottom right). The total number of wires exceeds 2.0 million while the number of cathode strips is approximately 235,000. All strips are instrumented, whereas ten wires are ganged together yielding about 235,000 readout channels.

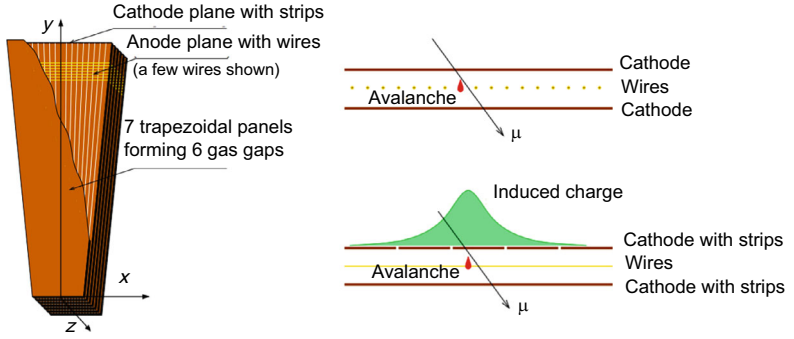

Fig. 4.78 Left: Schematic layout of a CMS cathode strip chamber trapezoidal wedge. Top right: A muon passing through one CSC layer produces an avalanche near the anode wire (x-view). Bottom right: Charge induced on cathode strips (y-view). All reprinted under CC-BY-NC-ND-4.0 Licence from [229], © 2013, B. M. Joshi

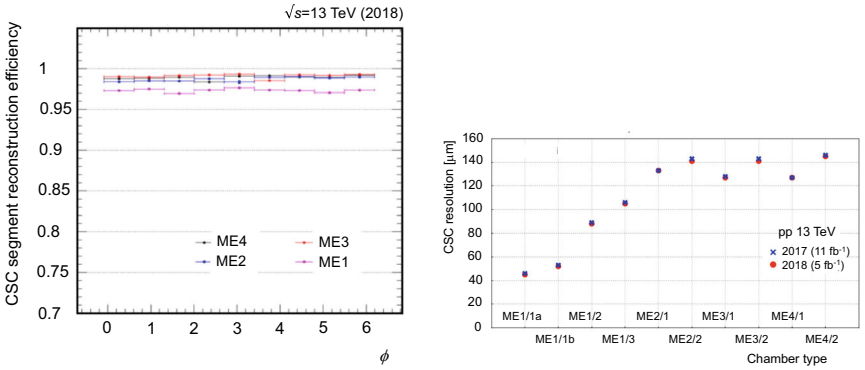

Fig. 4.79 Left: Efficiency of the different cathode strip chamber types in the CMS endcap. The efficiencies have been determined with two different reconstruction algorithms. Right: Spatial resolutions of the CSCs in the four disks in the CMS endcaps. Both reprinted with kind permission from [231], © 2020, IOP Publishing. All rights reserved

The CSCs combine both the precision and trigger functions in one device. They can operate at high rates, in large and non-uniform magnetic fields and require no tight gas, temperature or pressure controls. The chambers are operated with an Ar-CO_2-CF_4 (40:50:10) gas mixture at a high voltage of 3.4 kV. Each chamber has an efficiency >92% providing a track finding efficiency of >99%. Figure 4.79 (left) shows the hit efficiency in the different types of CMS CSCs. The highest efficiency of >98% is obtained with the Road Usage algorithm [230]. Figure 4.79 (right) shows the spatial resolution of the different types of CMS CSCs. In the first disk, the spatial resolutions are around 45 μm increasing to 125-140 μm in disks three and four.

ATLAS uses CSCs in the innermost station of the endcap muon system covering pseudo-rapidities of $2.2 < |\eta| < 2.8$, where particle fluxes are highest [232]. The 32 CSCs are arranged in two rings of eight chambers each. A chamber consists of two identical modules, each having four wire planes. The configuration is equivalent to the one in the MDT system but having finer granularity. The chambers have trapezoidal shape and come in two sizes. The small chambers have a minimum width of 40.3 cm and a maximum width of 73.4 cm with a radial extent of 108.7 cm. The large chambers have dimensions of 61.0 cm, 114.0 cm and 104.0 cm, respectively. The wire pitch is 2.54 mm while the cathode pitch is 5.08 mm. The anode cathode separation is 2.54 mm. The wires are gold-plated tungsten wires with 30 μm diameter. The chambers are operated with an Ar-CO_2-CF_4 (30:50:20) gas mixture at 2.6 kV. The single-point spatial resolution is 60 μm while that of a chamber (four points) is 40 μm. The first pulse of the four planes has a timing resolution of 3.5 ns.

4.14 Thin Gap Chambers

Thin Gap Chambers (TGCs) are also multi-wire chambers consisting of a row of parallel anode wires sandwiched between two cathode planes as shown in Fig. 4.80

(left) [233]. The cathodes are coated with a highly resistive material like graphite. Readout strips or pads are capacitively coupled to the cathodes as depicted in Fig. 4.80 (right). The anode wires are gold-plated tungsten wires with diameters between 20 μm and 100 μm. The anode wire pitch is $\sim$ 2 mm. The anode-cathode gap is 1.0–1.5 mm. Electrons liberated in an ionization process produce a signal on anode wires and induce signals on the readout strips or pads. These chambers have some nice properties. They produces fast signals with a rise time of less than 10 ns and are essentially 100% efficient. Using an operation voltage of 3.5–4.0 kV, they can take particle rates of 300k/cm^2/s. With operation in high multiplication mode the Landau tail becomes small. Thin-Gap Chambers are insensitive to magnetic fields. They can be constructed with high accuracy at moderate costs.

The OPAL experiment used TGCs for electromagnetic presampling in the endcaps [208,236], which consisted of 32 chambers arranged in 16 sectors, where each sector had one large and one small trapezoidal chamber. While the small chamber was perpendicular to the beam, the large chamber was inclined by 18° with respect to the plane perpendicular to the beam. The cathode planes were 200 μm thick G10 sheets covered with resistive carbon paint separated by 3.2 mm. The anode plane in the center consisted of 69 (432) gold-plated tungsten wires 50 μm in diameter spaced by 2 mm for small (large) chambers. The small (large) chamber had 22 (32) strips placed on one G10 outer surface and 10 (16) pads placed on the other G10 outer surface. The chambers ran with a gas mixture of CO_2-C_6H_{12} at a high voltage of 3.5–3.7 kV. For minimum ionizing particles, the intrinsic resolution was 2.17 mm for single wire hits and 4.62 mm for single strip hits. If the charge was shared by two or more wires or strips the spatial resolution improved. For low-momentum tracks, however, the spatial resolution was worsened by a multiple scattering.

The ATLAS experiment uses TGCs in the muon endcaps, which provide two functions: first, to trigger on muons and second to measure the azimuthal coordinate [180,237]. The TGCs are arranged in one doublet layer before the toroid magnet and in three layers consisting of one triplet layer before and two doublet layers behind

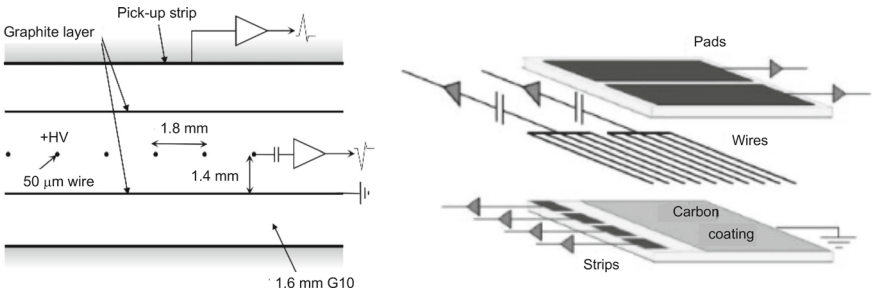

Fig. 4.80 Left: Schematic layout of a thin-gap chamber. Reprinted with kind permission from [234], © 2003, ATLAS Collaboration. All rights reserved. Right: Exploded view of a small thin-gap chamber. Reprinted with kind permission from [235], © 2013, ATLAS Collaboration. All rights reserved

the Big Wheel [238].[18] Each TGC has a trapezoidal shape with a typical size of 1.3 m for the longer base and 1.3 m in height. Each chamber consists of two 1.6 mm thick G-10 plates separated by a 2.8 mm wide gap. The inner walls are coated with graphite. The resistivity is 0.5–2.0 MΩ/square. Individual chambers in a doublet or triplet are separated from each other by a 20 mm honeycomb stiffener. In the center of each chamber, a plane of 50 μm thick gold-plated tungsten anode wires with 1.8 mm pitch is placed that run in the azimuthal direction to measure the radial coordinate. The alignment of sense wires in consecutive layers is staggered to optimize the position resolution and lift the left-right ambiguity. Each sense wire, connected to the high voltage of 2.9 kV, is read out via a decoupling capacitor connected to a preamplifier. Two chambers in a triplet or doublet have 32 copper strips each running along the radial direction to measure the azimuthal coordinate. The gas gap is 2.8 mm. The strip pitch varies between 14.6 mm and 49.1 mm. Anode wires have lengths between 39 cm and 167 cm, while the strip lengths lie between 104 cm and 216 cm. Between 6 and 31 sense wires are grouped together for readout as a function of pseudo-rapidity.

The chambers operate with a CO_2-C_4H_8 (55:45) gas mixture at a pressure of one bar and a high voltage of 2.9 kV. The gas gain is 3×10^5. The highly quenching gas prevents the creation of streamers at high gain. Low-energy neutrons produce pulse heights that are just a factor of 30 above those of minimum ionizing particles. The efficiency is larger than 99%. The long anode wires are supported to reduce sagging. A total of 3,588 TGCs with 318,000 channels is used in the ATLAS detector. The high electric field around the anode wire and the small wire pitch yield good time resolutions of 4 ns. Within a time window of 25 ns more than 99% of the signal is recorded. The spatial resolutions are 2–6 mm in the radial direction and 3–7 mm in the azimuthal direction.

For Run 3, ATLAS has upgraded the Small Wheels in the endcaps [235] with New Small Wheels. Figure 4.81 shows a photograph of a completed New Small Wheel and Fig. 4.82 (left) displays a schematic layout. Each New Small Wheel is made from eight large and eight small pie-shaped sectors. A sector consist of two Micromegas detectors sandwiched between two small-strip Thin Gap Chambers (sTGC) as shown in Fig. 4.82 (right). Each of the four chambers consist of four layers. The cell geometry, electric field and gas mixture are the same as those of the ATLAS TGCs in the endcaps. The cathode planes of inner (outer) chambers consist of a graphite-epoxy mixture with a surface resistivity of 100 (200) kΩ/square that are sprayed onto 100 (200) μm thick G10 sheets. One outer G10 surface is covered with copper strips that run perpendicular to the sense wires while the other outer G10 surface is covered with copper pads that are used for fast trigger purposes. Both, the Cu-strips and Cu-pads are on ground potential and are read out. The strips have a 3.2 mm pitch (2.7 mm strip width 0.5 mm gap) that is much smaller than that of the ATLAS TGCs. The pad size is about 8.7 cm × 8.7 cm. Five anode wires are ganged together for the readout. The four chambers are mounted together in a honeycomb structure. Positioning of the strip planes is required to better than

[18] This is the second tracking station behind the toroid in each endcap consisting of MDTs.

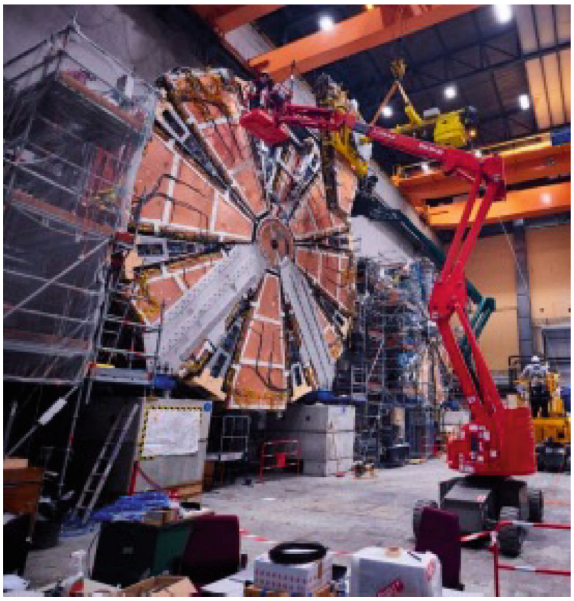

Fig. 4.81 Photograph of an ATLAS New Small Wheel. Reprinted with kind permission from [239], © 2013, ATLAS Collaboration. All rights reserved

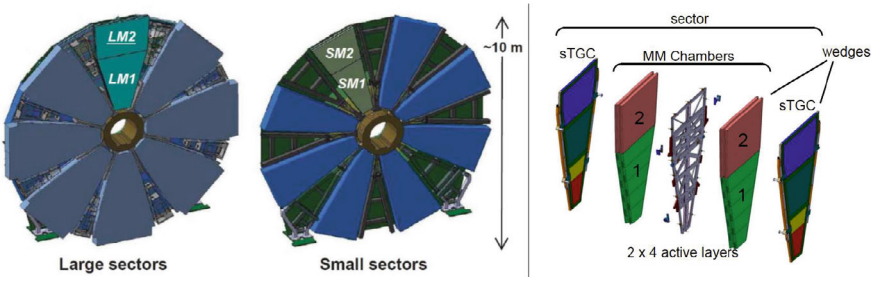

Fig. 4.82 Left: Schematic view of the ATLAS New Small Wheel that is built from large sectors on one side and small sectors on the opposite side. Right: Layout of a New Small Wheel wedge consisting of one four-layer sTGC wedge, two quadruplet Micromegas (MM) and another four-layer sTGC. Both reprinted with kind permission from [240], © 2020, IOP Publishing. All rights reserved

40 μm. The chambers are operated with the same gas mixture and high voltage as the TGCs. Figure 4.83 (left) shows the spatial resolution measured with a four-layer prototype in a CERN test beam with 32 GeV/c pions in six different runs. The average over different runs and layers for perpendicular tracks yields a spatial resolution of $\sigma = 44 \pm 4$ μm. About 95% of all events are contained within a 25 ns time window. Figure 4.83 (right) shows the intrinsic strip spatial resolution of a production module versus the anode high voltage. At the nominal operation voltage of 2.9 kV, a spatial

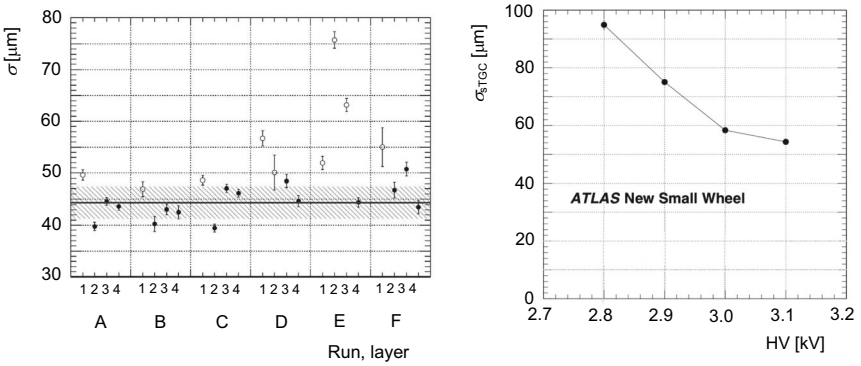

Fig. 4.83 Left: Spatial resolution per layer measured in six different runs in a beam test with a four-layer prototype of sTGCs. The solid points show runs with no expected degradation. The line is a fit to all layers in all runs. Reprinted under CC-BY-4.0 Licence from [241], © 2016, A. Abusleme. Right: Spatial resolution as a function of the anode high voltage for a new Small Wheel production module. Reprinted with kind permission from [240], © 2020, IOP Publishing. All rights reserved

resolution of about 75 μm is measured. Though this is worse than the measured resolutions with the prototype, it is smaller than the design requirement of 100 μm.

4.15 Bubble Chambers

The bubble chamber was invented by Glaser in 1952 [242] for which he was awarded the Nobel Prize in Physics in 1960. A bubble chamber is a volume filled with a liquefied gas with a pressure below but near the boiling point (T_b). After a charged particle passes through the chamber, the volume is expanded to exceed the boiling point. Due to the heat from recombining ions, bubbles are formed along the particle trajectory. A camera takes pictures of the trajectories, which are scanned by people to look for interesting processes. Using high-grain films, resolutions of a few μm were achieved.

At CERN, the Gargamelle bubble chamber was designed to detect neutrino interactions [243]. It operated with 12 m^3 of freon in a muon neutrino beam from 1970 to 1978. In 1973, the discovery of neutral currents was announced shortly after its prediction [244]. In its time of operation, about 83,000 neutrino events were observed of which 102 were neutral-current events. Figure 4.84 (left) shows a photograph of a neutral current interaction, which represents the process $\nu_\mu e^- \rightarrow Z^0 \rightarrow \nu_\mu e^-$. An incoming energetic neutrino interacts with an electron in the atom via a virtual Z^0 boson. The electron is kicked out and radiates photons that are converted into e^+e^- pairs. The neutrino leaves the bubble chamber (on the top of the picture). Gargamelle terminated operation after it developed a crack in 1978. An even larger bubble chamber, the Big European Bubble Chamber (BEBC), started operation inside a 3.5 T superconducting magnet at the Proton Synchrotron in 1973 [245]. In 1977 it was moved to the Super Proton Synchrotron where it operated till 1984. The chamber

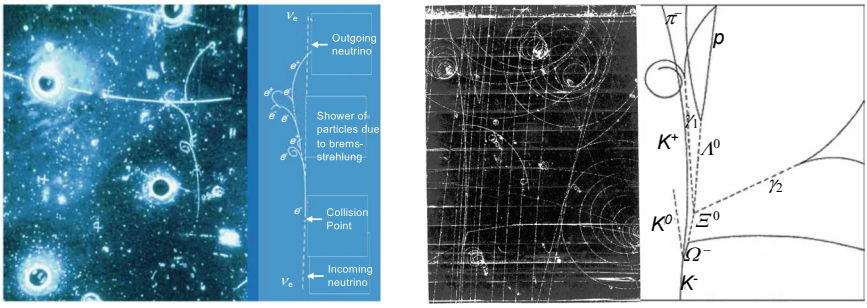

Fig. 4.84 Left: Observation of neutral currents in the Gargamelle bubble chamber showing the photograph on the left-hand side and an interpretation of the particles on the right-hand side [249]. The neutrino enters from the bottom (dashed line). At the collision point an electron is kicked out (solid line). The electron first moves in the direction of the neutrino. It radiates off photons (dotted lines) that convert into e^+e^- pairs. Reprinted with kind permission from [10], © 1992, CERN. All rights reserved. Right: Observation of the Ω^- in the Brookhaven bubble chamber showing the photograph on the left-hand side and an interpretation of the particles on the right-hand side. The Ω^- cascades down via a $\Xi^0\pi^-$, and $\Lambda^0\pi^0$ to a proton and a π^-. Reprinted under CC-BY-NC-ND 3.0 Deed Licence from [250], © 2011, BNL

had a volume of 35 m^3 of hydrogen, deuterium, or hydrogen-neon gas mixture. It produced 6.3 million photographs during its operation.

The 80-inch bubble chamber at Brookhaven discovered the Ω^- baryon in 1964 [246]. This confirmed the approach by Gell-Mann, who classified mesons and baryons into multiplets in the Eightfold Way [247,248]. The Ω^- is a bound state of three strange quarks that had not been seen before. Gell-Mann predicted its quantum numbers including mass, spin and strangeness.[19] So, the discovery was a triumph for the Eightfold Way, marking the beginning of a wider acceptance for the concept of quarks. Figure 4.84 (right) shows a photograph taken by the Brookhaven bubble chamber. The Ω^- was produced in a K^-p interaction. Besides the Ω^-, a K^0 and a K^+ are produced to conserve the strangeness quantum number in strong interactions. The Ω^- then cascades down: $\Omega^- \rightarrow \Xi^0\pi^-$, $\Xi^0 \rightarrow \Lambda\pi^0(\rightarrow 2\gamma)$ and $\Lambda \rightarrow p\pi^-$.

Despite the superb position resolution, the bubble chambers has several disadvantages. The formation of bubbles cannot be read out electronically. One has to rely on photographs, which are two-dimensional. Scanning photographs is time consuming and cannot compete with high-statistics measurements. The procedure is not well-suited to measure short-lived particles, since the super-heated phase must be ready at the right time. The bubble chamber has a considerable deadtime (∼1 ms). Thus, it is not suited to operate at higher rates since the efficiency rapidly drops with an increased event rate. Furthermore, it is not possible to trigger on specific events.

[19] Strangeness is a quantum number that refers to the number of strange quarks in the meson or baryon.

4.16 Other Detectors

In past fixed-target experiments other tracking detectors were used, which include

- Streamer chambers that produce visible streamers along the particle trajectory caused by discharge of the ionized gas [251].
- Spark chambers that produce a discharge of the ionized gas, which is photographed [252,253].
- Flash chambers that produce a large discharge that is recorded [252,254].
- Emulsion detectors using photographic plates that are exchanged and developed from time-to time [255,256].

We will not discuss these detectors in further detail. The interested reader can get more information in older textbooks [257,258]. Except for the emulsion plates, all other detectors listed above are no longer used since it is difficult to read them out electronically, which is important for high efficiencies at high counting rates in multipurpose detectors. Like a bubble chamber, emulsion plates have a very high position resolution determined by the grain size of the plate. A charged particle passing through the emulsion leaves an imprint. Since these detectors cannot be exchanged frequently, they are only used for rare processes. After development of the film, the process becomes visible. The analysis, however, is cumbersome as each plate needs to be inspected visually and may contain more than one event. The development of semiconductor detectors discussed in Chap. 6 have revolutionized the measurement of particle positions.

4.17 Position Resolution of Tracking Detectors

Table 4.10 shows a comparison of spatial resolutions of the different tracking detectors we discussed or we mentioned. Large drift chambers, jet drift chambers and TPCs provide good $r\phi$ resolution of the order of 100 μm. Small drift and jet drift chambers yield $r\phi$ resolutions of 60 μm. Time resolutions depend on the drift length and drift velocity. For $v_{\mathrm{d}}^{e} = 1$ cm/μs, a variation in drift length of 10 μm corresponds to 1 ns. For faster drift velocities, larger drift lengths correspond to 1 ns. Thus, time resolutions are typically a few ns. These detectors were used as tracking detectors. The MWPCs, which also have reasonable spatial resolution, have been used mostly in TPC endcaps, muons systems and TOF counters. Both GEM and Micromegas detectors reach excellent position resolutions. The GEM and MicroMegas detectors are used for tracking in several experiments as well as for the readout of TPCs. Both RPCs and LSTs are mainly used in muon detectors and hadron calorimeters, where excellent spatial resolution is not too important. The poor spatial resolutions measured in different experiments are due to large strip and pad pitches to save readout electronics. In the ATLAS experiment for example, RPCs are used to trigger on muons. So excellent spatial resolution is not relevant but time resolution is important, which is of the order of 1 ns. Other trigger chambers are TGCs, whose

Table 4.10 Comparison of average position resolutions in tracking detectors. [§]Resolution for cylindrical detectors is typically in $r\phi$ and z while for planar detectors it is in x and y. [†]Value in parentheses is from SLD. [⋆]This depends on the gas mixture; spatial resolutions of 11 μm were achieved with a CF_4-iC4H_{10} (80:20) gas mixture at $|\vec{E}| = 2.7$ kV/cm in a prototype. [‡]Here the resolutions are for ϕ and η

Detector	$\sigma_{r\phi}$ or σ_x [μm][§]	σ_z or σ_y [μm][§]	reference
Small MWPC	150	35–45	[41]
Planar MWPC	150 – 300	150 – 300	[27]
Cylindrical MWPC	179	440	[27,32]
Small DC	60	60	[60]
Planar DC	55–250	160	[61,63]
Cylindrical DC	90–150	100–150	[74,77]
Jet DC	135–170	0.6–1% $\cdot \ell_{wire}$	[90,92]
Small Jet DC	40–55	1% $\cdot \ell_{wire}$	[87,98]
Mini-jet vertex chamber	20–25	35 (at 560 kV/cm)	[99]
TPC	150–180	160–900	[36,100,110]
GEM	70	70	[131,259]
Micromegas	70–110 (11–14)[⋆]	–	[153,158,260]
RPC	2,000–11,000	2,000–11,000	[180]
LST	2,300- 5,000	900–11,000	[208,212]
MDT	70–200	–	[180]
Straw chamber	45–130	–	[222,223]
CSC[‡]	40–140		[180]
TGC	2,000–6,000	3,000–7,000	[180]
sTGC	44, 75		[240]
Bubble chamber	Few	–	[242,261]
Emulsion	1	1	[255,256]
Si strip	2–7	Few	[262]
Si pixel	2	2	[262]

spatial resolution is quite large as well. For the ATLAS run 3, upgrade of the new Small Wheel new sTGCs providing triggers also yield excellent spatial resolution. Both, drift tubes and CGCs provide excellent spatial resolution and are used for precise muon tracking. Despite their excellent spatial resolution, Bubble chambers have been phased out since they cannot be read out electronically and they are too slow to record short-lived particles. Similarly, streamer chambers, flash chambers and spark chambers are no longer in use since they are not competitive as well. Emulsions have been used in neutrino experiments because of their excellent spatial resolution. Since event rates are low due to the small neutrino cross section, the exchange of the photographic plates on a few days basis was fine. With the development of solid-state detectors spatial resolution were improved drastically, so that secondary vertices could be reconstructed. It first started with silicon strip sensors. Then due to increased occupancies, silicon pixel sensor were produced. We discuss these detectors in great detail in Chap. 6.

Exercises

4.1 Consider a big MWPC, which has one plane of wires in the x-direction, spaced every 3 mm. The distance to the frame is also 3 mm. The wires have a diameter of 25 μm. The wires are tensioned such that sagging may be ignored. After charged particles have passed through the detector, you observe the following patterns of charges: a) 11 μC on wire 9, 72 μC on wire 10 and 20 μC on wire 11; b) 51 μC on wire 10; c) 43 μC on wire 9 and 59 μC on wire 10. Determine the y-coordinates of the passing tracks and their uncertainties. Assume that the noise contribution is 1 μC. Hint: to determine the uncertainties on the charge measurements, assume that the MWPC has a gain of 10^7 and that the signal is further amplified in a shaping amplifier with a gain of 3×10^4. What systematic errors have we ignored?

4.2 Consider the same chamber as in problem 4.1. To measure the x coordinate, you instrument both sides of the wires. On side A you see charges of 42 μC and 60 μC for wires 9 and 10. On side B you see 28 μC and 24 μC, respectively. Determine the x position and its uncertainty.

4.3 Determine the RMS of a box distribution with width Δz. In silicon strip detectors one measures the position of particle tracks. Assume a detector that has an array of parallel strips; each strip is 40 μm wide and is separated from its neighbor by 10 μm. If only one strip records a signal, what position resolution do you measure?

4.4 a) Determine the electron drift velocity in Ar gas under normal conditions. There is an electric field present along the y-direction with $\vec{E} = (0, E_y, 0)$ and $E_y = 1$ kV/cm as well as a magnetic field along the z-direction with $\vec{B} = (0, 0, B_z)$ and $B_z = 1\ T$. The time between collisions is about 5 ps. How big is the Lorentz angle in degrees? What can I do to reduce the Lorentz angle? b) Change the electric field such that it only has a z component $\vec{E} = (0, 0, E_z)$. Determine the drift velocity and Lorentz angle in this case?

4.5 A drift chamber filled with Ar gas sits in a magnetic field of 1.5 T. The electrons need to drift a distance of 15 cm with a constant velocity of 2.2 cm/μs. The electrons collide with the gas atoms every 10^{-11} s. The mean free path is 5.66×10^{-5} cm. The electric field is parallel to the magnetic field. What is the expected position resolution? What resolution do you obtain if you switch off the magnetic field?

4.6 Consider a cylindrical straw chamber with a radius of $r_a = 1$ cm filled with Ar gas at normal conditions. In the center a 50 μm thick wire is positioned. Electric fields of +100 V/cm and +10 kV/cm are applied to the wire. Signals recorded on the wire are read out. Assume that an e-ion pair is produced at a position $r_0 = 0.5r_a$, where r_a is the radius of the straw. If the electron would not loose any energy by collisions what would the maximal kinetic energy be for the two field configurations when it hits the wire. The observed pulse has an electron and an ion contribution. What are the relative contributions from electrons and ions for the two field configurations?

4.7 Consider an MWPC with $a_w = 6$ mm, $d_w = 10$ μm and $s_w = 2$ mm. The chamber operates with a gain of 10^6. The wire diameter is known to 2%, the anode cathode gap has an uncertainty of 80 μm and the wire spacing is precise to 50 μm. What are the uncertainties on the gain?

4.8 The endplates of a TPC are instrumented with MWPCs. The chambers are operated with an Ar $-$ CH_4 (90:10) gas mixture at NTP in a 1.5 T solenoidal magnetic field. The electric field is 125V/cm. What is the drift velocity? After 1 m drift how big is the transverse diffusion with and without the magnetic field?

4.9 A GEM detector uses 50 μm thick Kapton sheets with 80 μm holes separated with a pitch of 140 μm. The detector is operated with pure argon gas at NTP. The electric field across the hole is $|\vec{E}| = 80$ kV/cm. How large is the first Townsend coefficient and how large is the amplification? How do your results compare to the measurement shown in Fig. 4.51?

4.10 Consider a limited streamer tube that is operated in an Ar-isobutane (25:75) gas mixture. The sense wires are 100 μm in diameter. The threshold voltage is $V_{ts} = 4.25$ kV. The slope is 70 pC/kV. What charge will be measured at operating voltages of 4.5 kV and 4.9 kV? For 50 μm diameter sense wires the threshold voltage is reduced to 3.55 kV. What charge will be measured at 4.0 kV? The chamber may be operated also in the proportional mode. For the 100 μm wire the threshold voltage is $V_{tp} = 3.5$ kV. What charge will be measured at 4.5 kV? The initial charge is 0.4 pC and the constant is $\kappa_p = 16$. Compare the charge measurements at 4.0 kV for the two modes of operation.

References

1. C.T.R. Wilson, Proc. Roy. Soc. Lond. A **87**-595, 277 (1912)
2. C.D. Anderson, Science **76**, 238 (1932)

3. C.D. Anderson, S.H. Neddermeyer, Phys. Rev. **50**, 263 (1936)
4. G.D. Rochester, C.C. Butler, Nature **160**, 855 (1947)
5. V.A. Mikhailov, V.N. Roinishvili, AEC-TR-5417 (1962)
6. G.E. Chikovani et al., Phys. Lett. **6**, 254 (1963)
7. M. Conversi, A. Gozzini, Nuo. Cim. **2**, 189 (1955)
8. M. Conversi, L. Federici, Nucl. Instrum. Meth. **151**, 93 (1978)
9. G. Charpak et al., Nucl. Instrum. Meth. **62**, 262 (1968)
10. G. Charpak, https://physicsmasterclasses.org/exercises/hands-on-cern/hoc_v21en/
11. S.K. Mitra, SLAC **108** UC-37 (1969)
12. F. Sauli, *Gaseous radiation detectors* (Cambridge University Press, Cambridge, UK, 2014)
13. G. Charpak, D. Rahm, H. Steiner, Nucl. Instrum. Meth. **80**, 13 (1970)
14. P. Morse, H. Feshbach, *Methods of theoretical Physics* (Mc Graw Hill, New York, 1953)
15. H. Buchholz, *Elektrische und magnetische Potentialfelder* (Springer, Berlin, 1957)
16. G.A. Erskine, Nucl. Instrum. Meth. **105**, 565 (1972)
17. F. Sauli, CERN report CERN **77**-09, 1 (1977)
18. H.G. Fischer et al., *Proc (Int* (Dubna, JINR report D, Meeting on Proportional and Drift Chambers, 1975), pp.13–9164
19. G. Charpak, Ann. Rev. Nuclear Sci. **20**, 195 (1970)
20. M. Breidenbach, F. Sauli, R. Tirler, Nucl. Instrum. Meth. **108**, 23 (1973)
21. L.E. Price, Nucl. Instrum. Meth. **112**, 507 (1973)
22. G. Charpak et al., Nucl. Instrum. Meth. **97**, 377 (1971)
23. R. Bouclier et al., Nucl. Instrum. Meth. **88** (1970) 149. Nucl. Instrum. Meth. **88**, 149 (1970)
24. P. Schilly et al., Nucl. Instrum. Meth. **91**, 221 (1971)
25. C. Trippe, CERN NP Internal Report **69**-18 (1969)
26. R. Bouclier et al., Nucl. Instrum. Meth. **115**, 235 (1974)
27. G. Aiken et al., SLAC-PUB-**2642**, (1980)
28. The LHCb Collaboration (A. Augusto Alves et al., JINST **3**, S08005 (2008)
29. M. de Palma et al., Nucl. Instrum. Meth. **217**, 135 (1983)
30. S. Özkorucuklu, SELEX experiment, FERMILAB-THESIS-2000-33 (2001)
31. K. Ackerstaff et al., Nucl. Instrum. Meth. A **417**, 230 (1998)
32. H.J. Behrend, Comp. Phys. Comm. **22**, 365 (1981); The Cello Collaboration (M. J. Schachter et al.), Phys. Scripta **23**, 610 (1981)
33. D. Bloch et al., Nucl. Instrum. Meth. A **273**, 847 (1988)
34. The ALICE Collaboration (A. Gallas et al.), Nucl. Instrum. Meth. A **581**, 402 (2007)
35. The ALEPH Collaboration (D. Decamp et al.), Nucl. Instrum. Meth. A **294**, 121 (1990)
36. C. Brand et al., Nucl. Instrum. Meth. A **283**, 567 (1989)
37. The ALICE Collaboration (A. di Mauro et al.), Nucl. Instrum. Meth. A **433**, 190 (1999)
38. A. Breskin et al., Nucl. Instrum. Meth. **143**, 29 (1977)
39. G. Charpak et al., Nucl. Instrum. Meth. **167**, 455 (1979)
40. M. Atac et al., Nucl. Instrum. Meth. **176**, 1 (1980)
41. G. Charpak et al., Nucl. Instrum. Meth. **148**, 471 (1978)
42. F. Sauli, LBNL Symposium, Berkeley, May2-3 (2014)
43. R. Turchetta, Nucl. Instrum. Meth. **335**, 44 (1993)
44. The LASS Collaboration (D. Aston et al.), SLAC-0298 (1987)
45. The LHCb TDR, CERN-LHCC-2003-030 (2003); A.A. Alves Jr. et al., arXiv:1211.1346v2 [physics.ins-det] (2013)
46. A. Andreev et al., Nucl. Instrum. Meth. A **465**, 482 (2001)
47. J. Va'vra, Wire Aging, talk at DESY workshop, https://desy.de/~agingw/trans/ps/vavra.pdf (2003)
48. O. Ullaland, The OMEGA and SFMD experience in intense beams, talk at the Workshop on Radiation Damage to Wire Chambers. LBL- **21170**, 107 (1986)
49. I. Juricic, LBL- **21170**, 141 (1986)
50. M. Binkley et al., Nucl. Instrum. Meth. A **515**, 53 (2003)
51. L. Malter, Phys. Rev. **50**, 48 (1936)

52. F. Sauli, talk on Gas Detectors, KEK, March 14, (2009)
53. R. Openshaw et al., Nucl. Instrum. Meth. A **307**, 298 (1991)
54. G.S. Oehrlein et al., J. Vac. Sci. Tech. A **12**, 333 (1994)
55. A.H. Walenta, J. Heintze, B. Schürlein, Nucl. Instrum. Meth. **92**, 373 (1971)
56. The Particle Data Group (S. Navas et al.), Phys. Rev D. **110**, 030001 (2024)
57. A. Breskin et al., Nucl. Instrum. Meth. **124**, 189 (1975)
58. G. Marel et al., Nucl. Instrum. Meth. **141**, 43 (1977)
59. M. Holder et al., Nucl. Instrum. Meth. **148**, 235 (1977)
60. D. Bettoni et al., Nucl. Instrum. Meth. A **252**, 272 (1986)
61. B. Adeva et al., Nucl. Instrum. Meth. A **289**, 35 (1990)
62. Y. Peng, Report RX-1231, AMSTERDAM (1988)
63. The H1 Collaboration (I. Abt et al.), Nucl. Instrum. Meth. A **386**, 348 (1997); DESY-93-103 (1993)
64. J.M. Bailey, Nucl. Instrum. Meth. A **323**, 184 (192)
65. The H1 Collaboration (I. Abt et al.), DESY-93-103 (1993)
66. P.J. Laycock et al., JINST **7**, T08003 (2012)
67. H. Grässler et al., Nucl. Instrum. Meth. A **283**, 459 (1989)
68. W. Farr et al., Nucl. Instrum. Meth. **154**, 175 (1978)
69. D. Bernstein et al., Nucl. Instrum. Meth. A **226**, 301 (1984)
70. J. Roehrig et al., Nucl. Instrum. Meth. A **226**, 319 (1984)
71. The TASSO Collaboration (R. Brandelik et al.), Phys. Lett. B **83**, 261 (1979)
72. H. Boerner et al., Nucl. Instrum. Meth. **176**, 151 (1980)
73. The ARGUS Collaboration (H. Albrecht et al.), Nucl. Instrum. Meth. A **275**, 1 (1989)
74. SLD Design Report, SLAC **273** (1985)
75. J. Fero et al., Nucl. Instrum. Meth. A **367**, 111 (1995)
76. The CLEO II Collaboration (Y. Kubota et al.), Nucl. Instrum. Meth. A **320**, 66 (1992)
77. The BABAR Collaboration (B. Aubert et al.), Nucl. Instrum. Meth. A **479**, 1 (2002)
78. BABAR Collaboration (B. Aubert et al.), Nucl. Instrum. Meth. A **729**, 615 (2013)
79. The Belle II Collaboration (T. Abe et al.), Belle II TDR arXiv:1011.0352, (2010); (N. Taniguchi et al.), JINST **12**-06, C06014 (2017)
80. T.V. Dong et al., Nucl. Instrum. Meth. A **930**, 132 (2019)
81. The CDF Collaboration (A. Affolder et al.), Nucl. Instrum. Meth. A **526**, 249 (2003)
82. T. LeCompte and H. T. Diehl, Ann. Rev. Nucl. Part. Sci. **50**, 71 (2000); R. Blair et al., Technical Design Report, FERMILAB-PUB-96-390-E (1996)
83. W.D. Li et al., Int. J. Mod. Phys. A **24**-S1, 9 (2009)
84. M. Moritsu et al., PoS EPS-HEP **2019**, 128 (2020)
85. G.F. Tassielli et al., JINST **15**-09, C09051 (2020)
86. M. Hauschild, https://indico.cern.ch/event/996326/contributions/4200962/attachments/2191650/3704305/dEdx.pdf (2021)
87. W. Blum, L. Rolandi, *Particle Detection with Drift Chambers* (Springer Verlag, Berlin, 1994)
88. The BABAR Collaboration (G. Sciolla et al.), Nucl. Instrum. Meth. A **419**, 310 (1998)
89. The BABAR Collaboration (B. Aubert et al.), BABAR photos SLAC (2000); https://phas.ubc.ca/~hearty/BaBar-photos/BaBar-photos.html;
90. The JADE Collaboration (H. Drumm et al.), Nucl. Instrum. Meth. **176**, 333 (1980)
91. G. Abrams et al., Nucl. Instrum. Meth. A **281**-7, 55 (1989)
92. J. Bürger et al., Nucl. Instrum. Meth. A **279**, 217 (1989)
93. H.M. Fischer et al., Nucl. Instrum. Meth. A **283**, 492 (1989)
94. O. Biebel et al., Nucl. Instrum. Meth. A **323**, 169 (1992)
95. J. Heintze, Nucl. Instrum. Meth. A **196**, 293 (1982)
96. G. Hanson et al., Nucl. Instrum. Meth. A **252**, 343 (1986)
97. R.D. Heuer, A. Wagner, Nucl. Instrum. Meth. A **265**, 11 (1988)
98. J.P. Alexander et al., Nucl. Instrum. Meth. A **283**, 519 (1989)
99. M. Roney, Nucl. Instrum. Meth. A **279**, 236 (1989)

100. D. R. Nygren and J. N. Marx, Phys. Today **31**-N10 (1978); H. Aihara et al., IEEE Trans. Nucl. Scienc. NS-**30**, No. 1 (1983)
101. D. Fancher et al., Nucl. Instrum. Meth. **161**, 383 (1979)
102. P. Christiansen, The ALICE Time Projection Chamber, lecture at Lund University, https://www.hep.lu.se/staff/christiansen/teaching/spring_2013/the_alice_tpc.pdf (2013)
103. S.R. Amendolia et al., Nucl. Instrum. Meth. A **239**, 192 (1985)
104. The TOPAZ TPC Group (T. Kamae et al.), Nucl. Instrum. Meth. A **252**, 423 (1986)
105. R. Itoh et al., IEEE Trans. Nucl. Sci. **34**, 533 (1987)
106. A. Shirahashi et al., IEEE Trans. Nucl. Sci. **35**, 1 (1988); K. Fujii et al., Nucl. Instrum. Meth. A **264**, 297 (1988)
107. W. Blum, Nucl. Instrum. Meth. A **225**, 557 (1984)
108. W.B. Atwood et al., Nucl. Instrum. Meth. A **306**, 446 (1991)
109. The ALEPH Collaboration (D. Buskulic et al.), Nucl. Instrum. Meth. A **360**, 481 (1995)
110. J. Alme et al., Nucl. Instrum. Meth. A **622**, 316 (2010)
111. The XENON1T Collaboration, https://xenonexperiment.org/
112. The LZ Collaboration (D. S. Akerib et al.), Nucl. Instrum. Meth. A **953**, 163047 (2019)
113. The DUNE Collaboration (A. Falcone et al.), Nucl. Instrum. Meth. A **1041**, 167216 (2022)
114. ALEPH photographs, https://aleph.web.cern.ch/aleph/aleph/newpub/detector.html (1989)
115. The ALICE TPC Collaboration (M. M. Aggarwal et al.), Nucl. Instrum. Meth. A **903**, 215 (2018)
116. H.J. Hilke, Rep. Prog. Phys. **73**, 116201 (2010)
117. J. Alme et al., Nucl. Instrum. Meth. A **622**, 316 (2010)
118. A. Oed, Nucl. Instrum. Meth. A **263**, 351 (1988)
119. The ALEPH Collaboration, https://aleph.web.cern.ch/aleph/dali/normal/dc015768_005906_960307_1622.gif_3jet (1996)
120. T. Francke and V. Peskov, Innovative Applications and Developments of Micro-Pattern Gaseous Detectors, IGI Global (2004)
121. L. Alunni et al., Nucl. Instrum. Meth. A **348**, 344 (1994)
122. F. Angelini et al., Nucl. Instrum. Meth. A **360**, 22 (1995)
123. R. Bouclier, Nucl. Instrum. Meth. A **332**, 100 (1993)
124. F. Sauli, Nucl. Instrum. Meth. A **805**, 2 (2016)
125. C. Altunbasa et al., Nucl. Instrum. Meth. A **490**, 177 (2002)
126. F. Sauli, Nucl. Instrum. Meth. A **386**, 531 (1997)
127. Cern Courier, Micropattern detectors promise a big future, March issue, p15 (2001)
128. A. Buzulutskov et al., Nucl. Instrum. Meth. A **433**, 471 (1999)
129. J. Benlloch et al., CERN-PPE/97-146 (1997)
130. C. Altunbas et al., Nucl. Instrum. Meth. A **490**, 177 (2002)
131. B. Ketzer et al., Nucl. Instrum. Meth. A **535**, 314 (2004)
132. G. Anelli et al., JINST **3**, S08007 (2008)
133. S. Lami et al., Nucl. Phys. Proc. Suppl. **172**, 231 (2007)
134. The CMS Muon Group (M. Abbas et al.), JINST **15**-10, P10013 (2020)
135. M. Alfonsi et al., Nucl. Instrum. Meth. A **518**, 106 (2004)
136. A. Bondar et al., Nucl. Instrum. Meth. A **496**, 325 (2003)
137. The ALICE Collaboration (D. Miśkowiec et al.), J. Phys. Conf. Ser. **1561**- 1, 012017 (2020)
138. H. Fenker et al., Nucl. Instrum. Meth. A **592**, 273 (2008)
139. A. Balla et al., Nucl. Instrum. Meth. A **732**, 221 (2013)
140. F. Archilli et al., JINST **8**, P02022 (2013)
141. M. Alfonsi et al., Nucl. Instrum. Meth. A **581**, 283 (2007)
142. The CMS Collaboration (M. Bianco et al.), JINST **15**, C09045 (2020)
143. Y. Giomataris et al., Nucl. Instrum. Meth. A **376**, 29 (1996)
144. G. Charpak et al., Nucl. Instrum. Meth. A **478**, 26 (2002)
145. M.I. Ismail, Journal of Applied Electrochemestry **9**, 407 (1979)
146. I. Giomataris et al., Nucl. Instrum. Meth. A **560**, 405 (2006)
147. P. Colas, I. Giomatarisa, V. Lepeltier, Nucl. Instrum. Meth. A **535**, 226 (2004)

148. F. Kuger, Nucl. Instrum. Meth. A **845**, 248 (2017)
149. G. Barouch et al., Nucl. Instrum. Meth. A **423**, 32 (1999)
150. M. Titov, arXiv:1308.3047 [physics.ins-det] (2013)
151. A. Delbart et al., Nucl. Instrum. Meth. A **478**, 205 (2002)
152. C. Jesus-Valls, JINST **15**-08, C08016 (2020)
153. J. Derré et al., Nucl. Instrum. Meth. A **459**, 523 (2001)
154. Y. Giomataris et al., Nucl. Instrum. Meth. A **419**, 239 (1998)
155. F. Thibaud et al., JINST **9**, C02005 (2014)
156. The COMPASS Collaboration (D. Thers et al.), Nucl. Instrum. Meth. A **469**, 133 (2001)
157. F. Kunne et al., Nucl. Phys. A **721**, 1087 (2003)
158. C. Bernet et al., Nucl. Instrum. Meth. A **536**, 61 (2004)
159. The T2K TPC Collaboration (N. Abgrall et al.), Nucl. Instrum. Meth. A **637**, 25 (2010)
160. The T2K TPC Collaboration (J. Beucher et al.), NSS/MIC 2008 / RTSD 2008, 3384 (2008)
161. C. Adloff et al., J. Phys. Conf. Ser. **293**, 012078 (2011)
162. C. Adloff et al., Nucl. Instrum. Meth. **763**, 221 (2014)
163. I. Manthos et al., AIP Conf. Proc. **2075**-1, 080010 (2019). (arXiv:1901.03160 [phys.ins.det] (2021))
164. D. Neyret et al., JINST **7**, C03006 (2012)
165. A. Delbart et al., J. Phys. Conf. Ser. **308**, 012017 (2011)
166. R. de Oliveira, MicroPattern Gaseous Detectors, talk at TIPP2023, https://indico.tlabs.ac.za/event/112/contributions/3303/attachments/1158/1568/TIPP%202023.pdf (2023)
167. The COMPASS Collaboration (F. Gautheron et al.), COMPASS II Proposal, SPSC-P-340, CERN-SPSC-2010-014 (2010)
168. R. Santonico, R. Cardarelli, Nucl. Instrum. Meth. A **187**, 377 (1981)
169. F. Anulli et al., Nucl. Instrum. Meth. A **515**, 322 (2003)
170. P. Kumari et al., JINST **15**-11, C11012 (2020)
171. The CMS Collaboration (S. Chatrchyan et al.), JINST **3**, S08004 (2008)
172. The ALICE Collaboration (K. Aamodt et al.), JINST **3**, S08002 (2008)
173. V. Ammosov et al., Nucl. Instrum. Meth. A **533**, 130 (2004)
174. G. Drake et al., Int. J. Mod. Phys. A **20**, 3830 (2005)
175. F. Anulli et al., Nucl. Instrum. Meth. A **539**, 155 (2005); Nucl. Instrum. Meth. A **552**, 275 (2005)
176. The Belle Collaboration (A. Abashian et al.), Nucl. Instrum. Meth. A **479**, 117 (2002)
177. A. Abashian et al., Nucl. Instrum. Meth. A **449**, 112 (2000)
178. R. Arnaldi et al., Nucl. Instrum. Meth. A **490**, 51 (2002); M. Gagliardi et al., Nucl. Instrum. Meth. A **661**, S45 (2012)
179. A. Ferretti, JINST **14**-06, C06011 (2018)
180. The ATLAS Collaboration (G. Aad et al.), JINST **3**, S08003 (2008)
181. The ATLAS Collaboration (G. Aad et al.), JINST **15**-09, P09015 (2020)
182. M. Sessa, PoS EPS-HEP2021, 750 (2022); The ATLAS Collaboration (G. Aad et al.), JINST **16**-07, P07029 (2021)
183. The CMS Collaboration (P. Paolucci et al.), JINST **8**, P04005 (2012); ibid (S. Chatrchyan et al.), JINST **5**, T03017 (2010)
184. The ALICE Collaboration (N. Jacazio et al.), PoS LHCP2018, 232 (2018); A. Alici, Nuovo Cim. C **027**, 403 (2004)
185. A.N. Akindinov et al., Nucl. Instrum. Meth. A **533**, 178 (2004)
186. The PHENIX Collaboration (K. Adcox et al.), Nucl. Instrum. Meth. A **499**, 469 (2003)
187. The FOPI Collaboration (J. Ritman et al.), Nucl. Phys. B Proc. Suppl. **44**, 708 (1995)
188. The HADES Collaboration (K. Zeitelhack et al.), Nucl. Instrum. Meth. A **433**, 201 (1999)
189. The HARP Collaboration (M. H. Catanesi et al.), Nucl. Instrum. Meth. A **571**, 527 (2007)
190. ARGO-YBJ Collaboration (B. Bartoli et al.), Astropart. Phys. **67**, 47 (2015)
191. A. Bertolin et al., Nucl. Instrum. Meth. A **602**, 631 (2009)
192. The ATLAS Collaboration (O. Kortner et al.), JINST **16**-06, C06001 (2021)
193. F. Anulli et al., Nucl. Instrum. Meth. A **508**, 128 (2003)

194. J.G. Wang et al., Nucl. Instrum. Meth. A **508**, 133 (2003)
195. G. Battistoni et al., Nucl. Instrum. Meth. **164**, 57 (1979)
196. R. Kass, talk on Key LST Project goals OSU (2003)
197. W. Menges, SLAC-PUB-12080 (2005)
198. B. Fulsom, SLAC graduate student seminar, SLAC (2005)
199. M. Atac, Nucl. Instrum. Meth. A **200**, 345 (1982)
200. F. Taylor, Nucl. Instrum. Meth. **289**, 283 (1989)
201. A.V. Benvenuti et al., Nucl. Instrum. Meth. A **290**, 353 (1989)
202. L.S. Osborne, eConf C **851031**, 026 (1985)
203. Y. Kamyshkov et al., Nucl. Instrum. Meth. A **257**, 125 (1987)
204. G. D'Agostini et al., Nucl. Instrum. Meth. A **252**, 431 (1986)
205. S. Bhadra et al., Nucl. Instrum. Meth. A **268**, 92 (1987)
206. G. Cibinetto et al., Int. J. Mod. Phys. A **20**, 3834 (2005)
207. G. Artusi et al., Nucl. Instrum. Meth. A **279**, 523 (1989); G. T. J. Arnison et al., Nucl. Instrum. Meth. A **94**, 431 (1990);
208. The OPAL Collaboration (K. Ahmet et al.), Nucl. Instrum. Meth. A **305**, 275 (1991)
209. The DELPHI Collaboration (P. Aarnio et al.), Nucl. Instrum. Meth. A **303**, 233 (1991)
210. I. Ajinenko et al., IEEE Trans. Nucl. Sci. **43**, 1751 (1996)
211. I. Kudla et al., Nucl. Instrum. Meth. A **300**, 480 (1991)
212. G. Abbiendi et al., Nucl. Instrum. Meth. A **333**, 342 (1993)
213. The H1 Collaboration (I. Abt et al.), Nucl. Instrum. Meth. A **386**, 348 (1997)
214. The MACRO Collaboration (M. Ambrosio et al.), Nucl. Instrum. Meth. A **486**, 663 (2002)
215. The MACRO Collaboration (S. Ahlen et al.), Nucl. Instrum. Meth. A **324**, 337 (1993); The MACRO Collaboration (M. Ambrosio et al.), Astropart. Phys. **7**, 109 (1997)
216. A. Korytov et al., Nucl. Instrum. Meth. A **338**, 375 (1994)
217. The ATLAS Collaboration (G. Aad et al.), JINST **14**-09, P09011 (2019)
218. M. Andreotti, SLAC-PUB-12205 (2005)
219. C. Adorisio et al., Nucl. Instrum. Meth. A **575**, 532 (2007)
220. The CMS Collaboration (S. Chatrchyan et al.), JINST **5**, T03016 (2010)
221. The CMS Collaboration (G. L. Bayatian et al.), CMS TDR, CERN/LHCC **7**-32 (1997)
222. P.S. Bahringer et al., Nucl. Instrum. Meth. A **254**, 542 (1987)
223. W.W. Ash et al., Nucl. Instrum. Meth. A **261**, 399 (1987)
224. W.T. Ford et al., Nucl. Instrum. Meth. A **255**, 486 (1987)
225. J. Adler et al., Nucl. Instrum. Meth. A **276**, 42 (1989)
226. M. Frautschi et al., Nucl. Instrum. Meth. A **307**, 52 (1991)
227. The ATLAS Collaboration (M. Aaboud et al.), JINST **12**, P05002 (2017)
228. D. Acosta et al., Nucl. Instrum. Meth. A **453**, 182 (2000)
229. The CMS Muon Group (B. M. Joshi et al.), PoS LHCP2018, 074 (2018)
230. M. Paneva, EPJ Web of Conferences **214**, 02014 (2019)
231. N. Manganelli, JINST **15**, C03047 (2020)
232. The ATLAS Collaboration (G. Aad et al.), ATLAS muon spectrometer: Technical Design Report, LHCC-**97**-22 (1997)
233. S. Majewski et al., Nucl. Instrum. Meth. A **217**, 265 (1983)
234. Y. Gernitzky et al., ATLAS note ATL-MUON-2003-005 (2003)
235. The ATLAS Collaboration (G. Aad et al.), New Small Wheel TDR, https://cds.cern.ch/record/1552862/files/ATLAS-TDR-020.pdf (2013)
236. C. Beard et al., Nucl. Instrum. Meth. A **286**, 117 (1990)
237. The ATLAS Collaboration (G. Aad et al.), ATLAS new Small Wheel TDR, CERN-LHCC-**2013**-006 (2013)
238. The ATLAS Collaboration (G. Aad et al.), Eur. Phys. J. C **75**, 120 (2015)
239. The ATLAS Collaboration, https://atlas.cern/updates/news/NSW-final-slice
240. The ATLAS Muon Collaboration (D. Pudzha et al.), JINST **15**, C09064 (2020)
241. A. Abusleme et al., Nucl. Instrum. Meth. A **817**, 85 (2016)
242. D. Glaser, Phys. Rev. **87**, 665 (1952)

243. P. Queru, Conf. Proc. C **700610V1**, 460 (1970)
244. F.J. Hasert et al., Phys. Lett. B **46**, 138 (1973)
245. H.P. Reinhard, Conf. Proc. C **730508**, 87 (1973)
246. G.S. Abrams et al., Phys. Rev. Lett. **13**, 670 (1964)
247. M. Gell-Mann, CTSL-20, TID-**12608** (1961)
248. M. Gell-Mann, Phys. Rev. Lett. **12**, 155 (1964)
249. http://cds.cern.ch/record/2033326
250. http://it-spots.de/2011/10/brookhaven-national-laboratory-flickr-3/
251. G.E. Chikovani et al., Phys. Lett **6**, 254 (1963)
252. M. Conversi, A. Gozzini, Nuovo Ci. **2**, 189 (1955)
253. M.C. Alkofer, Thiemig München (1969)
254. M. Conversi, I. Federici, Nucl. Instrum. Meth. A **151**, 93 (1978)
255. S. Kinoshito, Proc. Roy. Soc. A **83**, 432 (1910)
256. R. Reiganum, Z. Physik **12**, 1076 (1911)
257. K. Kleinknecht, Detectiors for Particle Radiation, Cambridge University Press, 2nd ed. (1998)
258. W.R. Leo, *Techniques for Nuclear and Particle Physics Experiments* (Springer Verlag, Berlin, 1987)
259. R.K. Carnegie et al., Nucl. Instrum. Meth. A **538**, 372 (2005)
260. L. Sohl et al., JINST **15**, C04053 (2020)
261. D.A. Glaser, Handbuch der Physik **45**, 314 (1958)
262. See Chapter 6